62. Kelly, R. 1990. "Bombardment-Induced Compositional Change." Chap. 4 in *Handbook of Plasma Processing Technology*, ed. S.M. Rossnagel, J.J. Cuomo, and W.D. Westwood. Park Ridge, N.J.: Noyes Publications.
63. Winters, H.F., and J.W. Coburn. 1992. "Surface Science Aspects of Etching Reactions." *Surface Science Rep.* 14:161.
64. Bradley, R.M., J.M.E. Harper, and D.A. Smith. 1986. "Theory of Thin Film Orientation by Ion Bombardment during Deposition." *J. Appl. Phys.* 60:4160.
65. Petrov, I., L. Hultman, J.-E. Sundgren, and J.E. Greene. 1992. "Polycrystalline TiN Films Deposited by Reactive Bias Magnetron Sputtering: Effects of Ion Bombardment on Resputtering Rates, Film Composition, and Microstructure." *J. Vac. Sci. Technol.* A10:265.
66. Yapsir, A.S., L. You, T.-M. Lu, and M. Madden. 1989. "Partially Ionized Beam Deposition of Oriented Films." *J. Mater. Res.* 4:343.
67. Ohmi, T., T. Saito, M. Otsuki, T. Shibata, and T. Nitta. 1991. "Formation of Copper Thin Films by a Low Kinetic Energy Particle Process." *J. Electrochem. Soc.* 138:1089.
68. Homma, Y., and S. Tsunekawa. 1985. "Planar Deposition of Aluminum by RF/DC Sputtering with RF Bias." *J. Electrochem. Soc.* 132:1466.
69. Oechsner, H. 1975. "Sputtering—A Review of Some Recent Experimental and Theoretical Aspects." *Appl. Phys.* 8:185.
70. Thornton, J.A. 1977. "High Rate Thick Film Growth." *Annual Rev. Mater. Sci.* 7:239.
71. Thompson, M.W. 1968. "The Energy Spectrum of Ejected Atoms during the High Energy Sputtering of Gold." *Phil. Mag.* 18:377.
72. Zalm, P.C. 1986. "Ion Beam Assisted Etching of Semiconductors." *Vacuum* 36:787.
73. Zalm, P.C. 1988. "Quantitative Sputtering." *Surf. and Interface Anal.* 11:1.
74. Hoffman, D.W. 1990. "Intrinsic Resputtering—Theory and Experiment." *J. Vac. Sci. Technol.* A8:3707.

8.9 Recommended readings

Biersack, J.P. 1987. "Computer Simulations of Sputtering." *Nuclear Instr. and Methods in Physics Research* B27:21.
Carter, G., and D.G. Armour. 1981. "The Interaction of Low Energy Ion Beams with Surfaces." *Thin Solid Films* 80:13.
Davies, J.A. 1992. "Fundamental Concepts of Ion-Solid Interactions: Single Ions, 10^{-12} Seconds." *MRS Bull.* (June).
Hubler, G.K., ed. 1992. "Pulsed Laser Deposition." *MRS Bull.* (Feb., special issue).
Lafferty, J.M., ed. 1980. *Vacuum Arcs: Theory and Application*. New York: John Wiley & Sons.
Sanders, D. 1990. "Vacuum Arc-Based Processing." Chap. 18 in *Handbook of Plasma Processing Technology*, ed. S. M. Rossnagel, J.J. Cuomo, and W.D. Westwood. Park Ridge, N.J.: Noyes Publications.
Ziegler, J.F., J.P. Biersack, and U. Littmark. 1985. *The Stopping and Range of Ions in Solids*. New York: Pergamon.

Chapter

9

Glow-Discharge Plasmas

The powerful concept of using a plasma to couple nonthermal energy from an electric field into a film-deposition process was introduced in the last chapter. There, we defined the plasma state and examined the arc type of plasma for metal vaporization. We also examined in detail the use of the ion stream emanating from plasmas to accomplish sputter vaporization and film modification. In this chapter, we will focus on the structure and behavior of the widely used glow-discharge type of plasma. We will further see that plasma energy appears not only as ion bombardment, but also as neutral fragments of gas molecules. These "free radicals" have high chemical reactivity which promotes compound formation at a T much lower than that required for thermal reaction. Additional but smaller amounts of plasma energy appear as light and heat.

There are many ways to couple electrical energy into a plasma and many geometrical arrangements of plasma volume, sputtering target, gas source, and film substrate. These factors greatly influence the generation of ions and free radicals and their delivery to the process, so it is important to understand their behavior to obtain the desired film properties. In the following sections, we will examine energy coupling, plasma configuration, and the chemistry of free-radical reactions.

For all plasma configurations, the stages of energy transfer through the plasma are the same, namely: (1) acceleration of free electrons in the applied electric field; (2) electron-impact reactions with gas molecules to generate ions, electrons, free radicals, and excited-state molecules; (3) diffusion of these energetic particles out of the plasma toward the containment walls and film surface, where they dissipate

their energy; and (4) acceleration of ions into the wall and film by the "sheath field" next to it. The steady-state concentration of each type of particle within the plasma represents a balance between its generation rate and its loss rate to the walls. We will first examine the generation of energetic particles by electron impact.

9.1 Electron-Impact Reactions

Consider a free electron of charge q_e immersed in a gas and in an electric field **E** (V/m). The resulting Lorentz force, $q_e\mathbf{E}$, on the electron [Eq. (8.15)] accelerates it in accordance with $F = m_e dv/dt$ until it collides with a gas molecule. There are many possible outcomes of this collision depending on the electron's (translational) kinetic energy, E_e (in electron-volts, or eV). All of these outcomes are important to the behavior of the plasma, and we will examine them in order of increasing E_e. In the lowest E_e range of <2 eV or so depending on the molecule, the collisions are elastic; that is, the energy remains translational. At higher E_e, a variety of inelastic collisions take place, in which E_e is partially converted into internal energy of the target molecule. In the highest E_e range of > 15 eV or so, collisions result in ionization (*potential* energy increase), which sustains the plasma by producing positive ions and new free electrons in accordance with Eq. (8.14).

The key feature of the elastic collision is that the fractional energy transfer, γ_m, is very small, because the electron's mass is only $\sim 10^{-5}$ of the molecule's mass. For example, in a head-on collision with Ar, $\gamma_m = 5.4 \times 10^{-5}$ by Eq. (8.20). Thus, if **E** is strong enough, the electrons can continue to gain energy as they drift through the field undergoing many elastic collisions, until some electrons finally gain enough energy to cause the ionization which sustains the plasma. The low γ_m also means that the gas does not get heated very much by the electron flux. In a glow-discharge plasma producing enough free radicals and ions for thin-film processing, the gas T may only reach 200° C or so. This is different from the arc discharge of Sec. 8.3, whose constricted cross section results in such a high electron flux that the gas does become very hot despite the low γ_m. Considerable gas heating can also occur in very intense glow discharges, as we will see in Sec. 9.5.

The ions gain just as much translational kinetic energy as the electrons per unit travel distance along **E** [(see Eq. (6.6)], but they lose much of it in their first collision with a molecule because of a high γ_m. This process also produces some gas heating, but not very much, because, as we will see in the next section, **E** is by far the strongest at the edge of the plasma and is in the direction that accelerates ions into the wall and electrons into the plasma. Thus, the predominant

energy transfer paths from the plasma's charged particles are ion bombardment of the walls and inelastic electron collisions with gas molecules.

These inelastic collisions occur at higher electron kinetic energy, E_e, than the elastic ones, and they result first in excitation of an electron in the target atom or molecule. The excitation is stimulated by the electric-field pulse produced in the molecule as the free electron passes through it. The excited molecule can then spontaneously (that is, without further collision) undergo one of the following processes, in order of increasing E_e: (1) electron relaxation back toward the ground state, (2) dissociation, or (3) ionization. We discuss these processes in turn below.

Relaxation of an electronically excited state is practically instantaneous ($\sim 10^{-8}$ s) in most cases and is accompanied by the **emission of a UV or visible photon** whose wavelength corresponds to the excited electron's energy-level drop per Eq. (6.5). These emission lines give plasmas their glow and also provide for convenient and nonintrusive *qualitative* analysis of the plasma's atomic composition by optical-emission spectroscopy (OES). However, when molecules and free radicals are present along with atoms, the spectra become quite complicated and many lines remain unidentified. Also, quantification of atomic concentration is frustrated by not knowing either the fraction of atoms in the ground state or the electron energy distribution, both of which affect excitation rate. These problem are sometimes but not always eliminated [1–3] by the use of "actinometry" [4], in which an emission line at a nearby energy and from an atom of known concentration is used to calibrate the electron flux at that energy.

We mention in passing that other analytical techniques such as laser-induced fluorescence (LIF) [5] and line-of-sight mass spectrometry [6] provide more quantitative chemical analysis of plasmas and gases, but they are too complex to use for routine film deposition. The two most convenient analytical techniques are optical emission, as discussed above, and mass-spectrometric sampling of the *effluent* gas (Sec. 3.5). A survey of plasma diagnostic techniques is given in Kroesen (1993).

The relaxation of an electronically excited atom by photon emission is sometimes quantum-mechanically impeded, and then the atom can linger in a **"metastable" excited state** for many seconds until it finally radiates a photon or is deactivated in a collision. The three lightest inert gases have the highest-energy metastables [7]: He* at 19.8 eV, Ne* at 16.7, and Ar* at 11.7. Sufficiently energetic metastables can contribute to dissociation and ionization of weaker species by **"Penning" reactions:**

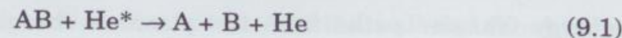

$$AB + He^* \rightarrow A + B + He \quad (9.1)$$

$$C + He^* \rightarrow C^+ + He \quad (9.2)$$

where A and B are atoms or free radicals.

Moving up in electron impact energy, we next come to the **dissociation reactions:**

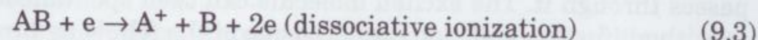

$$AB + e \rightarrow A^+ + B + 2e \text{ (dissociative ionization)} \quad (9.3)$$

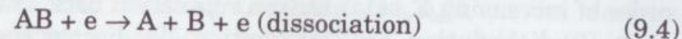

$$AB + e \rightarrow A + B + e \text{ (dissociation)} \quad (9.4)$$

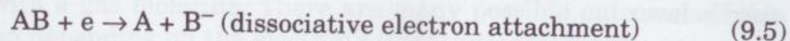

$$AB + e \rightarrow A + B^- \text{ (dissociative electron attachment)} \quad (9.5)$$

The free radicals produced here are very active chemically because of their unsatisfied (dangling) bond, and they are usually the primary reactants in plasma-activated film deposition. Radicals may be molecular fragments or reactive atoms; thus, we have both in

$$SiH_4 \rightarrow SiH_3 + H \quad (9.6)$$

In very intense plasmas where fractional ionization is high, positive ions can become the primary reactants instead of neutral radicals. Negative ions are also formed in plasmas [Eq. (9.5)], but they are not reactive when their formation completes an electron shell[8], as with F^- and SiH_3^-.

The reactive-plasma deposition processes are distinguished from each other according to how each source material is supplied. In activated reactive evaporation (ARE), a solid or liquid (say Al) is thermally evaporated into a plasma of reactive gas (say O_2); thus, $2Al + 3O \rightarrow Al_2O_3$. Reactive sputtering uses the same plasma for sputter-volatilization of the solid source material and for dissociation of the gaseous one. Plasma-enhanced chemical-vapor deposition (PECVD) uses only gaseous source materials, as does thermal CVD (Chap. 7). Plasma dissociation of gaseous reactants can also be employed in any of the beam techniques of Chap. 8. The various plasma configurations appropriate to these processes will be discussed further in subsequent sections.

The key feature of all plasma-activated reactive deposition is that the film-forming reaction(s) can occur at much lower substrate temperature, T_s, than with thermal processes. This is important in the many cases where high T_s causes undesired diffusion across film interfaces, decomposition of film or substrate, or excessive thermal-mismatch stresses upon cool-down. The T_s for deposition is reduced because electron-impact dissociation of relatively cool gas is providing the deposition reaction's activation energy, E_a. That is, free radicals

have highly positive heats of formation because of their dangling bond, so their formation brings the reactants much closer to the top of the activation energy "hill" of Fig. 7.16, or often over it. This was illustrated in Fig. 5.2 for the chemisorption reaction of the gaseous diatomic molecule Y_2 versus its atomic radical Y: for Y_2, there is a positive E_a for chemisorption, but for Y, there is none. The kinetics of free-radical reactions will be discussed further in Sec. 9.6.

The threshold electron kinetic energy to cause dissociation, $E_e°$, lies well *above* the molecular bond strength, E_b, though below the ionization threshold or ion "appearance potential," E_i. The excess of $E_e°$ over bond strength is a consequence of the Franck-Condon principle of quantum mechanics, which observes that electronic transitions occur in a much shorter time than nucleus motion [8]. Thus, electron-impact dissociation becomes a two-step process involving first the excitation of a bonding electron into an antibonding orbital without a change in bond length, as illustrated in Fig. 9.1, followed by separation of the now unbonded radicals and relaxation of their electron energy levels. For example, the SiH_3-H bond strength, E_b, is 376 kJ/mol or 3.9 eV/mc, while the $E_e°$ for SiH_4 dissociation is ≈8 eV (Fig. 9.2). Because of the Fig. 9.1 behavior, $E_e°$ cannot be predicted reliably.

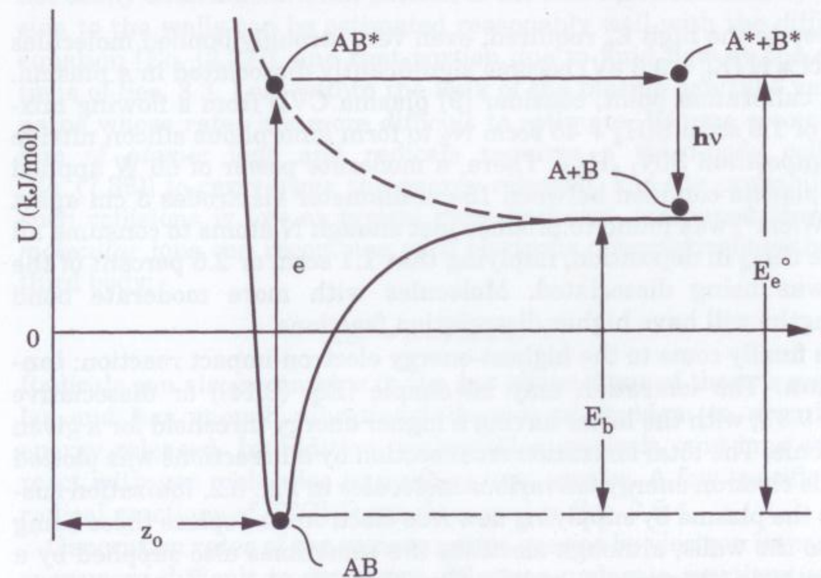

Figure 9.1 Internal energy, U, vs. bond length, z, during electron-impact dissociation of the molecule AB. z_o is the relaxed bond length, the dashed line corresponds to the antibonding orbital, and hν represents photon emission in relaxation of the excited-state radicals A* and B*.

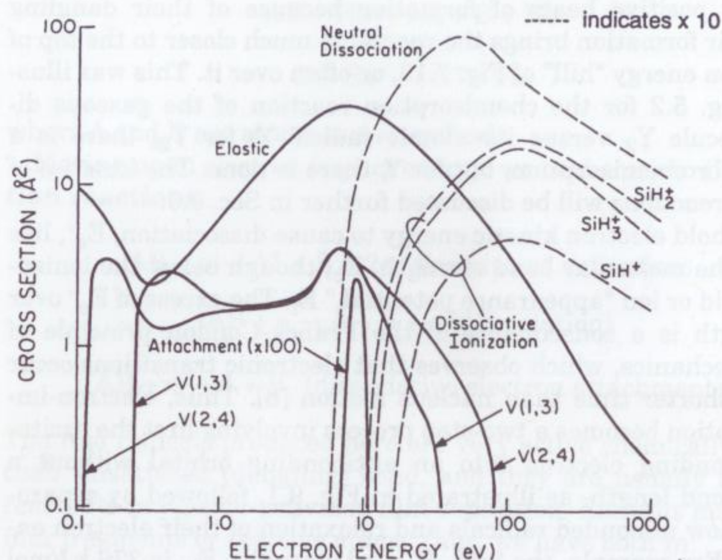

Figure 9.2 Electron-impact reactions of silane gas (SiH_4). Vibrationally excited states are denoted by V(i, j). 1 Å^2 = 10^{-20} m^2. (Source: Reprinted from Ref. 12 by permission.)

Despite the high E_e required, even very strongly bonded molecules like N ≡ N (E_b = 9.8 eV) become significantly dissociated in a plasma. As a calibration point, consider [9] plasma CVD from a flowing mixture of 1.6 sccm SiH_4 + 45 sccm N_2 to form amorphous silicon nitride of composition $SiN_{1.4}H_{0.3}$. There, a moderate power of 60 W applied to a plasma confined between 15-cm-diameter electrodes 3 cm apart (0.3 W/cm^2) was found to produce just enough N atoms to consume all of the SiH_4 in deposition, implying that 1.1 sccm or 2.5 percent of the N_2 was being dissociated. Molecules with more moderate bond strengths will have higher dissociation fractions.

We finally come to the highest-energy electron-impact reaction: **ionization**. The ionization may be simple [Eq. (8.14)] or dissociative [Eq. (9.3)], with the latter having a higher energy threshold for a given molecule. The total ionization cross section by all reactions was plotted versus electron energy for various molecules in Fig. 8.2. Ionization sustains the plasma by supplying new free electrons to replace those being lost to the walls, although electrons are sometimes also supplied by a hot-cathode (thermionic) emitter (Sec. 8.1). The concentration of ions, n_+, and electrons, n_e, in a plasma at steady state—the so-called plasma density—can be quite low and still have a profound effect on film deposition. (Note that n_+ and n_e are about equal except in the thin "sheath" at the plasma boundaries, because a tremendous electrical potential

would develop otherwise.) A typical density for the "parallel-plate" glow discharge (Sec. 9.3) is $n_+ \approx n_e \sim 10^{10}$ cm^{-3}, although special electrodeless coupling techniques (Sec. 9.5) can achieve ~10^{12} cm^{-3}. Thus, in a parallel-plate discharge operating at 100 Pa, where the molecular concentration at room T is 2.4×10^{16} mc/cm^3 [Eq. (2.10)], the fractional ionization is $<10^{-6}$! The level of n_e is not usually monitored during film deposition. The common techniques for doing so are simple in principle but fraught with practical problems (Kroesen, 1993). One technique involves interpreting the current versus voltage (I-V) curve of a small wire "Langmuir" probe immersed in the plasma [10], but perturbation of the plasma by the probe is always a concern, and interpretation of the curve is not straightforward, especially in the presence of negative ions, rf waves, or magnetic fields. In another technique, the plasma's refractive index, which increases with n_e, is measured with a microwave interferometer coupled through windows [11]. This technique is less intrusive, but beam alignment is difficult and spatial resolution is poor.

Ideally, one would like to know the steady-state concentration of *all* of the active species in the plasma, including metastables, radicals, and ions. In principle, this is obtained by setting the generation rate equal to the loss rate for each species, but in practice these rates are not easily determined. That portion of the loss rate occurring by diffusion to the walls can be estimated reasonably well with the diffusion equation [Eq. (2.27)], and that portion due to fluid flow by the equations of Sec. 3.3. Loss within the bulk of the plasma can take various paths whose rates are more difficult to estimate. Volume recombination of *atomic* ions and radicals requires a third-body collision [Eq. (7.38)] to carry away the energy released, and the probability of such collisions is low at typical glow-discharge pressures. However, *molecular* ions can recombine with electrons dissociatively without a third body:

$$AB^+ + e \rightarrow A + B \tag{9.7}$$

Radicals can also recombine in the gas phase if one of them is molecular and has enough vibrational degrees of freedom to absorb the energy released. In addition, metastables, radicals, and ions can all react with gas molecules to produce new species. A few specific free-radical reactions of PECVD are discussed in Sec. 9.6.4.

Generation rates of the various active species by electron impact are even more difficult to determine. Electron-molecule reactions can be described by a second-order rate equation similar to Eq. (7.34) for thermal reactions:

$$R_{Ai}\ (\text{mc/cm}^3\cdot\text{s}) = k_{Ai} n_e n_A \tag{9.8}$$

Here, subscript i indicates the particular reaction of molecule A to which the rate R and rate constant k refer, and the n terms are the concentrations of electrons and of molecule A per cm^3. The behavior of k does not follow the Eq. (7.35) Arrhenius form of thermal reactions, however, because electron energy rather than thermal energy is supplying the reaction activation energy, E_a. Thus, the E_a extracted from an Arrhenius plot versus gas T or substrate T has little meaning in a plasma reaction, even though such E_a values are often reported. The most one can conclude from such a plot is that if E_a is low (say 0.1 eV), the reaction is plasma activated, while if it is much higher, there is likely to be some degree of thermal activation involved.

It is useful to derive an expression for the k of Eq. (9.8) to see what factors do influence it. An electron moving at speed c_e in the plasma undergoes molecular collisions resulting in the reaction of interest (i) at a frequency given by

$$\nu_{ei}\,(s^{-1}) = c_e/l_{ei} = c_e(\sigma_{Ai}n_A) \qquad (9.9)$$

where σ_{Ai} is not the *total* collision cross section with molecules but only the cross section for the (i) reaction, and l_{ei} is the corresponding mean free path. The second equality above was derived earlier as Eq. (2.22). Since c_e and σ_{Ai} are both functions of electron energy, E_e, the reaction rate is not simply given by $R_{Ai} = \nu_{ei}n_e$, but must be obtained by integrating over the electron energy distribution: $f(E_e) = (dn_e/dE_e)/n_e$. That is,

$$R_{Ai} = \int_{n_e} \nu_{ei}\,dn_e = n_e n_A \int_0^\infty \sqrt{\frac{2E_e}{m_e}}\,\sigma_{Ai} f(E_e)\,dE_e \qquad (9.10)$$

where the second equality has been obtained by using Eq. (9.9) for ν_{ei} and Eq. (8.7) for c_e (or v_e) in terms of E_e. Thus, k_{Ai} is given by the second integral.

In only a few cases such as silane (Fig. 9.2) are the $\sigma_{Ai}(E_e)$ functions for the various electron-impact reactions known fairly well, and this is the first hurdle faced in estimating R_{Ai}. In Fig. 9.2, by the way, the one neutral-dissociation curve shown includes all possible neutral fragmentation patterns. The v(1,3) and v(2,4) curves denote vibrational excitation, which is another way for electrons to heat the gas besides elastic collisions. The electron-attachment curve shown is for dissociative reactions of SiH_4 by Eq. (9.5).

The second function needed for Eq. (9.10) is $f(E_e)$. If the electrons gained and lost energy only by colliding elastically with each other—that is, if they were in kinetic equilibrium—$f(E_e)$ would assume the Maxwell-Boltzmann form given in Eq. (2.1) for molecules. However, e-e collisions dominate only when the plasma's ionization fraction is very high. Generally, the E_e gain and loss mechanisms differ, as discussed above, so that $f(E_e)$ is non-Maxwellian. That is, the electrons continue to gain energy in the electric field until they lose their energy upon reaching the threshold for the high-σ inelastic collisions—dissociation and ionization. On balance, this process tends to produce an $f(E_e)$ that is crudely Maxwellian at low E_e and truncated at high E_e, but $f(E_e)$ cannot presently be estimated accurately enough for calculation of R_{Ai} using Eq. (9.10), except for the simplest plasmas such as the inert gases. Considerable research effort is underway to measure σ values and to predict $f(E_e)$ for practical processing plasmas. For reference, we note that a plasma in which e-molecule collisions dominate is called "Lorentzian," and one in which the ionization fraction is high enough so that e-e collisions dominate is "Coulombic."

Despite the above difficulties with $f(E_e)$, the plasma electrons can be described by a characteristic kinetic energy, which can be extracted from Langmuir probe [10] or other measurements. Recall that in a Maxwell-Boltzmann distribution, the mean translational kinetic energy of a particle is related to temperature by $(3/2)k_BT$ [Eq. (2.11)]. On this basis, it is customary in plasma physics to speak of an electron "temperature" even for a non-Maxwellian $f(E_e)$. However, this temperature is given in energy units of eV for convenience, and the (3/2) is dropped; thus,

$$\tilde{T}_e\,(\text{eV}) = k_BT_e/q_e = 8.63\times10^{-5}\,T_e \qquad (9.11)$$

Here, k_B is in J/K, and T_e would be the temperature in K of a Maxwellian distribution. The (~) over T_e signifies eV units and will be used below as a reminder that the electron temperature is in energy units rather than in K. Because only a small fraction of the electrons need to attain the ionization threshold, E_i, in order to sustain the plasma and because E_i does not vary a great deal among gases, $\tilde{T}_e$ is typically a few eV and is not particularly sensitive to plasma process conditions such as power, pressure, and composition. However, in some plasmas to be discussed later where rf fields and magnetic confinement allow the electrons to gain a great deal of energy before being lost to the walls and where the pressure is too low to provide sufficient collisional cooling, $\tilde{T}_e$ can be much higher. The $\tilde{T}_e$ of a few eV is much higher than the mean energy of the ions in a glow discharge, which are cooled by momentum transfer to approach the gas T of a few hundred °C or ~0.1 eV.

As a final topic in electron-impact phenomena, it is useful to estimate the dc electrical conductivity of a plasma. The conductivity of any substance is equal to its concentration of free charges times the drift velocity, v, of those charges per unit of electric field strength (the charge mobility, μ), as was expressed for electrons in Eq. (6.2). Note that the electron drift velocity, v_e, is the velocity of *net* electron motion in the direction of the field and is not the same as the random thermal speed, c_e, of Eq. (9.9). For low ionization fraction (Lorentzian plasma), the mobility of plasma electrons is limited by the drag produced by their collisions with molecules, which are predominantly elastic collisions. Some electrons will leave these collisions retaining part of their forward momentum, and some will have their momentum reversed, so on average the momentum retained will be zero. Thus, the drift momentum of an electron, $m_e v_e$, is reduced to zero at a frequency of just ν_e, the electron elastic-collision frequency with molecules from Eq. (9.9). The drag force so produced must balance the Lorentz force of Eq. (8.15) which is accelerating the electrons; that is,

$$F = d(m_e v_e)/dt = m_e v_e \nu_e = q_e \mathbf{E} \tag{9.12}$$

Solving the last equality for v_e and inserting into Eq. (6.2) using SI units, we have

$$\boxed{s\left(\mathrm{S/m\ or\ }\Omega^{-1}\mathrm{m}^{-1}\right) = \frac{n_e q_e^2}{m_e \nu_e} = \frac{n_e q_e^2}{\sqrt{2E_e m_e}\,\bar{\sigma}_e\, n}} \tag{9.13}$$

Here, ν_e was evaluated for the last equality using Eqs. (9.9) and (8.7); $\bar{\sigma}_e (m^2)$ is a mean value of the elastic cross section; n is the gas concentration (mc/m^3); and E_e is in coulomb-V, not eV. Because the electrons have only 10^{-5} times the mass of the ions and are about the same in concentration, they dominate the conductivity even though their collision frequency is higher than that of the ions due to their higher speed. Equation (9.13) also holds for rf plasmas as long as $\omega_o << \nu_e$ ("collisional" plasma), where ω_o is the rf-drive angular frequency (radians/s).

9.2 Plasma Structure

In the above discussion of the electron-impact reactions which couple electrical energy into the plasma gas, we considered only the bulk plasma region. We now move to the boundary region or "sheath" abutting the walls that confine the plasma. Plasma behavior in this region

is crucial both to sustaining the plasma and to controlling film deposition. Ion and electron loss occurs mostly at the walls, and electrical energy must pass from the walls through the sheath to sustain the plasma. Plasmas affect thin-film processes principally by providing ion bombardment and free radicals to various surfaces, including substrates, depositing films, and sputtering targets. Plasma-surface interaction is determined largely by the *way* in which electrical energy is coupled to the plasma electrons through surfaces, so we will discuss in subsequent sections the various coupling methods and how they affect thin-film processes. First, however, we need to examine the approach of the plasma to the surface and how this results in the plasma sheath.

Recall that a plasma is a partially ionized gas containing about equal concentrations of positive and negative particles. We assume here, as we have previously, that the negative particles are mostly electrons. On the other hand, plasmas rich in extremely electronegative gases such as the halogens can contain more negative ions than electrons, and this increase in mass of the negative particle alters plasma-sheath behavior considerably [13]. However, such plasmas are generally encountered in plasma etching rather than in film deposition. We also continue to assume here that the gas pressure is low enough that the electrons become much hotter than the ions; that is, we are in the glow-discharge regime. Finally, we assume only singly charged ions, which is valid except in very intense plasmas.

Now envision a volume of plasma suspended within a gas. The free electrons and positive ions are held within this volume by their mutual attraction, and there are two quantities which are very useful in characterizing this attraction. The first describes the screening of an ion charge by the electrons which accumulate around it. The electrical potential surrounding a screened ion falls off exponentially with increasing distance away from it. One would expect the distance needed for effective screening to decrease with increasing plasma density, n_e, and also to increase with electron "temperature" (energy), T_e, since the latter will increase the distance to which the electrons can remove themselves from the attraction of the ion's potential field. The distance within which the ion's potential falls to 1/e of the value it would have without screening (the Coulomb potential of Fig. 8.20) is called the **Debye length** and is derived in Chapman (1980; p. 57) as:

$$\lambda_D(\mathrm{cm}) = 0.1\left(\frac{\varepsilon_o \tilde{T}_e}{n_e q_e}\right)^{1/2} = 743\sqrt{\tilde{T}_e/n_e} \tag{9.14}$$

where ε_o = electrical permittivity of vacuum = 8.84×10^{-12} F/m

$\tilde{T}_e$ = electron T in eV [Eq. (9.11)]
n_e = plasma density, e/cm^3
q_e = electron charge = 1.60×10^{-19} C

(The 0.1 appears because of the use of cm rather than the SI unit of m in λ_D and n_e.) A typical plasma having $n_e = 1\times10^{10}$ e/cm^3 and T_e = 3 eV has λ_D = 0.013 cm.

The second quantity used in characterizing charge attraction relates to the plasma's response to a displacement of electrons from ions. If the electric field causing the displacement is removed, the electrons will be pulled back toward the ions, but they will then overshoot and oscillate about the ions at an angular frequency known as the **plasma frequency,** ω_p (s^{-1}), which is also the rate at which the electrons can traverse λ_D:

$$\omega_p = \frac{\bar{v}_e}{\lambda_D} = 10^3\left(\frac{n_e q_e^2}{\varepsilon_o m_e}\right)^{1/2} = 56{,}400\sqrt{n_e} \tag{9.15}$$

For the second equality here, the mean electron velocity in the direction of oscillation, $\bar{v}_e$, was evaluated by setting kinetic energy equal to the thermal energy of one dimension, $(1/2)k_BT_e$. (If SI units were used for n_e, the 10^3 would drop out.) The value of ω_p depends only on plasma density, and for our typical n_e of 1×10^{10} e/cm^3, we have $\omega_p = 5.6\times10^9$ s^{-1} or, dividing by 2π, 897 MHz or 0.9 GHz (gigahertz, pronounced "jiga," referring to "gigantic"). Observe that the second equality has the form of the equation for a mass-spring oscillator, $\sqrt{k/m}$ [Eq. (4.36)]. Here, the spring constant, k, is the Coulomb restoring force of the plasma charge, n_+q_+ (= n_eq_e), acting on an electron charge, q_e. ω_p will be useful later on when we discuss wave propagation of rf electrical energy in plasmas. Because of the restoring force of charge attraction, plasmas are rich in wave phenomena.

We can now proceed with examining our volume of plasma as it approaches the surface. The plasma will diffuse outward toward its containing surfaces, just like any particles diffuse down a concentration gradient. The much higher thermal velocity of the electrons relative to the ions in the bulk of the plasma causes them to lead this diffusion, so that the plasma bulk is left with a net positive charge while the edge collects a negative charge of electrons. These leading electrons are retarded by the positive-ion charge, while at the same time the ions are accelerated out of the plasma by the leading negative charge, so that in steady state, the diffusion velocities of both charges become equal, and the diffusion is said to be "ambipolar." The **ambipolar diffusion velocity,** u_a, can be obtained by setting the electron-plus-ion thermal energy in one dimension equal to the kinetic energy of the diffusing plasma:

$$\frac{1}{2}k_B(T_e+T_+) = \frac{1}{2}(m_e+m_+)u_a^2 \approx \frac{1}{2}m_+u_a^2 \tag{9.16}$$

Here, the electron and ion temperatures are in K. Solving for u_a and adding a second term to account for the drag of ion-molecule collisions due to their mean free path, l_+, in collisions with molecules [14], we have

$$u_a\,(\text{m/s}) = \left[\frac{q_e(\tilde{T}_e+\tilde{T}_+)}{m_+\,(\text{kg})}\right]^{1/2}\left[1+\frac{\pi\lambda_D}{2l_+}\right]^{-1/2} \rightarrow \left[\frac{q_e\tilde{T}_e}{m_+}\right]^{1/2} \tag{9.17}$$

where we have converted to $\tilde{T}$ in eV, and where the last expression holds in the low-pressure ($l_+ \gg \lambda_D$) and high-$\tilde{T}_e$ ($\tilde{T}_e \gg \tilde{T}_+$) regime that usually characterizes film-deposition plasmas. A close analogy exists here to the effusion of gas from an orifice. There, the gas reaches a maximum velocity equal to the speed of sound, which has the same m and T dependence as does u_a (see Appendix E). Thus, u_a is known as the "ion sound velocity." Both phenomena involve the conversion of thermal energy into directed energy. For a plasma of Ar (m_+ = 40 u × 1.67×10^{-27} kg/u) with $\tilde{T}_e$ = 3 eV, u_a by the last expression of Eq. (9.17) is 2.9×10^5 cm/s.

When the ambipolar diffusion front arrives at the surface, the electron charge that leads it is replaced by a negative surface potential that serves the same purpose; namely, to accelerate the ions and retard the electrons so that, in steady state, the escaping fluxes of ions and electrons are equal. The retardation of electrons produces a sheath of positive space charge against the surface, as shown in Fig. 9.3. In this figure, the surface is shown at ground potential, and the **plasma potential,** V_p, is positive with respect to it by $\Delta V_p = V_p - 0$. The level of ΔV_p needed to repel sufficient electrons increases with $\tilde{T}_e$ and also depends on the electron energy distribution, $f(E_e)$, of Eq. (9.10). This boundary condition leads to a key feature of the glow-discharge plasma, namely that *the plasma bulk is always more positive than the most positive of the containing surfaces* (excluding very small surfaces, such as a fine-wire Langmuir probe). As soon as a substantial surface is introduced which has a more positive potential, say V_s, plasma electrons flow into it until the plasma charges up to ΔV_p above it; that is, until $V_p = V_s + \Delta V_p$. This fact will be important in understanding the behavior of plasmas under ac and rf excitation.

The above considerations also apply to electrically floating surfaces, such as substrates suspended in the plasma for deposition. Since these

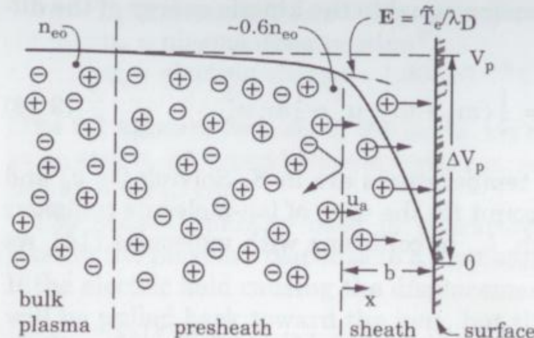

Figure 9.3 Charge distribution and voltage profile near a surface abutting a glow-discharge plasma. ΔV_p is the *minimum* (anode) sheath voltage drop.

surfaces must receive a balanced charge flow in steady state, they develop a **"floating" potential,** V_f (measured from ground), which is negative with respect to the plasma to retard electrons. This means that they also become surrounded by a sheath of positive space charge. For a Maxwellian $f(E_e)$, it can be shown (Chapman, 1980; p. 70) that the voltage drop across this sheath is

$$V_f - V_p = \Delta V_f = -\tilde{T}_e \ln(m_+/2.3m_e) = -\tilde{T}_e (6.7 + \ln M_+) \qquad (9.18)$$

where M_+ is the ion molecular weight. For Ar(M_+ = 40), for example, $\Delta V_f = -10\tilde{T}_e$. Although $f(E_e)$ is generally non-Maxwellian, ΔV_f is still of this order. V_f is easily measured as the potential at which no current flows into or out of a conducting surface or wire (a Langmuir probe [10]) immersed in the plasma.

The presence of ΔV_f and ΔV_p means that *all* surfaces exposed to a plasma have ions accelerated into them through at least this high a potential; that is, at least 10 eV or so. The acceleration potential can be made much higher by negatively biasing the surface, as we will see in the next section, but it cannot be made lower. Fortunately, 10 eV lies in the desirable ion-bombardment-energy window in which surface processes are activated but subsurface damage is avoided, as was discussed in Sec. 8.5. To estimate and control ion-bombardment energy and flux, we need to examine more closely the structure of the sheath and its interface with the bulk plasma.

The interface between the sheath and the plasma occurs roughly where the charge neutrality of the bulk plasma breaks down. According to the conventional "Bohm criterion," this is where the ion velocity begins to exceed the u_a of Eq. (9.17). A more recent definition [15],

which provides a smoother mathematical transition across the interface, places it where the electric field reaches a level of

$$\mathbf{E} = \tilde{T}_e/\lambda_D \qquad (9.19)$$

The region of ion acceleration between the bulk plasma and the sheath edge is known as the **presheath** and is shown in Fig. 9.3. Acceleration in the presheath causes a drop in plasma density to a fraction of the bulk value, n_{eo}, which is 0.6 if one makes the approximations of a Maxwellian $f(E_e)$ and thermal equilibrium (Chapman, 1980; p. 69). Using this 0.6 factor and the Bohm criterion, the ion current density or **ion flux** injected into the sheath is given by the conventional expression for flux as a product of particle concentration and velocity [as in Eqs. (2.5), (4.35), and (6.2)]:

$$j_+ \text{ (A/cm}^2) \approx 0.6 n_{eo} q_e u_a \qquad (9.20)$$

with n_{eo} and u_a in cm units. For our earlier example [after Eqs. (9.14) and (9.17)] of a 10^{10} e/cm^3 Ar plasma at $\tilde{T}_e$ = 3 eV, we have j_+ = 0.28 mA/cm^2. Measurement of n_{eo} requires special techniques (Sec. 9.1 under **ionization**), but we will see later that j_+ can be roughly estimated just from plasma power density for both dc (Sec. 9.3.1) and rf (Sec. 9.4.3) plasmas.

We next need to know the **sheath width,** shown as b in Fig. 9.3. This width is determined by the necessity to maintain a positive field, $\mathbf{E} = -dV/dx$, to draw ions to the surface despite the intervening positive space charge, which reduces $\mathbf{E}$ at the sheath-presheath boundary. In the low-pressure limit where the ions undergo free fall across the sheath without encountering collisions with molecules, this situation is governed by the Child-Langmuir law of space-charge-limited current flow, which was derived as Eq. (8.11) for thermionic electron emission from hot surfaces. Substituting m_+ for m_e in that equation, we have

$$\boxed{j_+ = \frac{4\varepsilon_o}{9}\sqrt{\frac{2q_e}{m_+}}\frac{V_b^{3/2}}{b^2} = 5.5\times10^{-8}\left(\frac{V_b^{3/2}}{M_+^{1/2}b^2}\right)} \qquad (9.21)$$

where M_+ is in atomic mass units, and where the units of b determine the units of j_+. The sheath voltage drop, V_b, will be equal to ΔV_p of Fig. 9.3, or it will be larger if a negative bias is applied to the surface. Solving for the sheath width, b, and setting the current injected from the

plasma [Eq. (9.20)] equal to the current extracted by the sheath field [Eq. (9.21)], we have

$$b^2 = 1.05\times10^{-2}\frac{\varepsilon_o V^{3/2}}{n_{eo} q_e \tilde{T}_e^{1/2}} \tag{9.22}$$

for units of cm and e/cm^3. Observe that b has the same n_{eo} dependence, as does λ_D [Eq. (9.14)], but a different $\tilde{T}_e$ dependence. For this collisionless or **Child-Langmuir sheath,** the ions bombard the surface at their maximum energy, which is the sum of their kinetic energy upon entering the sheath [(1/2) $\tilde{T}_e$ from Eq. (9.17)] and the potential-energy drop across the sheath (q_+V_b). In rf sheaths, however, bombardment energy is less, as we will see in Sec. 9.4.2.

At higher pressures, or for higher V_b where b is larger, various types of collisions occur within the sheath, which both reduce the ion-bombardment energy and increase the space charge. In the **charge-exchange collision,** an electron from a gas atom or molecule jumps over to an ion passing nearby, leaving the atom ionized and the ion neutralized. The latter continues on its course toward the surface without further acceleration, and the former accelerates in the sheath field. When the ion and molecule have the same nuclei, the collision cross section, σ_m, is very large; for example, it is about 4×10^{-15} cm^2 for $Ar^+ \rightarrow Ar$ in the 10-eV range. Ions can also be deflected by molecules without charge exchange occurring, as they are in solids (Fig. 8.21), but the effective σ_m values are much lower for these collisions. Ionization can also occur in the high-pressure sheath by the impact of secondary electrons which are emitted from the surface because of ion bombardment [Eq. (8.13)] and are accelerated toward the plasma by the sheath field.

The effects of charge exchange and electron-impact ionization on b have been calculated [16] for Ar plasma and are shown in Fig. 9.4 for various values of V_b and of injected j_+. Also shown is the mean free path of Ar^+ in room-T Ar based on its charge-exchange σ_m quoted above and using Eq. (2.22) [which applies here instead of Eq. (2.24) because the Ar^+ is traveling much faster than the Ar]. We see that b begins to decrease when pressure, p, increases to the point where the mean free path is less than b; finally, $b \propto 1/p$ in the "ionization limit" where electron-impact ionization dominates the space charge. The increase in space-charge density with p causes b to decrease because it increases the electric-field gradient in accordance with Eq. (8.4). A more recent sheath model [15] uses the presheath-interface criterion of Eq. (9.19) and accounts only for charge exchange, which was found

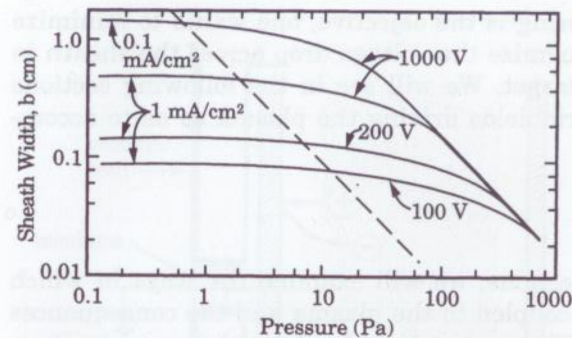

Figure 9.4 Calculated effect of pressure, sheath voltage, and injected-current density, j_+, on the sheath width in an Ar dc plasma. The dashed line is the mean free path of Ar^+ between charge-exchange collisions. (Source: Adapted from a figure in Ref. 16.)

to have a relatively small effect on b. The graphical results reported can be approximated by

$$b^2 \approx 10^{-2}\frac{\varepsilon_o V_b^{4/3}}{n_e q_e T_e^{1/3}} \tag{9.23}$$

where n_e (e/cm^3) is the value at the presheath interface, and b is in cm. Observe that this equation is similar to Eq. (9.22) with some differences in the exponents. It is not easy to determine b experimentally, because it is perturbed by probing and is often smaller than 1 mm. One possible method is observing the position at which gas-phase macroparticles accumulate (see Sec. 9.6.2).

It is important to know the extent to which the sheath is collisional in order to estimate ion-bombardment conditions at the surface. Collisions reduce the energy of the bombardment and also increase its flux by adding to it fast charge-exchanged neutrals and new ions made by electron impact. Both modeling and measurement of these energy and flux distributions are difficult and are not usually available for film-deposition processes, but it is useful to be aware of the qualitative effects of plasma parameters on ion bombardment when designing and operating such processes. Figure 9.4 and Eq. (9.21) together can be used as a guide to determine whether the maximum ion bombardment energy will be reduced by sheath collisions. When subsurface film damage is a concern, it is best to keep the sheath voltage drop at its minimum at the film surface by avoiding negative bias, rather than depending on sheath collisions to reduce ion energy. On the

other hand, when sputtering is the objective, one wants to minimize sheath collisions and maximize the voltage drop across the sheath in front of the sputtering target. We will see in the following sections how to control the electric fields driving the plasma so as to accomplish these objectives.

9.3 DC Excitation

In the following three sections, we will examine the ways in which electrical energy can be coupled to the plasma and the consequences for thin-film processing. These ways include: (1) applying a dc voltage across electrodes within the plasma vacuum chamber; (2) applying ac or rf voltage across these electrodes; and (3) coupling electromagnetic energy through an insulating chamber wall (electrodeless excitation). DC excitation is the oldest and also the simplest of these in concept, so we will address it first. However, its use is limited to electrically conducting materials on the electrodes. RF excitation avoids this restriction because of capacitive coupling, and it also reduces the drive voltage required. Coupling of electromagnetic energy through the vacuum wall is receiving increased attention because of its avoidance of electrodes within the chamber and because of its ability to achieve extremely high plasma density without developing excessive voltages within the chamber.

Recall from previous discussion that plasmas can enhance a film-deposition process in two ways: ion bombardment and free-radical reactions. Ion bombardment can be used for sputter-volatilization of source material or for structural modification of the depositing film, as was discussed in Sec. 8.5. Free radicals made by electron-impact dissociation of gas molecules are useful for their enhanced reaction rates with sputtered source material (reactive sputtering), evaporated source material (activated reactive evaporation—ARE), or each other (plasma-enhanced chemical vapor deposition—PECVD), as was discussed in Sec. 9.1. In this chapter, these various ion-bombardment and free-radical processes will be analyzed in the context of each particular electrical coupling technique rather than process by process.

9.3.1 Parallel-plate configuration

This most widely used plasma configuration and the potential distribution between its two electrode plates are shown in Fig. 9.5. It is often called a "planar diode" by analogy to the vacuum-tube diode, although its electrical behavior is actually rather different. In the figure, the anode is at ground and the cathode is driven negative by the power supply. The bulk of the plasma floats above ground by the plasma

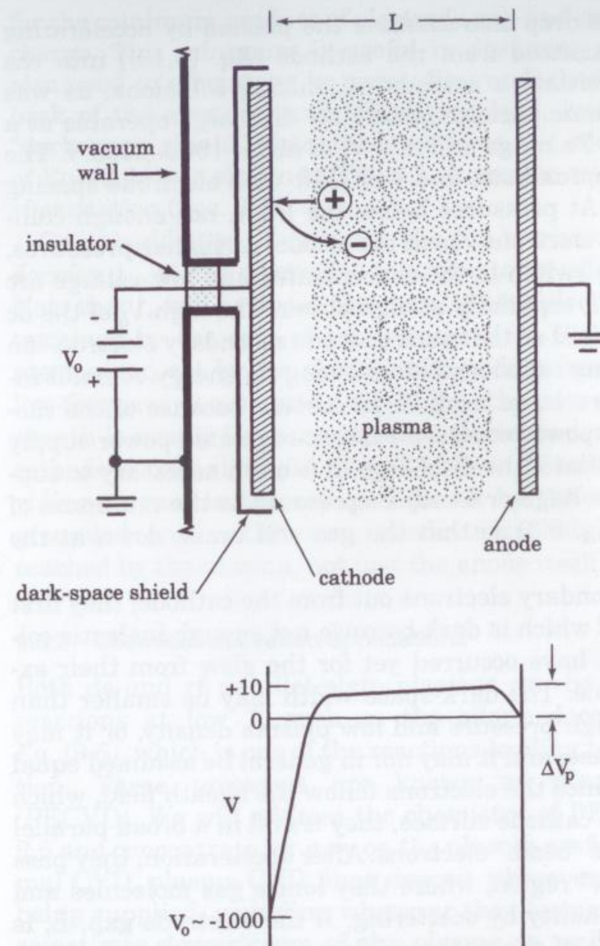

Figure 9.5 Geometry and typical voltage profile of the parallel-plate dc glow discharge. For good coating uniformity in sputtering or PECVD onto stationary substrates, the ratio of electrode diameter to L would be much larger than shown.

potential, ΔV_p, and has little voltage drop across it because of its high conductivity relative to that of the sheaths (see Exercise 9.2). This means that essentially all of the applied voltage, V_o, appears across the cathode sheath. This voltage drop results in high-energy ion bombardment and sputtering of the cathode. The polarity could be reversed, with the cathode at ground and the anode (and the plasma!) driven positive. However, then the grounded chamber walls would also act as part of the cathode, and their sputtering would contaminate the process.

The cathode voltage drop also *sustains* the plasma by accelerating secondary electrons emitted from the cathode [Eq. (8.13)] into the plasma where they initiate a cascade of ionizing collisions, as was shown in Fig. 8.2. The *dc* parallel-plate glow discharge operates at a pressure in the 3–300 Pa range and at a V_0 of about 1000–2000 V. The pressure limits are approximate and will shift with electrode spacing and gas composition. At pressures below the limit, not enough collisions occur before the electrons reach the anode. At higher pressures, the discharge tends to switch to the concentrated and low-voltage arc mode shown in Fig. 8.7, especially at high power. The high V_0 of the dc glow discharge is required so that each cathode secondary electron can produce enough ionizing collisions before losing its energy. A small increase in V_0 results in a large increase in current because of the cascade effect, so for good power control a current-regulated power supply is used. To "strike" (initiate) the discharge, it is often necessary to supply a spike of higher voltage or to adjust pressure to the minimum of the Paschen curve (Fig. 8.3) so that the gas will break down at the voltage available.

As we follow the secondary electrons out from the cathode, they first cross the "dark space," which is dark because not enough inelastic collisions with molecules have occurred yet for the glow from their excited states to be visible. The dark-space width may be smaller than the sheath width at high pressure and low plasma density, or it may be larger in opposite case, and it may *not* in general be assumed equal to the sheath width. Since the electrons follow the sheath field, which is perpendicular to the cathode surface, they travel in a broad parallel beam and are known as "beam" electrons. After acceleration, they pass into the "negative-glow" region, where they ionize gas molecules and also lose their directionality by scattering. If the electrode gap, L, is smaller than the width of the negative glow, the beam electrons are likely to reach the anode before undergoing an ionizing collision. Such a discharge is said to be "obstructed," and any further decrease in L causes a sharp rise in V_0 and ultimately extinction of the plasma. The region of plasma beyond the negative glow is known as the "positive column."

The width of the negative glow is roughly the mean free path for ionizing collisions as given by Eq. (2.22). Using the ideal-gas law [Eq. (2.10)] and room T to obtain the molecular concentration, n, in Eq. (2.22), and taking the ionization cross section for small molecules at 1 keV from Fig. 8.2 ($\sigma_m \approx 1\times10^{-16}$ cm^2), we have

$$\boxed{Lp \sim 40 \text{ Pa}\cdot\text{cm}} \qquad (9.24)$$

for the minimum product of electrode gap and gas pressure in a dc discharge. This minimum is useful in designing plasma reactors. It is also used to advantage in preventing undesired discharges along the back of the electrode and its voltage lead, by installing a grounded "dark-space shield" along these surfaces at a spacing well under the L of Eq. (9.24), as shown in Fig. 9.5. A similar minimum L applies with rf excitation (Sec. 9.4).

One would like to estimate the ion-bombardment flux or current density, j_+, at the electrodes to estimate its effect on film processing. Note that j_+ will be about the same at both electrodes, because it is determined by the rate of ion injection into the sheath from the bulk plasma and not by the sheath voltage drop [see Eq. (9.20)]. In dc and low-frequency-ac plasma (< 1 MHz), the current passing across the sheath is mostly ion current, since the secondary-electron yield at the cathode is only about 0.2 [Eq. (8.13)], so j_+ is roughly estimated by dividing current in the external circuit by the electrode area. For the grounded anode, this area needs to include all grounded surface reached by the plasma, not just the anode itself.

9.3.2 Chemical-activation applications

Both dc and rf parallel-plate plasmas can be used to activate CVD reactions at low T, such as the silane decomposition reaction of Eq. (9.6), which is one of the reactions leading to amorphous Si deposition. These processes are known as **plasma-enhanced CVD** (PECVD). We will address the chemistry of PECVD reactions in Sec. 9.6 and concentrate for now on the plasma configuration. As with thermal CVD, plasma-CVD films deposit wherever the reaction energy is being supplied, including wherever the plasma touches a surface and sometimes downstream of the plasma as well. Usually, substrate-T control is important to film quality, and therefore the substrate is generally placed on one of the electrodes rather than being suspended in the plasma. This maximizes heat transfer by gas conduction (Sec. 5.8.2) between the substrate and the electrode, whose T can be controlled. The choice of anode or cathode for the substrate position depends on the desired energy of film ion bombardment. In amorphous Si films, for example, termination of dangling Si bonds by H is needed to remove electron trap states from the band gap, and excessive bombardment dislodges the H. There, "anode material" is a better semiconductor than "cathode material." On the other hand, when the tensile stress of a film is excessive, high bombardment energy can counteract it by the ion-peening effect (Sec. 8.5.3). For good plasma uniformity across the substrate, both electrodes should be larger in radius than the substrate by several times the electrode gap to avoid

the plasma-density dropoff region at the edges, which results from ambipolar diffusion (Sec. 9.2).

When a large substrate needs to be coated, the reactant gases are distributed evenly over it through a "showerhead" array of holes in a hollow counterelectrode into which the gases are metered. The holes should have a diameter much less than the sheath width so that they do not create "hot spots" in the plasma. This problem results from the hollow-cathode effect illustrated in Fig. 9.6. Penetration of the sheath edge into the hole creates a region of plasma that is more intense than elsewhere, because beam electrons are being injected into it from all around rather than just from a plane. This localized region of enhanced conductivity preferentially attracts the applied power, which further enhances the local current of ion bombardment and beam electrons. This is an unstable, "runaway" situation which results in arc plasmas (Sec. 8.3) developing at some or all of the holes and much less power being dissipated where one usually wants it—in the uniform glow discharge. Moreover, the arcs quickly erode away the edges of the holes. The same situation develops in rf plasmas. Because sheath width decreases with increasing plasma density [Eq. (9.22)], arc breakdown sets an upper limit to plasma density and power in glow discharges and is one of the reasons why electrodeless discharges (Sec.

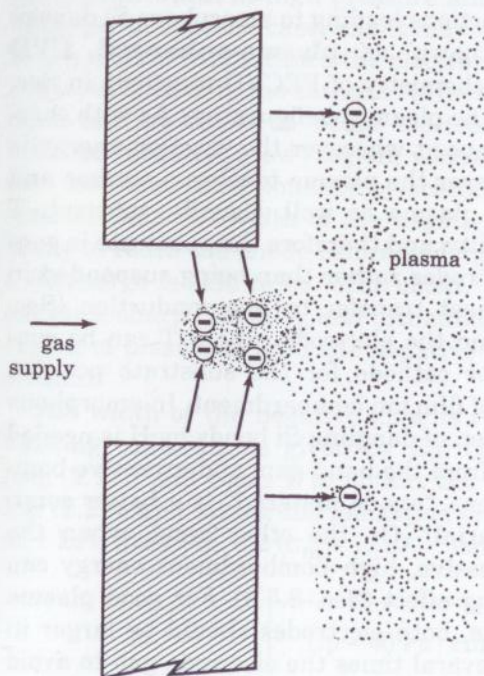

Figure 9.6 Hollow-cathode intensification effect at a hole in the plasma cathode.

9.5) are attractive. Of course, one could specifically design a showerhead to operate in the hollow-cathode mode as a way to achieve high localized plasma density. Even in the absence of holes in the electrodes, high enough plasma density leads to arc breakdown at cathode surface asperities due to field emission [Eq. (8.12)].

A glow discharge can also be used to activate a gaseous reactant in the presence of a thermally evaporated reactant in the process known as **activated reactive evaporation** (ARE) [17]. The evaporant is usually a metal, and the gas can be, for example, O_2, NH_3, or CH_4, for the formation of metal oxide, nitride, or carbide films, respectively. In ARE, a thermionic (hot) cathode (Fig. 8.1) is preferred to a simple plate cathode, for the following reason. The parallel-plate glow discharge is a "cold-cathode" discharge in which the sustaining electrons are generated mostly by gas ionization. This places a lower limit on gas pressure, p [Eq. (9.24)], and this limit can cause various problems. In subsequent discussion, we will see how excessive p scatters ions and vaporized source material, depletes the kinetic energy of sputtered species, and causes macroparticle formation. There are several ways in which a glow discharge can be made to operate at lower p, including electrodeless excitation (Sec. 9.5), the magnetron (Sec. 9.3.4), and the thermionic cathode which we presently consider.

One geometry for ARE is shown in Fig. 9.7. Electrons thermionically emitted from the hot-filament cathode are accelerated toward the pos-

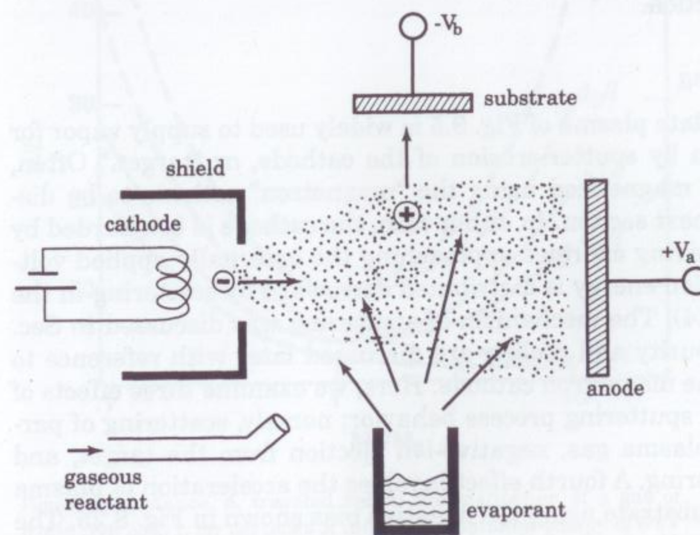

Figure 9.7 Typical geometry for compound-film deposition by plasma-activated reactive thermal evaporation.

itively biased anode plate. Even without a plasma, this current dissociates and ionizes intervening gas by electron impact, as it does in the ion gauge (Fig. 3.6*c*). With increasing p, additional current flows because of the resulting plasma. However, because of the thermionic emission, there is no lower p limit. Thus, p can be low enough that evaporant can be transported across the plasma to the substrate without being excessively scattered by intervening gas. Some of this evaporant will also become ionized as it crosses the electron beam (see Exercise 9.6). The ions of gas and vapor can be accelerated into the film if so desired by applying a negative potential to the substrate. Finally, the film-forming reaction takes place on the surface between adsorbing vapor and gas radicals. The filament may need to be shielded from the vapor to prevent alloying, and in oxidizing gases it needs to be made of Ir rather than W. Filament design is discussed in Appendix D. ARE can also be done with an electron-beam evaporation source (Fig. 8.4). There, the plasma which is always generated over the source in the presence of a gas background can be enhanced by adding an anode collector plate or ring above the source. Electrodeless sources of gas radicals and ions can also be used for ARE, and these will be discussed in Sec. 9.5.

The third mode of plasma chemical activation uses a sputtered source material along with a gaseous one. The gas becomes dissociated in the sputtering plasma and reacts to form a compound film, such as $Ti + N_2 \rightarrow TiN$. This **reactive sputtering** technique will be discussed in the next section.

9.3.3 Sputtering

The parallel-plate plasma of Fig. 9.5 is widely used to supply vapor for film deposition by sputter-erosion of the cathode, or "target." Often, the plasma is magnetized using the "magnetron" cathode to be discussed in the next section. In either case, the cathode is bombarded by plasma ions having energies approaching the externally applied voltage, although ion energy is distributed downward by scattering in the sheath (Fig. 9.4). The mechanism of sputtering was discussed in Sec. 8.5.4. Target purity and cooling are discussed later with reference to Fig. 9.10 for the magnetron cathode. Here, we examine three effects of the *plasma* on sputtering process behavior; namely, scattering of particles by the plasma gas, negative-ion ejection from the target, and reactive sputtering. A fourth effect involves the acceleration of plasma ions into the substrate using the negative bias shown in Fig. 8.25. The resulting "resputtering" of the depositing film can produce effective planarization of rough topography (Fig. 8.31), and the bombardment can modify film structure in various ways (Sec. 8.5.3).

Even at the lowest operable pressure of the dc-diode plasma [Eq. (9.24)], there is considerable **gas scattering** of sputtered particles as they cross the plasma, with consequent loss of their desirable kinetic energy and loss of deposition rate by backscattering. Magnetic confinement is widely used to reduce minimum pressure and thus avoid these problems, but for now we examine the simple planar diode. By Eq. (9.24), minimum diode pressure is about 10 Pa for a typical electrode gap of L = 4 cm. At this pressure, the mean free path between atomic collisions, l, is ~0.1 cm per Eq. (2.24), so a sputtered particle will undergo many collisions in crossing the gap. The number of collisions needed to "thermalize" *any* energetic particle to the mean kinetic energy of the surrounding gas atoms depends on the efficiency of energy transfer as expressed in Eq. (8.20) and is therefore a minimum for equal masses of particle and gas atom. Ultimately, one wants to know the distance, d, traveled toward the substrate before **thermalization,** and this is shown in Fig. 9.8 in terms of number of mean free paths (d/l) versus the ratio of gas to energetic-particle mass (M_g/M_s) and for initial translational energies corresponding to that of a typical

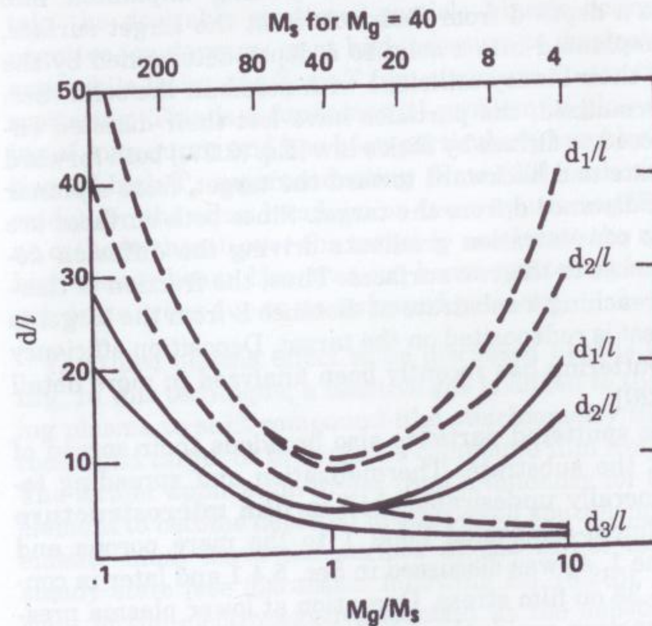

Figure 9.8 Distance, d, traveled before thermalization of a gas of mean free path l, for particles of initial translational energy of 5 eV (solid line) or 1000 eV (dashed line) using three calculational models (d_1, d_2, d_3) vs. the mass ratio of the gas atom (M_g) to the energetic particle (M_s). (Source: Reprinted from Ref. 18 by permission.)

sputtered particle (5 eV) and that of a reflected plasma ion or ejected negative ion (1000 eV) coming from the target. These calculations also take into account the increase in mean free path with decreasing mass and with increasing energy [18]. The thermalization distance is minimum for $M_g = M_s$, as expected. For our example above, the substrate was 40 mean free paths from the target, so even for large mass differences, sputtered particles will be thermalized before reaching the substrate. On the other hand, the more energetic reflected (positive) or ejected (negative) ions can arrive still retaining some energy. Figure 9.8 can be used to estimate the conditions needed either to preserve the desirable kinetic energy of the sputtered particles or to thermalize the much higher and usually undesirable kinetic energy of the reflected or ejected ions. At high sputtering power, however, local rarefaction of the gas in front of the target due to "sweep-out" by the sputtered particle flux increases the l in the electrode gap above that calculated from gauge pressure [19].

The fractional **deposition-rate loss** due to a thermalization distance, d, which is less than the electrode gap, L, can be estimated as follows. The sputtered particles are essentially being "implanted" into the plasma gas to a depth d from their source at the target surface, just as ions are implanted into a solid to a depth determined by the stopping power of their binary collisions with atoms in the solid (Sec. 8.5.2.2). Once thermalized, the particles have lost their directed energy and then proceed to diffuse by Fick's law [Eq. (2.27)] both forward toward the substrate and backward toward the target, from a planar source situated at distance d from the target. Since both surfaces are particle sinks, the concentration gradients driving the diffusion depend only on distances to the two surfaces. Thus, the fraction of thermalized particles reaching a substrate at distance L from the target is just d/L, and the rest is redeposited on the target. Deposition efficiency in planar-diode sputtering has recently been analyzed in more detail along these lines [20].

Scattering of the sputtered particles also broadens their spread of incident angles at the substrate. Thermalization and spreading together cause a generally undesirable shift in **film microstructure** from the bombardment-compacted Zone T to the more porous and weakly bonded Zone 1, as was discussed in Sec. 5.4.1 and later in connection with Fig. 5.38 on film stress. Operation at lower plasma pressure using the magnetron avoids this problem.

We now turn to the second plasma effect on sputtering behavior: **negative ions** ejected from the target. In a compound target, when one element has a low ionization potential, E_i, (say 6 eV) and the other has a high electron affinity (say 2 eV), so that the difference between

the two becomes small, it is likely that the latter element will be sputtered as a negative ion rather than as a neutral atom. Elements of high electron affinity include the halogens (F, Cl, . . .) and the chalcogens (O, S, . . .) to the right of the periodic table, and some transition metals such as Au. Elements of low E_i include the alkali metals (Li, Na, . . .) and alkaline earths (Be, Mg, . . .) to the left, and the rare earths (La, . . . Sm, . . .). Indeed, the negative-ion yield from a Au target was found [21] to increase by 10^4 when the Au was alloyed with Sm. Negative ions get accelerated into the plasma along with the beam electrons by the cathode sheath field. For pressures above 1 Pa or so, they will be stripped of the extra electron in the plasma [22]; but unless the Lp product [Eq. (9.24)] is very high, they can still cross to the depositing film and bombard it with enough energy to damage it or erode it. This will occur more in the direct beam path than off to the side, especially in magnetron sputtering at low pressure. Negative-ion-beam effects have even been seen [22] in ZnO, despite the relatively large difference between the appearance potential of Zn^+ and the electron affinity of O (9.4–1.46 eV). When negative-ion flux is substantial, one is faced with the dilemma of operating either at low pressure to retain the desirable sputtered-particle kinetic energy while suffering negative-ion damage, or at high pressure to dissipate negative-ion energy while losing the Zone T film structure due to thermalization and scattering. This is a fundamental problem in *glow-discharge* sputtering of compounds and has been particularly troublesome in the deposition of high-T_c superconducting films [23] such as YBCO (Y-Ba-Cu oxide). On the other hand, in *ion-beam* sputtering (Fig. 8.25*a*), there is no cathode sheath over the target to accelerate the negative ions into a high-energy beam. However, ion-beam sputtering is restricted to small substrate areas due to its awkward geometry.

The third plasma effect to be discussed here is **reactive sputtering**. In this technique, a reactive gas is added to the usual Ar sputtering plasma to shift compound-film stoichiometry in sputtering from a compound target or to deposit a compound film from a metallic target. The former application arises from a tendency for the electronegative element to become depleted in compound sputtering. Although both elements must leave the surface at the target composition ratio in steady state [see discussion following Eq. (8.38)], the sticking coefficient of the electronegative element at the substrate is likely to be lower, resulting in a substoichiometric deposit. This shortfall can be compensated by addition of an appropriate amount of that element to the supply flow of sputtering gas. Thus, the transparent conducting film indium-tin oxide (ITO) is sputtered from a compound target in Ar + O_2. The O_2 flow is raised enough to reduce film optical absorption

by metal precipitates but not enough to produce excessively resistive films.

Compound deposition by reactive sputtering from a metal target generally lowers target fabrication cost and increases target purity as compared to using a compound target, but it complicates process control when film composition is critical. The process-control problem is illustrated in Fig. 9.9. This **hysteresis loop** can be plotted using a quartz-crystal deposition-rate monitor (Sec. 4.8.1) or by monitoring an optical-emission line from the metal vapor in the plasma. When the metal target is being sputtered in pure Ar (point A), the sputtering rate is relatively high. As the reactive-gas supply flow is increased, rate remains high until some point, B, at which the gas adsorption rate on the target exceeds the sputtering rate. Then, the target becomes "poisoned" with adsorbed gas, and the sputtering rate drops to a much lower level (C) because much of the ion bombardment now goes into sputtering away the continuously adsorbing gas layer rather than into sputtering the underlying metal. If the reactive-gas flow is now decreased, the poisoned condition persists until point D, where the sputtering rate begins to exceed the adsorption rate so that the target can clean itself and return to a high sputtering rate.

To describe the hysteresis loop of Fig. 9.9 quantitatively and to determine the relationship between mass flow and film composition, it is necessary to think in terms of the partial pressure, p_i, of the reactive gas. Equation (3.8) relating p_i to pumping speed needs to be modified for this situation as follows:

$$p_i = Q_i/(C_o + C_s) \qquad (9.25)$$

Here, Q_i (Pa·l/s) is the mass flow rate of the reactive gas, C_o (l/s) is the pumping speed of the chamber vacuum pump reduced by its connecting piping and throttle valve (Fig. 3.3), and C_s is the pumping speed of the *depositing metal* for the reactive gas, which adsorbs on it

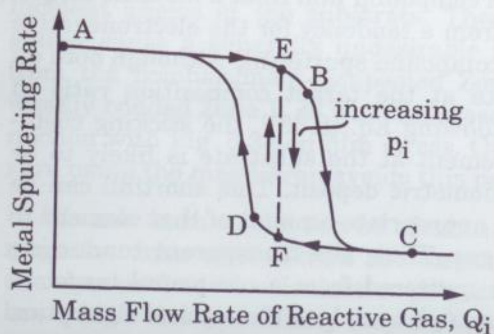

Figure 9.9 Typical process behavior of metal sputtering in reactive gas i, with the mass flow rate of Ar fixed.

and becomes buried ("getter" pumping). If the metal is depositing much faster than the gas, C_s is the same as the conductance of a molecular-flow orifice: 11.6×A *l*/s for the case of room-T air [Eq. (3.5)], where A is the adsorption area in cm^2. That is, all of the gas arriving at A is pumped by burial. For slower metal-deposition rate or higher p_i, C_s will be reduced by the fractional surface coverage of reactive gas, Θ, in accordance with the Langmuir adsorption model discussed prior to Eq. (6.20). Returning now to Fig. 9.9, consider an attempt to operate at point E on the hysteresis loop, where the ratio of metal deposition flux to p_i happens to produce the desired stoichiometry in the compound being deposited. Now if Q_i should drift up by the slightest amount, p_i will increase and cause both Θ and target poisoning to increase. These effects both reduce C_s and cause p_i to increase further per Eq. (9.25). This *positive feedback* produces an inherently unstable situation which results in the process drifting to point F, where for the same Q_i, metal deposition rate is much lower and p_i is much higher, thus reducing process throughput and shifting film composition. From point F, a slight downward drift in Q_i could cause a return to point E, so film composition is not controllable within the hysteresis-loop area.

The width of the loop can be reduced by increasing C_o in Eq. (9.25), because that lessens the effect of a fluctuating C_s. Also, the loop can be shifted to the right by introducing the reactive gas near the substrate to produce a higher p_i there than at the target [24], thus reducing the degree of poisoning for a given Q_i. Operating at high sputtering rate further reduces poisoning by causing gas rarefaction in front of the target [19]. However, it may still be desirable to operate at point E to obtain the desired stoichiometry at high deposition rate. This can be done if sufficient *negative* feedback is imposed to counteract the positive feedback inherent to the process. To do this, one needs to monitor p_i or some related signal and inject it into a feedback control loop to drive Q_i. (The same technique was applied to T control in Sec. 4.5.3.) That is, if p_i starts to drift up from its programmed set point, Q_i needs to be driven down to restabilize it. Convenient signals include the p_i reading on a downstream mass spectrometer, an optical-emission line from the reactive gas in the plasma, or the voltage across the plasma under constant-power control, since plasma impedance changes with gas composition. Extensive mathematical modeling of reactive sputtering has been done [24], including the case of *two* reactive gases for the deposition of compounds such as oxynitrides, where the control problem is much more difficult [25]. In reactive deposition by the narrow-beam evaporation processes of Secs. 8.2–8.4, source poisoning does not occur, because the evaporation flux is always much higher than the adsorption flux of reactive gas.

9.3.4 Magnetrons

The lower limit of operating pressure in the planar-diode sputtering plasma (Fig. 9.5) was imposed by the need for the beam electrons ejected from the cathode to undergo enough ionizing collisions with the gas to sustain the plasma before they reach the anode and are removed there. The magnetron has been a major advance in sputtering technology, and greatly improves upon this situation. Basically, it incorporates a crosswise magnetic field over the cathode, which traps the beam electrons in orbits in that location and thus greatly increases their path length before they finally escape to the anode by collisional scattering. Because the electron's travel path is now much longer than the electrode gap, L in Eq. (9.24), the minimum pressure to sustain the plasma is much lower for the magnetron than for the planar diode—typically 0.1 Pa instead of 3 Pa. At 0.1 Pa, the sputtered particles retain most of their kinetic energy upon reaching the substrate, so one obtains the beneficial effects of this energy on film structure, as discussed in Sec. 8.5.1.3. Also, deposition rate is increased because of reduced scattering and redeposition of sputtered particles on the cathode, although redeposition is still measurable [19]. Finally, the increased efficiency of electron usage means that lower applied voltage (typically 500 V) is needed to sustain a plasma of a given density, n_e, and that the voltage increases even less steeply with power than it does in the planar diode [26]. Unfortunately, the magnetic field cannot be made strong enough to deflect the problematic cathode negative ions that were discussed in the previous section, although their influence is reduced by the lower cathode-sheath voltage of the magnetron. Another problem is that the erosion pattern of a magnetron target is highly nonuniform across the surface, as we will see below. This pattern becomes imprinted on films deposited on stationary substrates when negative ions are affecting the film, because of the beam nature of these ions. Deposition-rate nonuniformity is less sharply imprinted, because the sputtered particles are neutral and are emitted in more or less the broad cosine distribution (Sec. 8.5.4.2). Both magnetrons and planar diodes can also be operated using rf excitation when one needs to couple power through insulating targets.

Many configurations of magnetic field and cathode shape have been developed for various applications [26, 27], but we will discuss magnetron operating principles with reference to the planar, circular configuration of Fig. 9.10. The overall setup for magnetron sputtering was discussed in connection with Fig. 8.25*b*, while here we examine the magnetron cathode in more detail. The target material to be sputtered is a disc 3 to 10 mm thick which is bonded for good thermal contact to a water-cooled Cu backing plate. Bonding is best done by soldering, al-

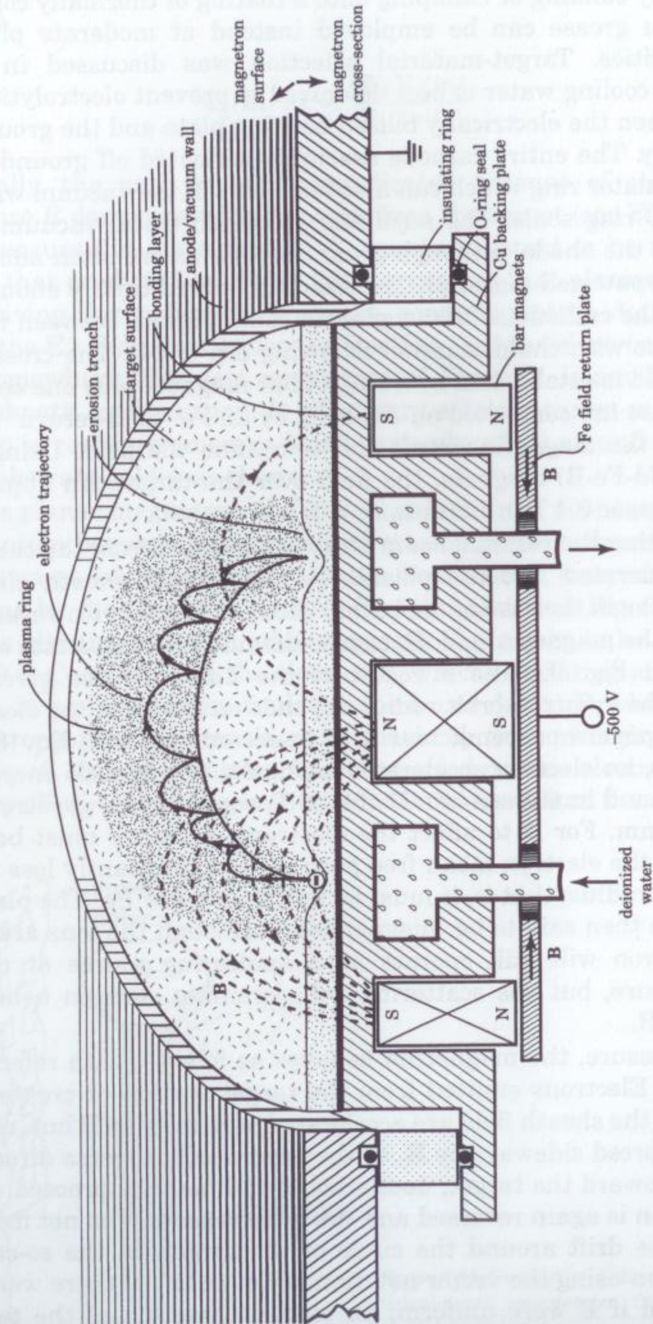

Figure 9.10 Planar-magnetron structure and behavior. The electron-orbit radius is shown much larger than actual size for clarity.

though epoxy bonding or clamping onto a coating of thermally conductive vacuum grease can be employed instead at moderate plasma power densities. Target-material selection was discussed in Sec. 8.5.4.1. The cooling water is best deionized to prevent electrolytic corrosion between the electrically biased backing plate and the grounded water supply. The entire cathode assembly is floated off ground by a ceramic insulator ring which can also form part of the vacuum wall by employing O-ring seals. The adjoining grounded metal vacuum wall then acts as the anode, although grounded shields are often added to confine the sputtered material. The anode is spaced closely enough to the edge of the cathode so that a plasma cannot ignite between them, in accordance with the discussion following Eq. (9.24). The crosswise magnetic field is established by a ring of bar magnets plus one central one, and these are connected on the back by an Fe "field-return" plate to complete the magnetic circuit and to confine the field. Using the strongest (Nd-Fe-B) magnets, the field over the target can approach one kilogauss, or 0.1 T in SI units.

Upon igniting the plasma, beam electrons emitted from the cathode become accelerated into the plasma by the cathode-sheath electric field, **E**, just as in the case of the planar diode of Fig. 9.5. However, the presence of the magnetic field, **B**, causes them to also curve into orbits as shown in Fig. 9.10 as a result of the Lorentz force given by Eq. (8.15). The gyratron-orbit radius depends on **B** and on the electron velocity component perpendicular to **B** in accordance with Eq. (8.17). For example, an electron accelerated vertically to a kinetic energy of 500 eV by **E** and immersed in a **B** of 0.03 T would have a gyratron radius of 2.5 mm. For **B** to affect the electrons, pressure must be low enough that the electron mean free path is not significantly less than the gyratron radius; that is, it must be less than a few Pa. The plasma electrons are then said to be "magnetized," although the ions are not. The magnetron will still operate as a sputtering source at much higher pressure, but gas scattering will dominate electron behavior rather than **B**.

At low pressure, the magnetron behaves as follows, with reference to Fig. 9.10. Electrons emitted from the target surface or created by ionization in the sheath field are accelerated vertically by **E** but, at the same time, forced sideways by **B**, so they eventually reverse direction and return toward the target, decelerating in **E** as they proceed until their direction is again reversed and the cycle repeats. The net motion is a clockwise drift around the circle of the target, in the so-called **E**×**B** direction using the vector notation of Eq. (8.15). If there were *no* collisions and if **E** were uniform, an electron starting at the target with zero kinetic energy would follow a "cycloidal" path, which is the same as that of a point on the periphery of a wheel rolling along the

ground, and the time-average **E**×**B** drift velocity would be (Cecchi, 1990)

$$u_d(\mathrm{m/s}) = \frac{|\mathbf{E}|(\mathrm{V/m})}{|\mathbf{B}|(\mathrm{tesla})} \tag{9.26}$$

Actually, the path is more complicated because of collisions and because **E** decreases with distance from the target (see Fig. 9.3). Also, u_d measured in magnetrons [27] has been found to be much larger than that predicted by Eq. (9.26), suggesting that plasma *waves* may be driving the motion. In any case, good magnetron design requires that the **E**×**B** drift path close on itself so that the electrons do not pile up somewhere. The post magnetron of Fig. 9.11 is another common closed-path configuration. It offers very efficient target-material utilization in coating numerous small parts placed all around the cylindrical substrate holder as shown.

The planar magnetron of Fig. 9.10 suffers from poor target-material utilization because of the trenched erosion pattern shown. The radial narrowness of this trench results from radial compression of the plasma by the magnetic-mirror effect illustrated in Fig. 9.12. This effect is also important in other magnetized plasmas to be discussed in Sec. 9.5. Consider first the electron *a*, which is orbiting at some velocity $\mathbf{v}_e$ in a plane perpendicular to the z axis due to **B**, which is becoming stronger with increasing z as shown by the converging field lines. By Eq. (8.15), the resulting force **F** exerted on this electron will be in the $\mathbf{v}_e \times \mathbf{B}$ direction, perpendicular to **B**. Because **B** at the orbit periph-

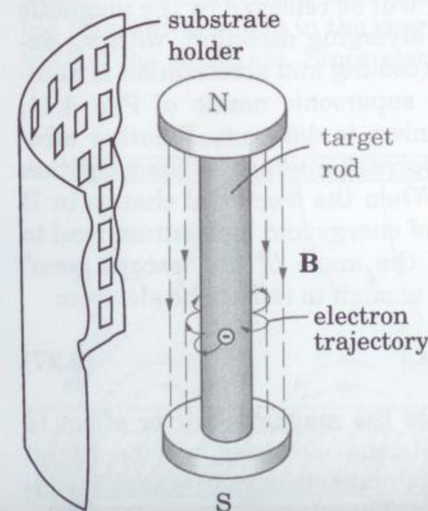

Figure 9.11 Geometry of the cylindrical post magnetron. (Anode rings not shown.)

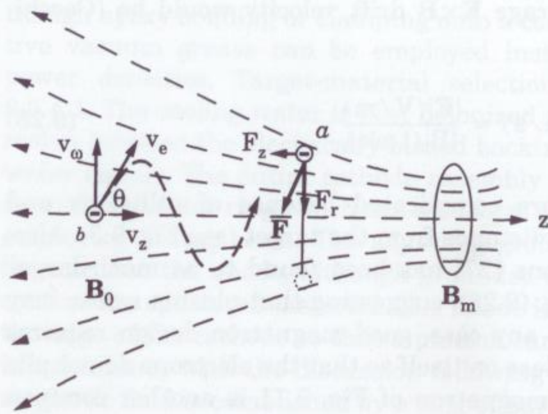

Figure 9.12 Behavior of electrons in a magnetic mirror.

ery is not parallel to z, **F** resolves into an axial component, F_z, as well as a radial one, F_r, and F_z accelerates the electron *away from the converging field*. Note that this would also be true for reversed polarity of field or charge. Since **F** is always perpendicular to $\mathbf{v}_e$, the electron's kinetic energy remains unchanged in this process, and therefore the axial acceleration has to be accompanied by a corresponding reduction in the circumferential (orbit) velocity. Conversely, consider electron *b*, whose velocity $\mathbf{v}_e$ has a z component, v_z, as well as a circumferential one, v_ω. As this electron spirals toward the converging field, the directed velocity, v_z, decreases, and the "thermal" one, v_ω, increases. If v_z passes through zero before the electron reaches the position of maximum field strength, $\mathbf{B}_m$, the electron will be reflected by the magnetic mirror and accelerated back in the diverging direction, with v_ω decreasing (cooling) as it proceeds. This cooling and acceleration is analogous to molecular behavior in the supersonic nozzle of Fig. 4.11, although the energy transfer mechanism is different. Whether electron *b* gets reflected depends on its approach angle, θ, at the z position where **B** has some lower value, $\mathbf{B}_o$. When the fractional change in **B** per orbit cycle is small, conservation of energy and momentum lead to a simple formula (Cecchi, 1990) for the angle of the "escape cone" within which the mirror is not strong enough to reflect the electron:

$$\sin^2\theta = |\mathbf{B}_o/\mathbf{B}_m| \tag{9.27}$$

Returning now to Fig. 9.10 to relate the magnetic-mirror effect to magnetron operation, we see that plasma electrons will be forced away from both the small and the large magnetron radii where **B** converges toward the magnet pole pieces. The plasma electrons will be

compressed by these mirrors toward an intermediate radius where **B** is uniform, and that is where the plasma and the ion bombardment of the target will be most intense. This effect can be reduced somewhat by designing a flatter **B** or by mechanically scanning the magnets back and forth during sputtering, although the latter solution is awkward.

The film-thickness nonuniformity that results from plasma compression in magnetrons can be avoided by moving the substrates around during deposition, as was done in dealing with point sources of evaporant in Sec. 4.6. One common deposition geometry utilizes the rectangular magnetron, a variation of the Fig. 9.10 design in which the disc is stretched to an arbitrary length in one direction so that the electrons follow an oblong "racetrack" $\mathbf{E}\times\mathbf{B}$ path above the target. When a rectangular magnetron is used in the Fig. 4.13 substrate-transport configuration, ±2 percent uniformity can be obtained over very large areas such as rolls of plastic film or sheets of architectural glass.

Localization of the plasma over the target by the magnetron's transverse magnetic field results in a much lower plasma density over the substrate than in the case of the planar diode (Fig. 9.5), and ion bombardment flux to the substrate is reduced proportionately per Eq. (9.20). This is desirable when the neutral sputtered particles alone carry sufficient kinetic energy to optimize film structure or when one wants to minimize the substrate heating that results from ion bombardment. In other cases, however, one may want to further increase film bombardment while retaining the low operating pressure of the magnetron. One way to do this is by "unbalancing" the magnets [28, 29] as shown in Fig. 9.13. There, the central bar magnet has been replaced by a smaller one that cannot pull in all the field lines emanating from the magnets in the ring. Some of these lines then curve away toward the substrate. Since electrons traveling parallel to **B** are not

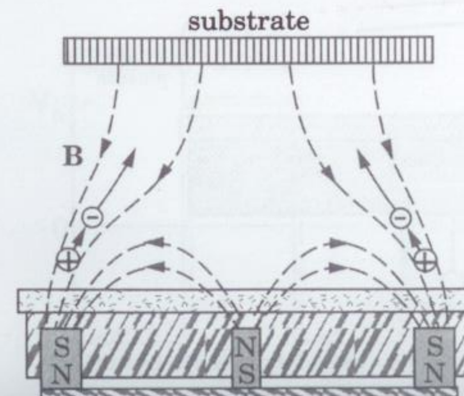

Figure 9.13 Plasma flow toward the substrate along magnetic field lines in an unbalanced magnetron.

acted on by **B**, they can escape along these field lines and toward the substrate, pulling positive ions along with them by ambipolar diffusion [Eq. (9.17)] and thus increasing ion flux to the substrate. The bombardment energy may then be increased if necessary by negatively biasing the substrate.

Another way to increase ion-bombardment flux to the film is to ionize the mostly neutral sputtered-particle flux during its transport to the substrate. This can be done as shown in Fig. 9.14, where an rf-powered coil is used to couple energy inductively into a secondary plasma downstream of the magnetron plasma [30]. The inductive coupling mechanism is discussed in Sec. 9.5.3. By increasing pressure to 4 Pa to increase sputtered-particle transport time and by using an 8- to 10-cm deep secondary plasma, 85 percent ionization of sputtered metal can be achieved [30]. This is much higher than the ionization fraction of the background Ar, because the ionization potential of metals is much lower. The ionized metal can then be accelerated into the substrate using negative bias. Metal-ion acceleration has an advantage over just Ar^+ acceleration in that it causes the depositing metal to arrive more perpendicularly to the substrate, thus reducing the problem of film buildup on the top corners of topography, which was illus-

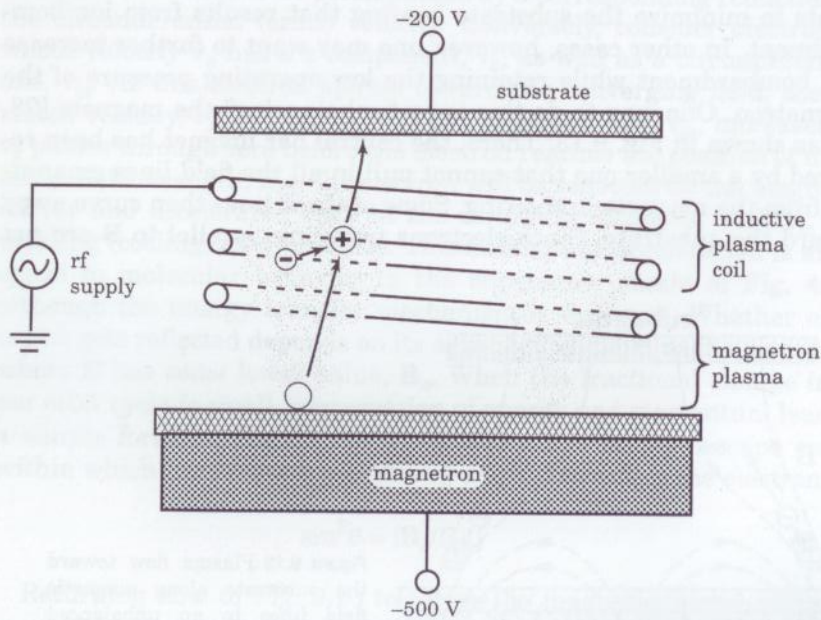

Figure 9.14 Ionization of sputtered particles using a secondary, inductively coupled plasma.

trated in Fig. 8.30. Cathodic-arc evaporation (Sec. 8.3) shares the advantage of high ionization fraction, but it suffers from the macroparticle problem.

9.4 Frequency Effects

We have so far focused on plasmas driven by dc electrical power, such as the vacuum arc (Sec. 8.3), the dc planar diode (Fig. 9.5), the thermionically supported diode (Fig. 9.7), and the dc magnetron (Fig. 9.10). DC operation requires that the surfaces of both electrodes be electrically conductive, including any sputter-target materials, substrates, or thin films that may be placed on them. The presence of insulating layers on the electrodes deflects dc plasma current into any surrounding conductive areas and thus leads to gross plasma nonuniformity or to plasma extinction. Insulating substrates can be placed elsewhere, parallel to the current flow path, but this tends to be an awkward and limited mode of operation. Therefore, when insulating materials are involved, ac power is usually employed so that power may pass through the insulator by capacitive coupling.

The effect of electrical drive frequency on capacitive coupling may be understood by considering the ignition of a planar-diode plasma when an insulating substrate is covering the driven electrode. For analytical simplicity, we will use a square-wave voltage symmetrical about ground, although the voltage would normally be sinusoidal. Let the voltage start on the negative swing of the cycle at $-V_o$, as shown at the left of Fig. 9.15. Initially, the substrate surface also floats to $-V_o$ so that most of the drive voltage is dropped across the gas space to ground. Then, a dc plasma ignites, and ion current starts to be drawn to the surface of the substrate across the cathode sheath just as in Fig. 9.5. How quickly the surface charges up positively due to this ion current is determined by the capacitor operative equation,

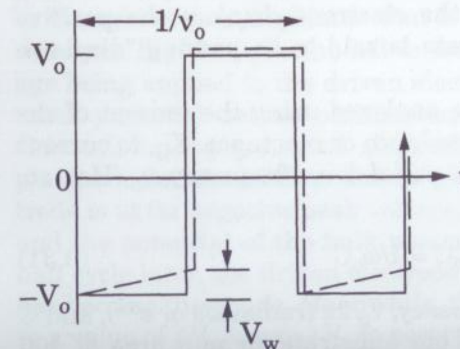

Figure 9.15 Voltage on the surface of an insulating substrate (dashed line) which is sitting on a planar-diode electrode being driven by a square-wave voltage (solid line) of frequency ν_o Hz.

$$I = j_+A = C(dV_w/dt) \tag{9.28}$$

where, using SI units,

I = current, A
j_+ = ion current density, A/m^2
A = area of the insulating substrate and of the electrode, m^2
C = capacitance, F
V_w = voltage drop across the capacitor, V
t = time, s

For a parallel-plate capacitor such as the substrate in question,

$$C = \varepsilon_o\varepsilon_d A/w \tag{9.29}$$

where ε_o = electrical permittivity of vacuum = $8.84{\times}10^{-12}$ F/m
ε_d = dielectric constant of the capacitor medium
w = plate spacing (substrate thickness here), m

During the initial chargeup, when $V_w << V_o$, dV_w/dt is constant and may be replaced by $\Delta V_w/\Delta t$. Then we may combine Eqs. (9.28) and (9.29) and rearrange to give the time to charge up to some ΔV_w:

$$\Delta t = 8.84{\times}10^{-12}\varepsilon\Delta V_w/j_+w \tag{9.30}$$

Taking the case of a 1-mm-thick quartz substrate ($\varepsilon = 3.8$) and the typical j_+ of 0.28 mA/cm^2 [which was calculated following Eq. (9.21)] and converting these to SI units, we find that ΔV_w rises to 100 V in only 1.2 µs. This means that if we wish to restrict substrate charging to a maximum of 100 V, we must reverse the voltage within 1.2 µs by operating at a drive frequency of 400 kHz. When V_o becomes positive, electrons immediately flow out of the plasma until the bulk plasma floats up to $+V_o$ plus the plasma potential, ΔV_p, of Fig. 9.3. These electrons neutralize the positive charge residing on the surface of the substrate so that it again starts from $\Delta V_w = 0$ when the next dose of ions arrives, as shown in Fig. 9.15. That is, the electrons *displace* the positive charge, and the capacitive substrate is said to be passing "displacement" current.

The above situation may also be analyzed using the concept of circuit impedance. The capacitive impedance or reactance, X_C, to current flow decreases with increasing *sinusoidal* drive frequency, ν_o (Hz), according to

$$X_C\ (\Omega) = 1/2\pi\nu_oC = 1/\omega_oC \tag{9.31}$$

where ω_o is the angular drive frequency, $\nu_o/2\pi$ (radians/s or s^{-1}), and C is in farads (F). The impedance of our substrate for unit area at 400

kHz is thus $1.2{\times}10^5\ \Omega{\cdot}cm^2$. This may be compared to the impedance of the plasma, which is largely in the cathode sheath and is resistive at this ν_o. For a typical sheath voltage of 1000 V, the sheath impedance is (1000 V)/($2.8{\times}10^{-4}$ A/cm^2) = $3.6{\times}10^6\ \Omega{\cdot}cm^2$. Considering the substrate and sheath as a voltage divider, this says that the *time-average* voltage drop across the substrate will be 3 percent of V_o, which is consistent with our Eq. (9.30) calculation in which the *maximum* substrate voltage drop was 10 percent of V_o. Operation at lower ν_o would result in too much of V_o being dropped across the substrate, causing plasma extinction, or causing the plasma to seek lower-impedance current paths, or causing plasma nonuniformity across the substrate due to variation in the substrate-electrode gap and therefore in capacitive coupling. When the depositing film itself is the largest capacitive impedance, as in the case of reactive sputtering or PECVD of insulating compound films onto conducting substrates, ΔV_w may have to be held to an even lower value to avoid electrical-breakdown damage across the film (see Exercise 9.8).

The above example illustrates the motivation to operate glow discharges at high frequency. Plasma drive voltage dropped across insulating layers can cause film damage, loss of ion-bombardment energy, plasma nonuniformity, or plasma extinction, and this voltage drop decreases with increasing frequency. However, other factors also influence the selection of drive frequency. We will see below that there is a distinct change in plasma behavior in crossing 1 MHz or so. The <1 MHz regime includes 60 Hz ac up through the audio range and through the low-frequency rf range and will be termed the low-frequency regime here. Above 1 MHz is the high-frequency regime. Later, in Sec. 9.5, we will examine operation in the microwave or UHF regime (> 300 MHz) as a means to drive an electrodeless discharge.

9.4.1 Low-frequency regime

At drive frequencies below 1 MHz or so, the planar-diode plasma may be thought of as a dc plasma that is periodically reversing polarity, as shown in Fig. 9.16. To the left is the sinusoidal waveform of the voltage being applied to the driven electrode, and to the right is the electrical potential versus position across the gap, L, from the driven electrode to the grounded electrode at the far right. At t = 0, the plasma looks identical to the dc plasma of Fig. 9.5: the driven electrode is at its negative peak voltage, $-V_o$, and is acting as the cathode, and the potential of the bulk plasma is floating ΔV_p above ground. A half cycle later, the driven electrode is at its positive peak voltage and has become the *anode*. Meanwhile, the plasma potential has floated up to a value of ΔV_p above $+V_o$ in accordance with the principle of Sec. 9.2

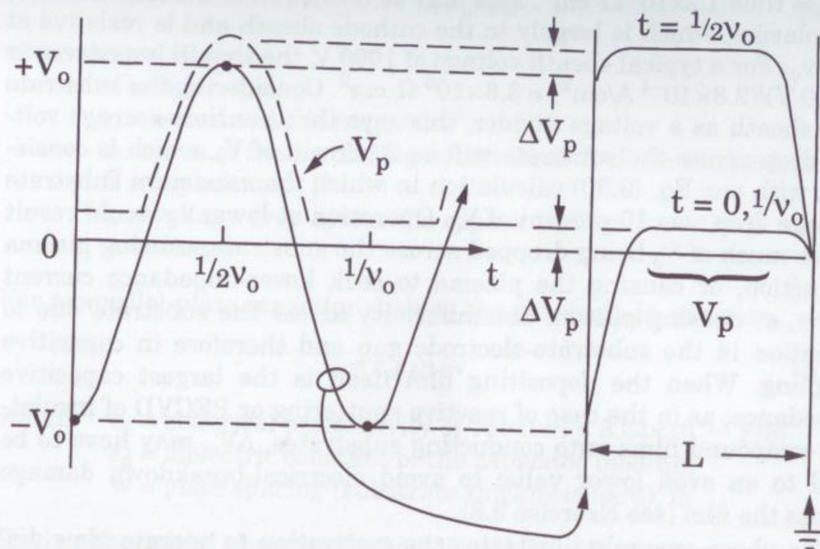

Figure 9.16 Voltages vs. time (left) and vs. position across the electrode gap, L (right), in a low-frequency planar-diode glow discharge. On the left, the solid waveform is the voltage applied to the electrode, and the dashed waveform is the plasma potential relative to ground, V_p.

that the bulk plasma is always more positive than the most positive of its containing surfaces. The plasma potential measured from ground, V_p, tracks the positive-going drive voltage essentially instantaneously as shown on its Fig. 9.16 waveform, because the mobile plasma electrons are quickly drawn into the positive-going electrode. Thus, at $+V_o$ the cathode sheath has shifted from the driven electrode to the grounded electrode. Then, as drive voltage decreases, V_p drops to maintain the ΔV_p criterion, by the flow of ions to ground. V_p eventually remains pinned at ΔV_p above ground when the drive voltage returns to the negative swing of its cycle. The resulting V_p waveform is essentially that of a half-wave rectified sinusoid because of the rectifying action of the sheaths, which pass electrons much more easily than ions.

What are the effects of the above behavior on film deposition? The low-frequency plasma is most often applied to plasma-enhanced CVD, with the substrate residing on one or the other electrode. First of all, for a drive waveform symmetrical about ground (no dc component), the experience of a film on either electrode will be the same. With regard to ion bombardment, either film will receive alternating bursts of low-energy ions across the anode sheath and high-energy ions across the cathode sheath, as the sheaths periodically swap places. This

leads to the commonly observed "bimodal" time-average ion-energy distribution at the electrodes of low-frequency plasmas [31]; that is, a low-energy hump at ΔV_p and a smaller high-energy hump near V_o. However, at high pressure, sheath collisions will distribute the high-energy hump to lower energies as discussed at the end of Sec. 9.2. Meanwhile during this oscillation, the plasma is being sustained by bursts of high-energy "beam electrons" (Sec. 9.3.1) which are emitted from the cathode and accelerated into the plasma across the cathode sheath. Thus, the beam-generated region of high electron-impact reaction rates (excitation, dissociation, ionization; see Sec. 9.1) also alternates between electrodes, and the degree of reaction localization at each electrode increases with pressure. These effects can be seen using time- and position-resolved monitoring of optical emission from electronically excited molecules [32], which relax rapidly ($<10^{-7}$ s) compared to the drive-cycle time, $1/\nu_o$.

Because of the rapid optical-emission decay time, the plasma *appears* to extinguish in the drive-voltage crossover region between the V_o peaks, where little excitation occurs because of the low energy of the beam electrons. However, electron temperature, $\tilde{T}_e$, and the free-radical population decay less rapidly, so whether a drop is seen in them depends on drive frequency, ν_o (and on pressure). The $\tilde{T}_e$ decay time may be estimated as follows. The electrons are cooled by elastic collisions with molecules, as discussed in Sec. 9.1, and this collision frequency is given by

$$\nu_e = c_e/l_e \tag{9.32}$$

where c_e and l_e are the electron mean speed and mean free path. At the typical $\tilde{T}_e$ of 3 eV, the mean electron kinetic energy is 4.5 eV [see discussion preceding Eq. (9.11)], and c_e is 1.3×10^8 cm/s by Eq. (8.7). By Eq. (2.22), $l_e \approx 4/p$ cm, where p is the pressure in Pa. However, the large electron-molecule mass disparity results in a low fractional energy transfer per head-on collision, which is $\gamma_m = 5.4\times10^{-5}$ for Ar, for example [(by Eq. (8.20)]. Thus, the characteristic time for electron thermalization to the gas T is

$$\tau_T\,(s) \approx 1/\nu_e\gamma_m = l_e/c_e\gamma_m = 6\times10^{-4}/p \tag{9.33}$$

or 6 μs at a typical PECVD operating pressure of 100 Pa. At drive frequencies low enough that the voltage crossover interval is longer than this time, the loss of electron energy causes the sheaths to collapse and thus causes ion bombardment to cease. Sheath collapse also means that any negative ions or negatively charged macroparticles that were trapped by the sheath's retarding field can now diffuse to

the film surface. The negative-particle problem will be discussed further in Sec. 9.6.3.

The population of the free radicals, some of which are film precursors, decays much less rapidly because these usually must reach a surface before reacting away. The characteristic time, τ_D, for diffusion across a length Λ with a diffusivity D may be found by rearranging Eq. (5.25). Taking $\Lambda = 1$ cm as typical, and using the D of Ar in Ar from Table 2.1 with a 1/p pressure dependence, we have

$$\tau_D = \Lambda^2/4D \approx 1.3\times10^{-5}p \qquad (9.34)$$

or 1.3 ms at 100 Pa. Thus, the free-radical supply to the surface will be unmodulated except at very low drive frequencies or pressures. Note that the pressure dependence of this decay time is opposite to that of the T_e decay time in Eq. (9.33).

9.4.2 Transition to high frequency

Two significant changes in plasma behavior occur as drive frequency, ν_o, crosses into the high-frequency regime above 1 MHz or so, although there appears to be no coupling between these changes. One is that plasma ions injected into the sheath no longer have enough time to cross to the surface within a half-cycle time, $1/(2\nu_o)$. The other is that a new electron-energy gain mechanism becomes operative, which involves reflection of bulk electrons off the oscillating sheath. These phenomena and their implications for film deposition will be discussed in turn below.

9.4.2.1 Ion transit time. Because ions are so much more massive than electrons, the electron-related assumption of instantaneous response to changes in sheath voltage at rf frequencies is not valid for ions. The time for an ion to cross a collisionless (low-pressure) sheath may be estimated by setting the force exerted on it by the sheath electric field, **E** [see Eq. (6.6)], equal to the force of accelerating its mass:

$$q_+\mathbf{E} = m_+(dv_+/dt) = m_+d(dx/dt)/dt \qquad (9.35)$$

Actually, **E** increases (more or less linearly) with distance from the plasma edge to the electrode surface, as seen in Fig. 9.3, but it will suffice here to give it a constant, average value of V_b/b across the sheath width, b. If one also neglects the injection velocity at the sheath edge [Eq. (9.17)] compared to the subsequent acceleration, integration of Eq. (9.35) gives for the characteristic ion transit time across the sheath (Exercise 9.9), in SI units:

$$\tau_+ = \sqrt{\frac{2m_+b^2}{q_+V_b}} \qquad (9.36)$$

For Ar^+ crossing a typical cathode sheath having $V_b = 1000$ V and b = 1 cm (see Fig. 9.4), we find that $\tau_+ = 0.29$ μs. For some ions to bombard the surface with energy corresponding to nearly the full sheath voltage, they must cross the sheath while the drive voltage is near its peak, or within a radian or so of the voltage cycle; that is, $\nu_o \le 0.6$ MHz. At significantly higher ν_o, the ions will take many cycles to cross, experiencing a burst of acceleration during each cathodic phase and then coasting during each anodic phase, so that they arrive with an energy corresponding to the *time-average* sheath voltage drop. For the V_p waveform of Fig. 9.16, this average is V_o/π. However, we will see in the next section that in the high-frequency regime, the waveform becomes more sinusoidal so that the average becomes $V_o/2$. We will also see that a lower V_o is required in the high-frequency regime. The result of the time averaging and the lower V_o is that *the maximum ion-bombardment energy is much lower in the high-frequency regime.*

The effect of the ion-energy transition is dramatically reflected in the intrinsic stress of silicon nitride films deposited by PECVD over a range of drive frequencies, as shown in Fig. 9.17. These films are tensile at >1 MHz due to a chemical mechanism which will be discussed in Sec. 9.6.4.2. However, at <1 MHz, the "ion-peening" effect of high-energy bombarding ions, as expressed in Eq. (8.33), overcompensates for the chemical effect and results in compressive stress. In principle, one could operate at an intermediate frequency to obtain zero stress. However, this is an awkward frequency regime due to the changing plasma behavior (Sec. 9.4.2.2) and also due to power-coupling problems (Sec. 9.4.4). Instead, one can use a mixture of a high and a low

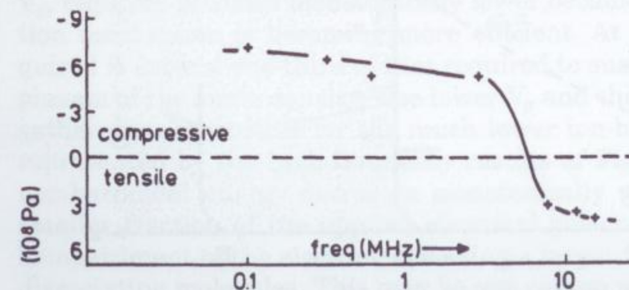

Figure 9.17 Effect of drive frequency on stress of PECVD silicon nitride films deposited from SiH_4 + NH_3 + N_2. (Source: Reprinted from Ref. 33 by permission.)

frequency in the power proportion appropriate to give zero stress (see Sec. 9.4.4).

9.4.2.2 Electron energy gain. We now turn to the second change in plasma behavior that occurs upon crossing into the high-frequency regime. Recall that in the dc and low-frequency regimes of plasma drive power, the plasma is sustained by secondary electrons that are generated by ion impact on the cathode and accelerated across the sheath (the "beam" electrons). While this mechanism is still operative at high frequency, another electron-energy gain mechanism becomes more important: sheath oscillation. At any frequency, the sheath thickness expands as the driven electrode swings negative, because of the need to expose more volume of positive space charge to accommodate the increased voltage drop [(see derivation of Eq. (8.11)]. Then it contracts again on the positive swing and proceeds to oscillate in thickness in a roughly sinusoidal manner, with some harmonic content due to various nonlinearities [14]. Figure 9.18 shows the ion and electron concentrations, n_+ and n_e, versus position across the sheath at an intermediate point of time in the cycle where the sheath has some intermediate thickness, b(t), between the anodic and cathodic limiting thicknesses, b_a and b_c. On the plasma side of b(t), we have n_e

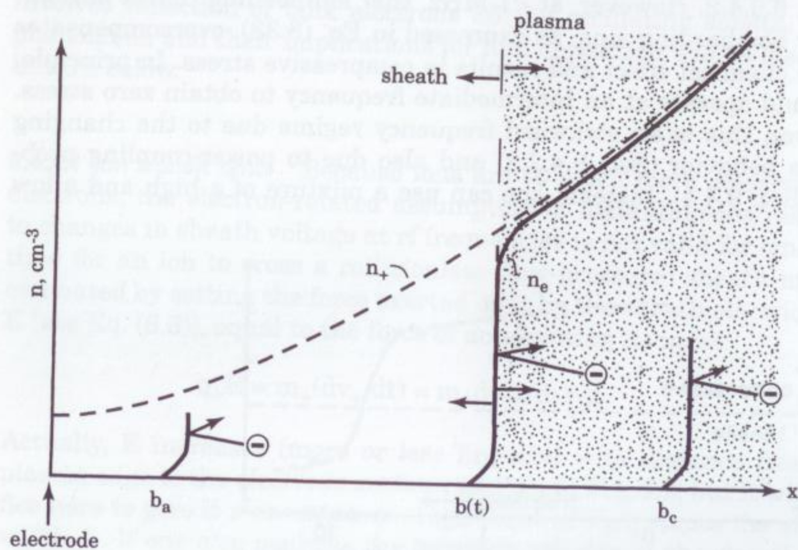

Figure 9.18 Ion and electron concentrations across the rf sheath edge, b(t), which is oscillating between b_a and b_c limits and from which plasma electrons are reflected. (Source: Adapted from a figure in Ref. 14.)

$\approx n_+$ in accordance with the principle of plasma charge neutrality, while at b(t), n_e drops precipitously as we enter the positive-space-charge region of the sheath. Meanwhile, n_+ decreases slowly toward the electrode as the ions become accelerated toward it [Eq. (4.35) at constant flux].

Now, recall from the discussion of Fig. 9.3 that the sheath develops in the first place because of the high velocity of the electrons relative to the ions. The sheath provides a potential barrier for electrons, which reduces their escape flux so that it becomes equal to that of the ions. Thus, all but the fastest electrons in the tail of the electron-energy distribution are reflected from the sheath edge and returned to the plasma. If the sheath happens to be expanding when a particular plasma electron reflects off it, that electron will receive a "swat" analogous to that imparted to a ball by a tennis racket, and it will return to the plasma *hotter*. At the usual rf frequency of $\nu_o = 13.56$ MHz, the energy gain per swat is only 0.1 eV or so (see Exercise 9.10), but the electron soon bounces off a gas molecule and returns for another swat. Statistically, some of the electrons will gain enough energy through successive favorable collisions to ionize molecules, and the plasma is thus sustained by this *volume* energy-gain mechanism without the need for beam electrons from the surface. This is considered to be "ohmic" heating because it is dominated by collisions. The advancing-sheath mechanism is analogous to the heating of a gas by an advancing piston during gas compression. The electrons being swatted are sometimes described as "wave-riding" on the advancing sheath, but this is misleading because it does not account for the multiple bounces which are necessary for reaching ionizing energy.

The energy gained from sheath oscillation is proportional [34] to the square of the sheath velocity and thus to ν_o^2. For $\nu_o < 1$ MHz or so, the electron energy gained in this way is insufficient to sustain the plasma, while for increasing ν_o above 1 MHz, the drive voltage, V_o, required becomes monotonically lower because the sheath-oscillation mechanism is becoming more efficient. At 13 MHz, the V_o required is around one-third of that required to sustain a low-frequency plasma of the same density. The lower V_o and the ion transit time together are responsible for the much lower ion-bombardment energy represented by the high-frequency results of Fig. 9.17. Because ion-bombardment energy decreases monotonically with increasing ν_o, a smaller fraction of the applied electrical power is dissipated in ion bombardment of the electrodes, leaving a larger fraction available for dissociating molecules. This may be one reason why plasma chemical reactions are often observed to increase in efficiency with ν_o, as in the case of amorphous Si PECVD rate [35]. Another difference in V_o behavior in the high-frequency regime is that V_o rises much more

steeply with power than at low frequency, being roughly proportional to plasma current.

Other characteristics of the high-frequency sheath are of interest as well. Calculations of the collisionless (low-pressure), high-frequency, rf **sheath thickness,** b(t) in Fig. 9.18, show it to be roughly the same [14] as in the dc case [Eq. (9.23)] for a given voltage drop. When the collision rate in the sheath is high and the voltage drop is also high, b(t) decreases by at most 50 percent. In contrast to the dc plasma, here the time-average sheath thickness is the *same* as that of the "dark space" observable at the edge of the glow, since the energetic electrons which produce the glow are being generated at the sheath edge. Electrically, this sheath looks much like a capacitor, because at high rf frequencies the capacitive impedance is much less than the resistance represented by the flux of ions across it, as may be seen by examining the calculation following Eq. (9.31). In other words, the displacement of electrons as the capacitor's plate spacing, b(t), oscillates represents a **displacement current** that is much higher than the dc ion current flowing in parallel to it. Across a capacitor, the current is at its peak when the sinusoidal applied voltage is crossing its midpoint and is therefore at its maximum rate of rise, as seen in Eq. (9.28). That is, current *leads* voltage by a quarter cycle or 90°. This is different from the dc and low-frequency plasmas, where the sheaths were resistive because they mostly passed ion current in phase with the sheath voltage. Note that there is no power dissipation in a capacitor. Power is dissipated only by the in-phase component of the I×V vector product. Therefore, there is a large excess of current flowing through the high-frequency rf plasma—the displacement current—which is not carrying power but which still must be handled by the power circuit. This fact is important in driving these plasmas, as we will see in Sec. 9.4.4. Another consequence of the relative immobility of the ions at high frequencies is that the **plasma potential,** V_p, does not track the drive voltage in the half-wave rectified manner of Fig. 9.16, as it did at low frequencies. Instead, it oscillates in a roughly sinusoidal manner with the sheath capacitance [31], between limiting values of ΔV_p above ground and ΔV_p above the most positive excursion of the driven electrode. The maximum (collisionless) ion-bombardment energy is then determined by the time-average value of this oscillating V_p.

The sheath-edge and the beam mechanisms of electron energy gain are actually both operative at high frequency [36], and the plasma is said to be in the "α" or "γ" mode when the first or second mechanism is dominant, respectively, since α and γ are the historical symbols for the volume and surface secondary-electron emission coefficients. The beam mechanism increases in relative importance at higher power where sheath voltage is higher.

9.4.3 RF bias

The low impedance of capacitors in the high-frequency regime [see Eq. (9.31)] allows rf power to be coupled to the driven electrode through a series capacitor as shown in Fig. 9.19*a*. This is an important and widely used technique which greatly improves plasma control. Consider the typical "asymmetric" plasma geometry of Fig. 9.19*a*, in which the area of the grounded "electrode" is much larger than that of the driven electrode because it includes not only the substrate and its

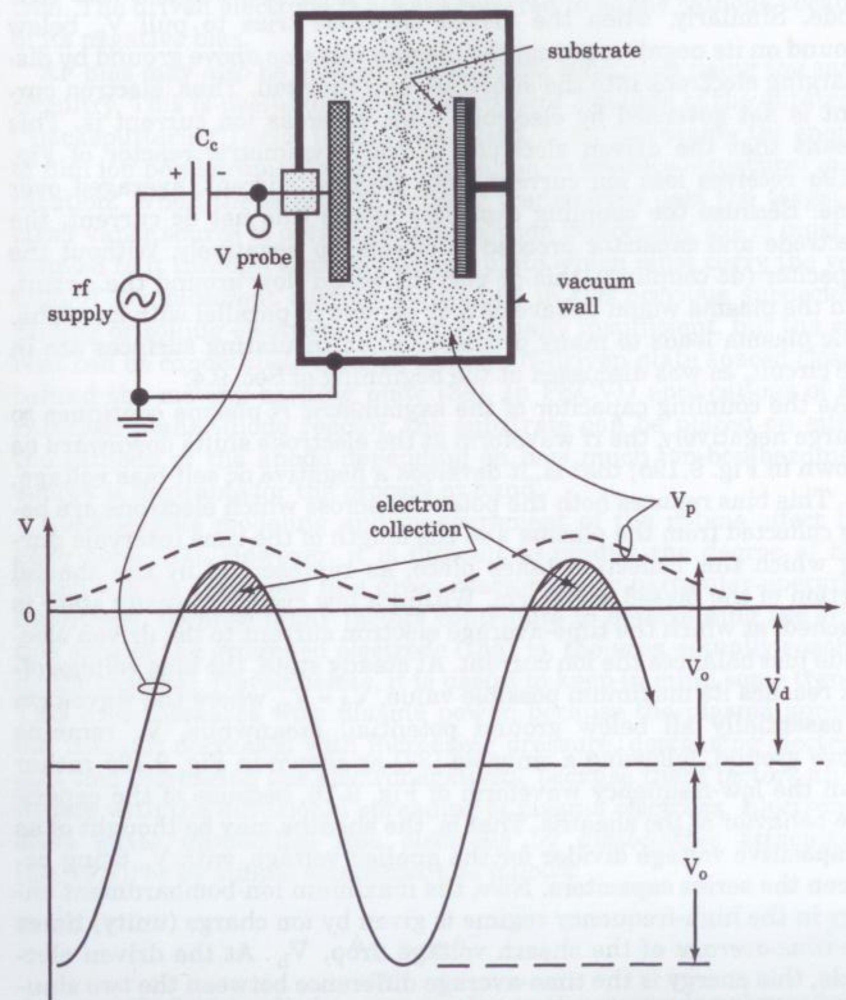

Figure 9.19 DC self-biasing of a capacitively coupled rf waveform due to plasma-electrode asymmetry.

platform but also all of the vacuum-wall surface that is reached by the plasma. Now, recall that the ion flux or current density, j_+, injected into the sheath and arriving at the surface is determined only by plasma density and $\tilde{T}_e$ through Eq. (9.20). If these two quantities are reasonably uniform throughout the plasma, then the electrode of smaller area, A, will receive less ion current, $I_+ = j_+A$, than will the larger electrode. Conversely, electron current to a surface is determined by the plasma potential, V_p, relative to that surface. When the driven electrode tries to become more positive than V_p on its positive swing, the plasma instantly floats above it by discharging electrons into that electrode. Similarly, when the driven electrode tries to pull V_p below ground on its negative swing, the plasma remains above ground by discharging electrons into the substrate and the wall. Thus, electron current is not governed by electrode area, whereas ion current is. This means that the driven electrode in the asymmetric reactor of Fig. 9.19*a* receives less ion current than electron current, averaged over time. Because the coupling capacitor blocks this net dc current, the electrode and capacitor proceed to charge up negatively. Without the capacitor (dc coupling), this dc current would flow around the circuit, and the plasma would behave as a dc plasma in parallel with an rf one. A dc plasma leads to many problems when insulating surfaces are in the circuit, as was discussed at the beginning of Sec. 9.4.

As the coupling capacitor of the asymmetric rf plasma continues to charge negatively, the rf waveform at the electrode shifts downward as shown in Fig. 9.19*b*; that is, it develops a negative dc self-bias voltage, V_d. This bias reduces both the potential across which electrons are being collected from the plasma and the length of the time intervals during which this collection takes place, as represented by the shaded portion of the biased waveform. Within a few cycles, a steady state is reached, at which the time-average electron current to the driven electrode just balances the ion current. At steady state, the bias voltage often reaches its maximum possible value, $V_d \approx V_o$, where the waveform is essentially all below ground potential. Meanwhile, V_p remains above ground, following a sinusoid [37] as shown in Fig. 9.19*b* rather than the low-frequency waveform of Fig. 9.16, because of the capacitive behavior of the sheaths. That is, the sheaths may be thought of as a capacitive voltage divider for the applied voltage, with V_p being between the series capacitors. Now, the maximum ion-bombardment energy in the high-frequency regime is given by ion charge (unity) times the *time-average* of the sheath voltage drop, $\bar{V}_b$. At the driven electrode, this energy is the time-average difference between the two sinusoids of Fig. 9.19*b*, which is $V_o/2$ for an applied waveform symmetrical about ground and V_o for the fully biased case. For intermediate biases, then, we have

$$\bar{V}_b = (V_o - V_d)/2 \qquad (9.37)$$

where V_o is always positive and V_d negative. At maximum bias, ion-bombardment energy elsewhere has been reduced to a minimum equal to the potential drop of a dc anode sheath, ΔV_p from Fig. 9.5. This is a very desirable situation for sputtering, because it concentrates the ion energy on the target where it is wanted and eliminates unwanted sputtering elsewhere. It is the standard configuration for rf sputtering of insulating materials using either the planar diode or the magnetron. The driven electrode is always referred to as the cathode because of its negative bias.

RF bias may also be applied to insulating *substrates* using the same circuitry. This is useful for ion-bombardment cleaning of the substrate ("backsputtering") prior to film deposition, or for increasing the energy of film ion bombardment during deposition to produce structural modification. When the substrate is being transported past the target or other vapor source to obtain good deposition uniformity, the rf must be coupled to it through a metal backing plate which must carry the very high rf displacement current mentioned in the previous subsection. Sliding or rolling electrical contact is usually insufficient, but the current can be *capacitively* coupled from an rf-driven plate spaced closely behind the moving backing plate [38]. In PECVD applications of the rf-biased planar-diode reactor, the substrate can be placed on either the cathode or the anode depending on how much ion-bombardment energy is desirable for the process at hand.

Considerable modeling and measurement of the rf-bias effect has been done [37]. However, it is difficult to predict the degree of bias which will be developed in a given reactor under particular operating conditions, because many factors contribute to determining the *effective* area of the grounded electrode (that is, the area actually reached by the plasma). Nevertheless, it is useful to keep in mind some trends. This area increases with plasma power, because the plasma spreads out more. It decreases with increasing pressure, decreasing electrode gap, and increasing gas electronegativity, because these factors all interfere with the diffusional spreading of plasma electrons. Electronegative gases immobilize free electrons by dissociative attachment [Eq. (9.5)] or by simple attachment as follows:

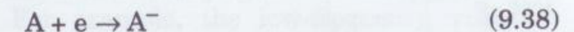

$$A + e \rightarrow A^- \qquad (9.38)$$

A magnetic field applied perpendicular to the electrodes also reduces effective area by inhibiting the radial diffusion of electrons across the field lines. In the low-frequency regime, plasma spreading is further

reduced because the perpendicularly directed beam electrons dominate plasma excitation [39].

RF bias may be hard to predict, but it is easy to measure using a high-impedance, high-voltage rf oscilloscope probe on the cathode vacuum feedthrough as shown in Fig. 9.19*a*. It is useful to measure both V_o and V_d in this way so that the fractional bias may be determined. Alternatively, V_d alone can be measured with the circuit of Fig. 9.20. Here, the inductor or choke, L, blocks the rf and passes the dc, since the impedance of an inductor is given by

$$X_L(\Omega) = 2\pi\nu_o L = \omega_o L \tag{9.39}$$

where L is the inductance in henrys (H). Meanwhile, the capacitor shunts any remaining rf around the resistive voltage divider because of its low rf impedance given by Eq. (9.31). The resistive divider reduces V_d to a conveniently measured level. At the conventional rf frequency of 13.56 MHz, the impedances of the L and C shown are 3.4 kΩ and 12 Ω, respectively, so that only 0.4 percent of the rf voltage appears across the capacitor and resistive divider.

For maximum bias where $V_d \approx V_o$, an upper limit on ion current, I_+, to the biased electrode can be estimated by assuming that all of the

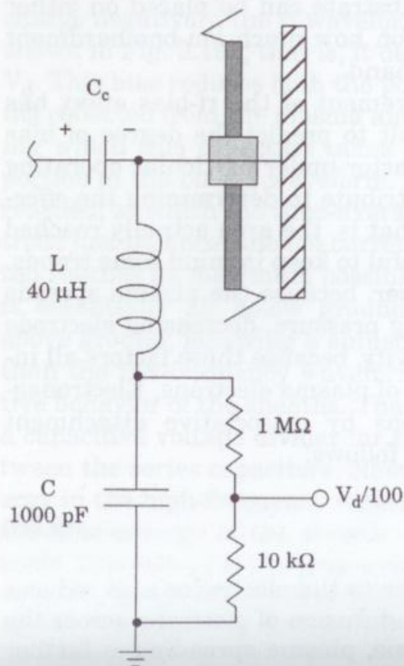

Figure 9.20 DC-bias probe with L and C sized for 13-MHz operation.

applied power, P, goes into ion acceleration across the cathode-sheath voltage drop, V_b; that is,

$$P = I_+ V_b \approx I_+ V_d \approx I_+ V_o \tag{9.40}$$

This assumption is most reasonable for monatomic gases at low pressure and high power [40], where the fraction of power dissipated in other ways is smallest.

9.4.4 Power coupling

The efficient and accurate delivery of power to a plasma load requires special techniques that vary considerably with the drive-frequency regime. It is important to understand these techniques when designing or tuning plasma-deposition equipment and when attempting to measure or reproduce the power delivered to a process. The various techniques will be outlined below, beginning with the simplest (dc) case and then proceeding to the low-frequency, high-frequency, and microwave regimes.

The **dc power** delivered to a load is simply the product of the current through the load and the voltage drop across it:

$$P\,(\mathrm{W}) = IV_o \tag{9.41}$$

To maximize the power delivered at *any* frequency, the load impedance, X_l, must be matched to the source impedance of the power supply, X_s. In the dc case, X_l is just a resistance, $X_l = R = V_o/I$, because the plasma is a resistive load. At any frequency, X_s is the V/I slope of the power supply's output. For example, a 1-kW dc supply rated at 1000 V and 1 A has X_s = 1000 Ω. If X_l is also 1000 Ω, the full rated power of the supply can be delivered. For $X_l < X_s$, the power supply will reach its current limit before full voltage is developed, whereas for $X_l > X_s$, it will deliver less than its rated current at maximum voltage. Good dc power supplies designed for driving plasmas are impedance-matched to the expected load and also have constant-power and constant-current control, arc protection, high-voltage pulses for plasma ignition, and safety interlocks.

RF power supplies for both the low- and high-frequency regimes have a standard source impedance of 50 Ω, which is much lower than the typical plasma X_l. For example, the low-frequency, resistive sheath discussed after Eq. (9.31) has R = 36 kΩ for a 100 cm^2 area. A high-frequency, *capacitive*, rf sheath 3 mm thick and 100 cm^2 in area has C = 2.9×10^{-11} f (29 pf or "puffs") by Eq. (9.29) and X_C = 400 Ω at 13.56 MHz by Eq. (9.31). This impedance mismatch is remedied in the

low-frequency case by inserting between the power supply and the load an impedance-matching transformer with a 50 Ω primary winding and a secondary winding matched to the X_l of the plasma.

In the **high-frequency** regime, two complications arise with this simple approach. One is that transformers do not work well, because their inductive coils develop too high an impedance [Eq. (9.39)], and because there is too much capacitive shunting across the coils [Eq. (9.31)]. Also, the plasma is now largely capacitive, and the resulting large displacement current which was discussed in Sec. 9.4.2.2 must be blocked from the power supply. This out-of-phase current represents "reflected" power, which would overload the supply and prevent it from delivering its rated power. Both of these problems can be solved by inserting an L-C matching network [41] such as the "π" network shown in Fig. 9.21. In a crude analysis of the operation of this network, variable capacitor C_1 is tuned to the 50-Ω source impedance, or about 200 pf at 13 MHz [Eq. (9.31)], and C_2 is tuned to the 400-Ω load impedance, or about 25 pf. In the inductor, L, V leads I by 90°, just the opposite of a capacitor, so when $X_L = X_C$, the I-V phase angle is restored to zero. Then, the network-plus-plasma looks like a resistive load from both ends, so the reflected power drops to zero. The L needed to match $(C_1 + C_2)$ is (0.7 + 5.6) μH at 13 MHz [Eq. (9.39)], and an additional amount is required to account for the C of the plasma and C_c in series. A coil suspended in air makes a suitable rf inductor, and

$$L\,(\mu H) = 0.024 j^2 \phi \tag{9.42}$$

where j is the number of turns and ϕ is the diameter in cm. In actual network operation, there is considerable coupling between C_1 and C_2, so they must be tuned together to the point of zero reflected power. Forward and reflected power are usually measured separately on 50-Ω,

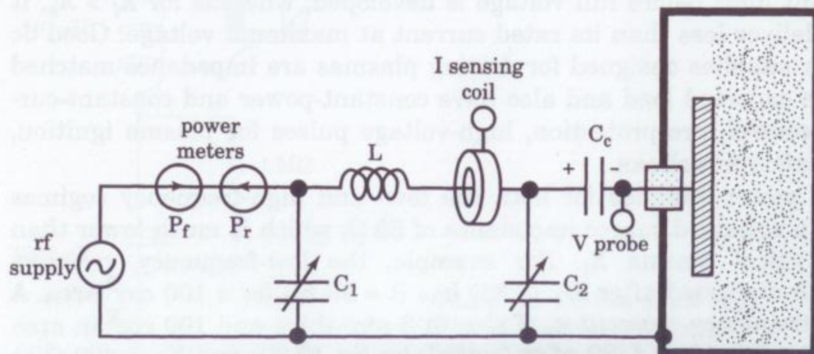

Figure 9.21 Typical matching network for high-frequency rf plasma coupling.

in-line power meters such as those manufactured by Bird and shown in Fig. 9.21. Reflected power may also be fed back to motor-driven capacitors for automatic tuning. This is useful when plasma conditions are being changed often, since that affects tuning.

L-C networks are operable from 1 to 100 MHz or so, but 13.56 MHz is generally used for high-frequency rf plasmas, because it is one of the frequencies assigned by the United States Federal Communications Commission (the FCC) for industrial use. Stray radiation from equipment operating at other frequencies can interfere with radio communications. Radiation in the low-frequency regime is less of a problem, because the wavelength is so much longer than typical equipment dimensions that the equipment does not make a very good radiating antenna. **Radio-frequency interference** (RFI) at high frequency can be a problem for electronics being used with the plasma process, such as vacuum gauges and mass flow controllers. This can be minimized [42] by first enclosing all rf-hot equipment in grounded metal boxes or screens (Faraday cages), which is good safety practice, anyway. Also, all electronics units and the rf supply should have only one ground lead each, and these leads should be brought to a common point of known good ground to eliminate rf ground loops. At high powers, the ground leads are best made of Ag-plated Cu sheet to give the largest surface area of high conductance, since at rf frequencies, current is carried near the surface of a conductor due to the "skin effect."

The **skin effect** is a result of the exponential attenuation of electromagnetic radiation upon entering a conductive medium. The transverse **E** field of the radiation transfers energy to the conducting charges so that the oscillation of **E** becomes damped. The effect limits the depth to which rf or microwave fields or light can penetrate any conductor, including *plasmas*, as we will see in Sec. 9.5. Light attenuation is expressed in Beer's law [Eq. (4.49)]. For rf, the characteristic depth at which **E** has been attenuated to 1/e is known as the "skin depth" [43],

$$\delta_s\,(\text{m}) = \sqrt{\frac{\varepsilon_o c_o^2}{\pi s \nu_o}} = \sqrt{\frac{2.54\times10^5}{s \nu_o}} \tag{9.43}$$

where c_o is the speed of light, s is the conductivity of the medium (S/m), ν_o is the radiation frequency (Hz), and all units are SI. For the most conductive metal, Ag, $s = 6.3\times10^7$ S/m at room T, so $\delta_s = 17$ μm at 13 MHz.

In the matching network of Fig. 9.21, there can be substantial **power losses** in the inductor and in the lead wire connecting it to the

plasma electrode. These losses are due to the skin effect coupled with the fact that the circulating displacement current may be ~100 A. The inductive coil and the capacitive plasma sheath essentially form a resonant or "tank" circuit in which a large amount of electrical energy sloshes back and forth, at a resonant angular frequency of $1/\sqrt{LC}$, between storage in the magnetic field of the coil when it is at peak current and storage in the electric field of the sheath when it is at peak voltage. When the absolute power delivered to the plasma needs to be known for purposes of process transfer, scaling, or modeling, these coupling losses must be subtracted from the net forward power measured on the upstream power meters of Fig. 9.21. A qualitative evaluation of whether power loss is significant and where it is occurring can be made by running the plasma for awhile and then turning off the power, *disconnecting* the power supply for safety, and quickly feeling around the matching network and vacuum feedthrough for hot spots.

For quantitative evaluation of power losses, the wiring's series resistance, R_s, at ν_o can be determined [44] by measuring its current with the sensing coil shown in Fig. 9.21 (a "Rogowsky" coil or "current donut"). Calibrated current-sensing coils are manufactured for various ν_o ranges. When the circuit is driven by the power supply *without* a plasma (gas evacuated), power (P) losses can occur only in the wiring, so that R_s is readily determined from

$$P = P_f - P_r = I_r^2 R_s \tag{9.44}$$

where P_f and P_r are the forward and reflected power, and I_r is the root-mean-square current, which is $\sqrt{2}$ times the peak current in the case of a sinusoid. Then, with the plasma operating, the power loss is $I_r^2R_s$, and the difference between that and the power measured on the meters, $(P_f - P_r)$, is the power dissipated in the plasma.

Sometimes, one wants to use **mixed drive frequencies,** ν_o; that is, to apply low-ν_o and high-ν_o power to the plasma simultaneously, such as for controlling the proportion of high-energy ion bombardment in PECVD, as discussed in Sec. 9.4.2.1. To do this, one can connect the matching networks of both power supplies to the same electrode, provided that the two power sources are sufficiently decoupled from each other [45]. The coupling capacitor, C_c, of Figs. 9.19 through 9.21 will suffice to keep the low-ν_o power from feeding back into the high-ν_o source because of its high X_C at the lower ν_o. Similarly, a series inductor placed between the low-ν_o matching transformer and the electrode will block high-ν_o power because of its high X_L at the higher ν_o.

In the **microwave frequency regime** (above 300 MHz), still other power-coupling techniques must be employed. At such high frequencies, the L-C network of Fig. 9.21 does not behave well, because the X_C

between inductor coils becomes as low as the coil's X_L, and the X_L of the capacitor lead wires becomes as low as the capacitor's X_C. That is, inductors start to look like capacitors and vice versa. Also, radiation is increased because of the short wavelength,

$$\lambda = c_o/\nu_o \tag{9.45}$$

which is 12 cm at the FCC-assigned industrial microwave ν_o of 2.45 GHz (2450 MHz). Therefore, it is important to transmit microwave power in tightly shielded and firmly connected coaxial cables or hollow metal waveguide tubes. The latter have lower transmission loss but are more awkward because of their rigidity. Both phase and impedance matching to the plasma load are necessary just as in the high-ν_o rf regime. Phase is tuned with a slider-adjustable length of rigid transmission line, and impedance is tuned by adjusting the proximity of a ground plane (a "tuning stub"). Because of the short λ, it becomes easy to launch a microwave beam into the plasma through a dielectric vacuum wall such as glass or ceramic. This can be done from a waveguide or from an antenna, and some specific examples will be given in the next section.

9.5 Electrodeless Excitation

We have seen in the previous two sections that glow-discharge-plasma excitation using electrodes always requires a high-voltage sheath to accelerate electrons to ionizing energy. While this sheath is useful when high ion-bombardment energy is desired at the surface, it also harbors some problems; namely, it can cause undesired sputtering, it consumes much power in accelerating ions, and it strongly limits the power and plasma density achievable. As pointed out in connection with the hollow-cathode effect of Fig. 9.6, high power density ultimately leads to arc breakdown at the cathode. Conversely, electrodeless excitation can avoid the high-voltage sheath and can therefore achieve ~100 times higher plasma density in the glow-discharge regime, thus providing much higher concentrations of active species for film deposition, with gas ionization fractions approaching unity when pressure is low enough. Because there is no high-voltage sheath, these ions bombard the film with low energies of ~10 eV, which is within the desirable energy window for rearranging surface atoms without doing subsurface damage (Sec. 8.5). Since many electrodeless techniques can also operate at very low pressures approaching the molecular-flow regime (Kn > 1), they can provide a highly directed flux of ionic depositing species, and this substantially reduces self-shadowing when coating surfaces having rough topography.

We will examine below several ways of accomplishing electrodeless excitation. All of these involve coupling rf or microwave energy through a dielectric vacuum wall from an external coil or antenna. Since the plasma is most intense nearest to this external coupler, the uniform distribution of active species over large film areas is often a problem. The equipment also tends to be more expensive than that of the parallel-plate reactor. However, since electrodeless plasmas are relatively new in thin-film deposition, their various pros and cons compared to more traditional plasmas are still in the process of assessment.

9.5.1 Microwaves

The wavelength of electromagnetic radiation at the industrial microwave frequency of 2.45 GHz is only 12 cm [Eq. (9.45)], so microwave energy can easily be beamed into a plasma from an external antenna or waveguide. The intervening vacuum-wall material needs to be an electrical insulator (a dielectric) for microwave transparency, and it is typically borosilicate glass, quartz, sapphire, or ceramic. One of the simplest of plasma couplers is the metal **quarter-wave cavity** [46] shown in Fig. 9.22. When the cavity is (1/4)λ long, grounded on one end, and driven from the coaxial-cable voltage at the other end, a standing wave develops as shown in the plot of the wave's transverse electric field, **E**. This is similar to the standing wave that develops in an organ pipe. Because this is a resonant situation, **E** can become quite large, and when it is large enough within the glass tube, the gas therein breaks down. Active species formed in the resulting plasma are transported downstream in the flowing gas and can be used in film-forming reactions with other species supplied downstream either by evaporation or as gases. Another way to activate a microwave plasma in a tube involves the launching of **"surface waves"** in the plasma using external electrodes [47]. The waves propagate along the tube, dissipating power in the plasma. Plasmas are rich in wave phenomena, as we will see below. Surface-wave devices may be operated over a wider range of drive frequency than resonant cavities, and they are less sensitive to changes in gas pressure or composition. They can also be operated at very high plasma density of $n_e > 10^{12}/cm^3$, but at most, one-half of the applied power can be coupled into the plasma, which is a distinct disadvantage.

The pressure effect on microwave plasma excitation can be understood by first considering the microwave **E** field acting on a free electron in *vacuum*. Figure 9.23*a* shows the **E** field of a microwave oscillating as $\mathbf{E} = \mathbf{E}_0\cos(\omega_0 t)$, as did the light wave of Eq. (4.44). The force exerted on the electron by **E** accelerates it parallel to **E** in accor-

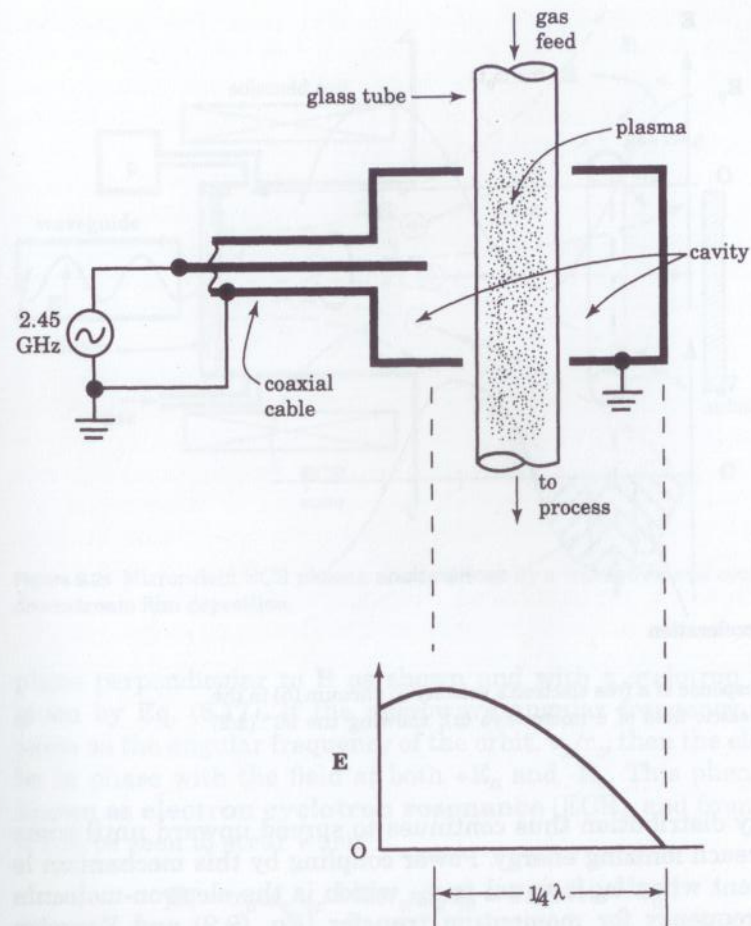

Figure 9.22 Typical quarter-wave microwave cavity for plasma coupling. (Tuning adjustments not shown.)

dance with Eq. (9.35) (written for ions), and the resulting electron velocity versus time, $v_e(t)$, is shown in Fig. 9.23*b*. When **E** crosses zero and reverses, v_e reaches its maximum negative value and begins decelerating, finally reversing direction and reaching another maximum when **E** again crosses zero. Thus, **E** and v_e are phase-shifted by 90° (π/2), and there is *no net energy gained* by the electron. This is analogous to the case of inductors and capacitors, where voltage leads or lags current by 90° so that there is no power dissipation (Sec. 9.4.4). When gas is present in the microwave field, however, electrons change their directions in collisions with molecules, and some of them will shift their phase so as to become further accelerated in **E**. The elec-

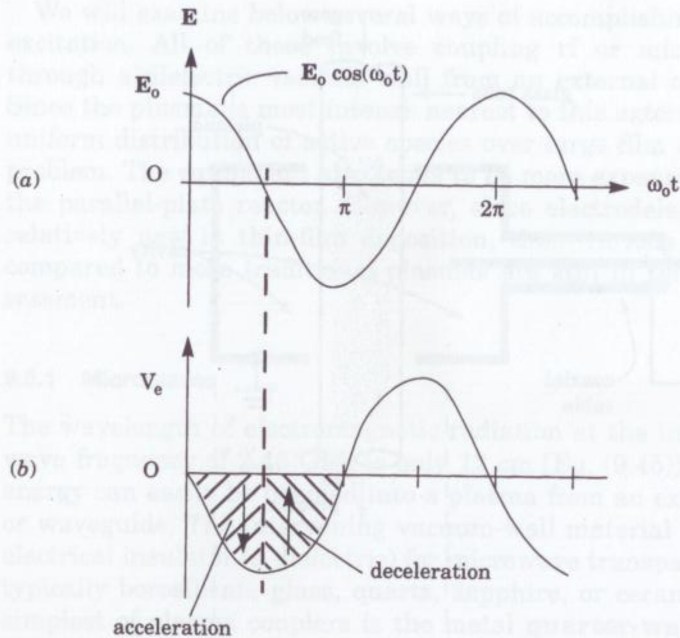

Figure 9.23 Response of a free electron's velocity in vacuum (*b*) to the oscillating electric field of a microwave (*a*), showing the 90° ($\pi/2$) phase shift.

tron-energy distribution thus continues to spread upward until some electrons reach ionizing energy. Power coupling by this mechanism is most efficient when ω_o is equal to ν_e, which is the electron-molecule collision frequency for momentum transfer [Eq. (9.9) and Exercise 9.11] (Cecchi, 1990; p. 44). However, with proper tuning, microwaves can be coupled to plasmas with little reflected power over a wide range of ν_e/ω_o (that is, over a wide range of pressure for a given ω_o). In the low-pressure limit of this range, there are not enough collisions, and in the high-pressure limit there are so many that too much energy is lost in momentum transfer. This pressure behavior is similar to the Paschen curve (Fig. 8.4) for gas breakdown in a dc field, although in the present case the low-pressure limit involves the electron's phase rather than its mean free path.

Collisions are not needed to change the electron phase if a strong enough magnetic field, **B**, is established parallel to the direction of the microwave beam and thus perpendicular to the **E** field. Figure 9.24 shows microwaves being beamed through a dielectric window into a plasma chamber containing a **B** field supported by an external solenoid coil. Electrons accelerated perpendicular to **B** by **E** will orbit in a

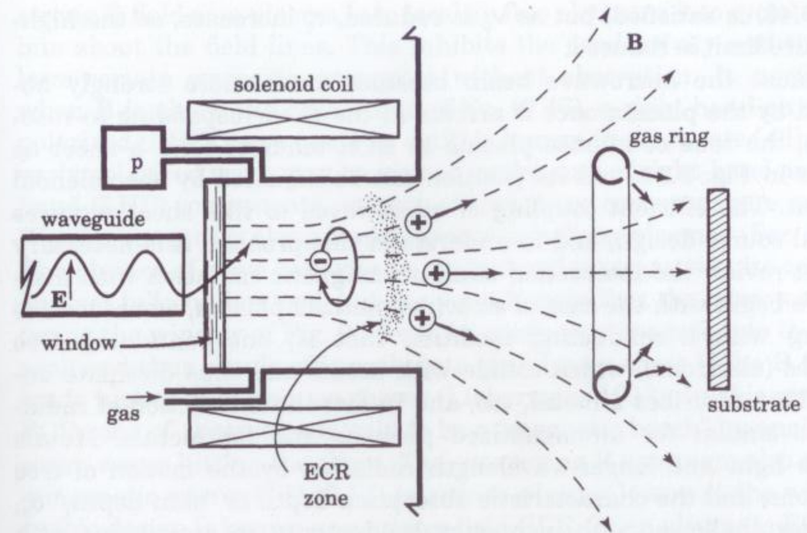

Figure 9.24 Mirror-field ECR plasma source driven by a waveguide and configured for downstream film deposition.

plane perpendicular to **B** as shown and with a cyclotron radius, r_c, given by Eq. (8.17). If the microwave angular frequency, ω_o, is the same as the angular frequency of the orbit, $v_\perp/r_c$, then the electron will be in phase with the field at both $+\mathbf{E}_o$ and $-\mathbf{E}_o$. This phenomenon is known as **electron cyclotron resonance** (ECR), and from Eq. (8.17) it can be seen to occur when

$$|\mathbf{B}| = \omega_o m_e/q_e = 2\pi\nu_o m_e/q_e = 3.58\times10^{-11}\nu_o \tag{9.46}$$

or when $|\mathbf{B}| = 0.0875$ T (875 Gauss) for $\nu_o = 2.45$ GHz. (Due to other plasma interactions, the resonance point can be shifted somewhat from this prediction.) At pressures low enough so that many orbits occur between collisions, the electrons continue to gain energy and spiral outward with increasing r_c until they finally collide with a gas molecule or with the side wall. To sustain any plasma, it is only necessary to have enough ionizing collisions to balance the electron loss that occurs by diffusion out of the plasma. Here, the loss is mostly at the end faces ($\perp$ **B**), since lateral diffusion is inhibited by **B**. Consequently, the low-pressure limit is only 10^{-2} to 10^{-3} Pa. At the other extreme, when pressure is high enough that there are many electron collisions per orbit, the resonance is lost (Exercise 9.12) and **B** has little effect. In other words, at high pressure, the electrons are no longer "magnetized," and the plasma behaves more like a conventional microwave discharge. In principle, ECR can be operated at any ν_o as long as

Eq. (9.46) is satisfied; but as v_o is reduced, r_c increases, so the high-pressure limit is reduced.

Because the microwave beam becomes much more strongly absorbed by the plasma once it arrives at the **B** corresponding to resonance, the zone of intense plasma in ECR tends to form a sheet as shown in Fig. 9.24, and its position can be adjusted by the solenoid current. The efficient coupling of microwaves to this sheet requires careful source design, and to understand this problem it is necessary to first review the interaction of electromagnetic radiation with matter. We begin with the case of an *un*magnetized plasma, where we are dealing with a conducting medium: that is, one containing free charges (electrons), which collide with atoms and thus dissipate energy. This describes a metal, too, and in fact the interaction of radiation is similar for unmagnetized plasmas and for metals. Metals absorb light and longer-wavelength radiation by the motion of free electrons, and the characteristic absorption depth or "skin depth," δ_s, becomes shallower with increasing conductivity in accordance with Eq. (9.43). The shallower that δ_s becomes, the larger is the fraction of radiation that gets reflected before it can be absorbed, which is why Ag makes the best mirrors. However, metals also have a plasma frequency, ω_p, which is given by Eq. (9.15). If the radiation angular frequency, ω_o, exceeds ω_p, then the electrons respond much less to the **E** oscillations of the radiation, and the medium becomes much more transparent. Thus, alkali metals become transparent in the UV, and plasmas become transparent when their density, n_e, is low enough that $\omega_p < \omega_o$, although there will still be some absorption due to electron collisions with molecules. For a $\omega_o/2\pi$ ($=v_o$) of 2.45 GHz, we can see from Eq. (9.15) that transparency occurs below $n_e = 7.45\times10^{10}$ cm^{-3}. Plasmas are designated "underdense" and "overdense" when n_e is below or above this point.

ECR plasmas are usually run overdense so as to achieve the desired level of gas activation for film deposition. However, the presence of a strong enough **B** field between the window and the ECR zone allows microwaves to propagate across this distance without being absorbed within the skin depth. This is because a highly magnetized plasma behaves like a *dielectric* medium rather than like a metal. Recall that the electrons in a dielectric are localized about individual atoms and experience a restoring force when displaced (polarized). An electromagnetic wave induces local oscillation in this polarization, but no conduction and therefore no energy dissipation except at high amplitude (nonlinear effects). The atomic oscillators essentially re-radiate the wave, and it is not absorbed. The wave is just slowed down or "loaded" by the oscillator interaction, and the wavelength is shortened, as expressed in the index of refraction [Eq. (4.40)]. The effect of a strong **B** field on a plasma is to localize free electrons into cyclotron orbits about the field lines. This inhibits the conductivity and thus allows certain waves to propagate without absorption. In particular, when **B** is above the ECR value of Eq. (9.46), a right-hand circularly polarized (RHP) wave (see Fig. 4.19) is known to propagate [48]. A linearly polarized wave may be viewed as the sum of right-hand and left-hand (LHP) components, so part of that wave can propagate as well. Wave propagation along **B** also occurs in helicon plasmas (Sec. 9.5.2). The physics of wave behavior in magnetized plasmas is quite complex and not fully understood, but the point here is that the microwave entering the window of Fig. 9.24 can be made to propagate into the ECR zone and thus couple efficiently into the plasma there if the **B** field is made higher upstream as shown (Lieberman, 1993). In this case, the ECR zone of absorption is said to be a "magnetic beach" by analogy to ocean waves hitting the shore. The converging **B** upstream also acts as a magnetic mirror (Fig. 9.12) to reduce plasma losses at the window, so this design is known as a mirror-field ECR. In an alternate ECR design where **B** is lower outside of the ECR zone, the wave is made to penetrate sufficiently into the ECR zone despite the skin-depth absorption by using a resonant cavity to achieve very high **E** [49].

The behavior of an ECR plasma changes dramatically in crossing from the underdense to the overdense region, which is done by increasing the microwave power or the gas pressure [50]. Microwave absorption and plasma density increase abruptly, and the plasma moves outward radially within the ECR zone. This and other mode shifts and nonuniformities can be a problem for process control, so it is important to characterize the behavior of an ECR source and to establish stable and reproducible operating conditions before running a process.

Typical plasma density in an ECR source is 10^{12} cm^{-3}, much higher than the 10^{10} cm^{-3} of the parallel-plate glow discharge. Toward the low end of the operating pressure range, this density becomes comparable to the gas concentration itself, which is 2.4×10^{12} cm^{-3} at 10^{-2} Pa and room T and still lower at the elevated gas T present in such an intense discharge. Thus, the **ionization fraction** can approach *unity* in ECR and other high-density, low-pressure plasma sources, whereas in the parallel-plate plasma it is more like 10^{-6}. This difference fundamentally changes the chemistry of plasma-enhanced film-deposition processes. Instead of a process dominated by neutral radicals as the depositing species and supplemented by ion bombardment, we have one in which ions carry both a depositing species and bombardment energy. One effect of this change is that the deposition flux is now directed, which is useful for filling the deep via holes encountered in integrated-circuit fabrication while avoiding pileup of deposit on the

sidewalls and resultant cavity formation, as shown in Fig. 9.25*a* and *b*. Another effect is that nearly every depositing atom carries at least several eV of kinetic energy, thus making the most of the beneficial effects of energetic deposition on film properties. However, the effects of this added energetic flux on film properties as compared to films deposited with energetic flux from conventional plasmas have not yet been adequately evaluated.

Two other effects result from high-power, low-pressure operation. One effect is **depleted gas pressure** in the source relative to that measured downstream, even if the gas is fed through the source as shown in Fig. 9.24. This happens when ionization fraction is high, because ambipolar diffusion of ions out of the source [Eq. (9.17)] is much faster than thermal diffusion of neutral particles. Thus, for accurate characterization of source behavior, pressure should be sampled within the source as shown. Note that a thermal-transpiration correction must then be applied [Eq. (3.18)] because of the high gas T. The second effect is **thermal runaway** of electron temperature, $\tilde{T}_e$. Without enough gas collisions, the $\tilde{T}_e$ of ECR electrons would continue to increase until it was so large that the orbit radius would approach the source radius. Thus, when source-pressure depletion sets in at high power, $\tilde{T}_e$ and ionization fraction rise, causing still more depletion. This is a positive-feedback, unstable situation. Further instability arises when $\tilde{T}_e$ exceeds 100 eV or so, because then ionization cross section begins to decrease with increasing $\tilde{T}_e$ (Fig. 8.2), and thus less electron energy is lost to collisions for a given pressure (Lieberman, 1993). High $\tilde{T}_e$ defeats one purpose of electrodeless excitation, namely elimination of the high-voltage sheath, because sheath voltage increases with $\tilde{T}_e$, as discussed prior to Eq. (9.18). Thus, in ECR sources run at too low a pressure, undesirable sputtering occurs where the ECR zone intersects the sidewall. Too high a $\tilde{T}_e$ can also result in ex-

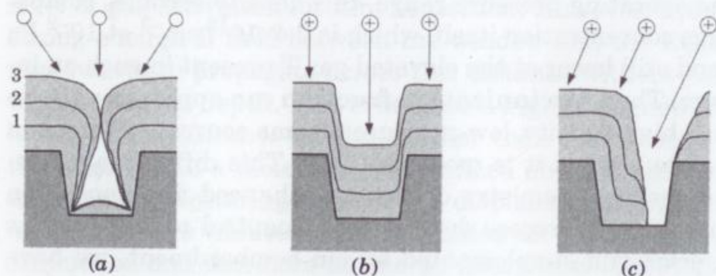

Figure 9.25 Characteristic film-thickness profiles at three successive times (1, 2, 3) during deposition into a via or trench on the substrate, when the depositing species are (*a*) randomly directed neutrals, (*b*) perpendicularly directed ions, and (*c*) obliquely directed ions.

cessive ion-bombardment energy at the film because of electron acceleration in the diverging **B**, as we will see below.

The diverging **B** field downstream of the solenoid of Fig. 9.24 is a reverse magnetic mirror: it is a **"magnetic nozzle,"** which accelerates orbiting electrons in the diverging direction as discussed prior to Eq. (9.27) (Cecchi, 1990). In the limit as $\mathbf{B} \to 0$ downstream, all of the orbiting (thermal) kinetic energy of the electron can be converted to kinetic energy directed along **B**. Moreover, ions are accelerated along **B** together with the electrons by the ambipolar-diffusion effect (Sec. 9.2), even though **B** is not strong enough to magnetize the ions. Thus, the higher the $\tilde{T}_e$, the higher the ion-bombardment energy on a downstream substrate. Ion acceleration along the **B** lines shown in Fig. 9.24 also causes ions to impinge at an oblique angle, which destroys the advantage of directed deposition for via filling, as shown in Fig. 9.25*c*. The ion flux can be collimated and the electron acceleration reduced at the same time by adding a downstream solenoid coil to straighten out the field lines [51] as shown in Fig. 9.26*a*.

If *higher* ion bombardment energy is desired than is supplied by the magnetic nozzle, negative bias can be applied to the substrate. When the substrate or film is a dielectric, this needs to be **rf bias** (Fig. 9.19). The application of bias also provides a convenient method of measuring ion current to the substrate, by assuming that the bias power applied is the product of the bias voltage times the ion current [Eq. (9.40)]. This assumption is valid at low pressure and at high power density in the source plasma, in which case most of the applied bias power goes into ion acceleration across the cathode sheath. The power input to the substrate from the high ion-bombardment flux can heat it significantly, even when bias is not applied. Recall from Sec. 5.8 that thermal contact between a substrate and its platform at low pressure is poor even if clamping is employed. Since platform T is almost always measured instead of actual substrate T, much of the work in which "room-T" deposition of high-quality films is reported actually involved a much higher substrate T. It may be that high-density plasma allows deposition at lower substrate T, but one has to be very careful in determining this T. These same considerations regarding substrate biasing and heating also apply to other high-density sources to be discussed below.

Plasma confinement downstream of a high-density plasma, or wall-loss reduction around any plasma, can also be achieved using a **"magnetic bucket."** One common configuration is shown in Fig. 9.26*b*. The array of permanent magnets surrounding the chamber presents to approaching electrons **B** fields that are crosswise between the magnets and thus deflect the electrons, and that are converging at each magnet and thus act as magnetic mirrors. Electrons can escape through the

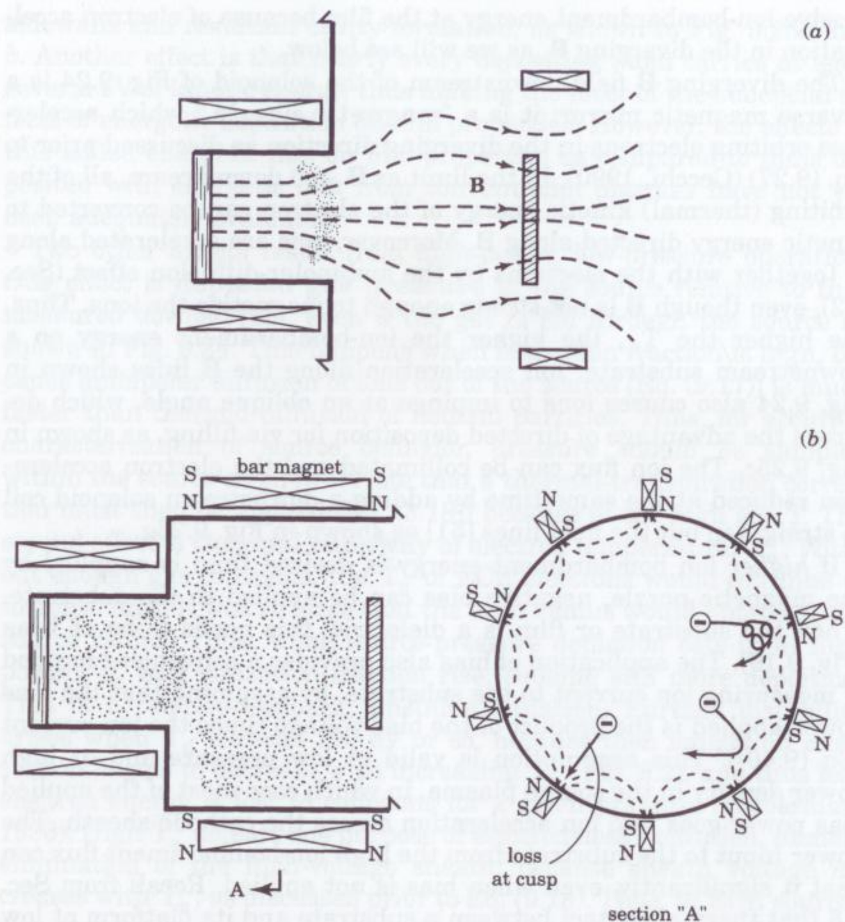

Figure 9.26 Methods of magnetically confining plasma downstream of a high-intensity plasma source such as that of Fig. 9.24: (*a*) solenoid field shaping and (*b*) magnetic bucket.

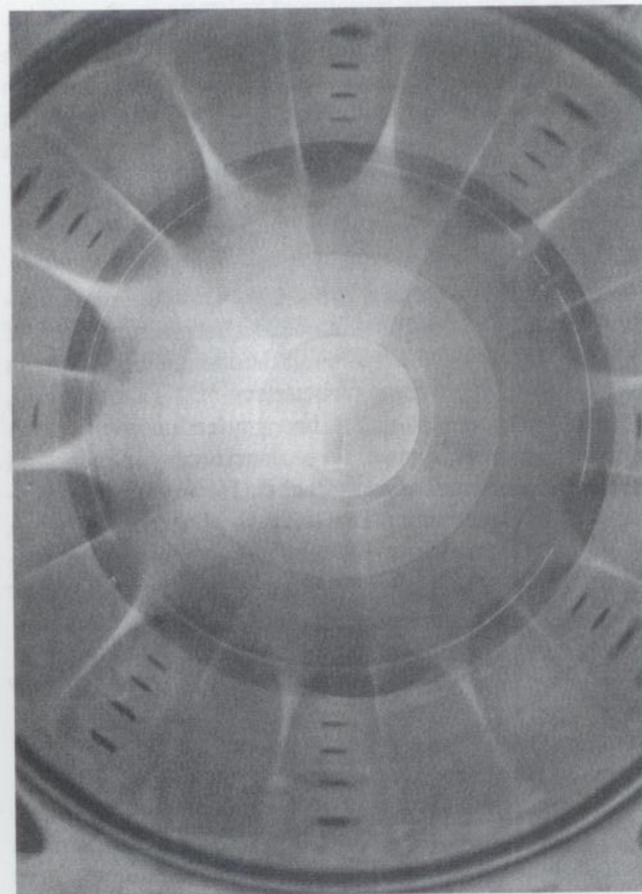

Figure 9.27 Photograph of plasma confined by a magnetic bucket, viewed as in Section A of Fig. 9.26*b*. (Source: Reprinted from Ref. 52 by permission.)

mirror only if they have velocities nearly parallel to and aligned with the "cusps" in **B** parallel to the chamber radius at the center of each magnet [Eq. (9.27)]. Figure 9.27 is a photograph of a plasma being confined by a magnetic bucket, looking from downstream. Bright plasma extends outward toward the wall at the ten cusp points. The magnet spacing in a bucket is always a compromise between too much loss at the cusps if the spacing is too small and too much **B** penetration toward the center of the chamber if the spacing is too large.

Gas distribution is the final aspect of ECR design for film deposition to be discussed. We have mentioned injection of gas upstream in the ECR source, but if one were to introduce a *depositing* species there, most of the film deposition would occur within the source rather than on the downstream substrate. Therefore, the depositing species is instead injected just upstream of the substrate, through the "gas ring" shown in Fig. 9.24. The ECR plasma supplies the gaseous species which either activates or reacts with the depositing species to form the film. For example, SiH_4 from the gas ring and activated O_2 from the plasma will deposit SiO_2, and SiH_4 plus activated He will deposit amorphous Si. The chemistry of film deposition downstream of a plasma is discussed further in Sec. 9.6.3. The gas ring contains an array of effusion orifices directed at the substrate. These need to be positioned so that the flux of gas arriving at the substrate is reasonably

uniform. They also need to be small enough, compared to the inside diameter of the ring tubing, that the fractional pressure drop through the ring tubing is small, to ensure uniform effusion rate from orifice to orifice. The pressure drop due to fluid flow in tubing can be found from Eqs. (3.2) and (3.7), and flow rate versus pressure drop for orifices in the sonic-flow limit is given in Appendix E.

9.5.2 Helicons

Electromagnetic waves of *rf* frequency can propagate through an overdense plasma when it is magnetized, just as could the microwaves of the ECR plasma of Fig. 9.24. Recall from that discussion that a plasma is overdense when its plasma frequency, ω_p [Eq. (9.15)], exceeds the angular drive frequency, ω_o, of the applied power. In an overdense plasma without magnetization, free electrons can respond to the electromagnetic field to absorb and reflect it. However, magnetization of the electrons inhibits their conductivity so that the plasma behaves more like a dielectric medium. In particular, when the magnetic field, **B**, is strong enough so that the electron cyclotron angular frequency,

$$\omega_c = (q_e/m_e)|\mathbf{B}| \tag{9.47}$$

[compare Eq. (9.46)], is larger that the drive frequency, ω_o, right-hand circularly polarized waves (see Fig. 4.19) can propagate along **B** [48]. These are the "whistler" waves discovered in the early days of radio, which are generated in lightning storms and then propagate through the ionospheric plasma along the Earth's magnetic field. They are more generally known as "helicon" waves because of the helical path traced by the tip of the rotating **E** vector as it propagates.

Interaction with the orbiting electrons of a magnetized plasma slows down a helicon wave just as interaction with the oscillating dipoles in a dielectric medium slows down a light wave. Thus, the wave speed in either medium is

$$c = \frac{c_o}{\tilde{n}} = \nu_o \lambda = \nu_o\left(\frac{\lambda_o}{\tilde{n}}\right) = \frac{\omega_o}{2\pi/\lambda} = \frac{\omega_o}{\mathbf{k}} \tag{9.48}$$

where Eq. (9.45) provides the second equality, and where

c_o = speed of light in vacuum or air = 3×10^8 m/s
$\tilde{n}$ = index of refraction of the medium at ω_o
λ = wavelength in the medium
λ_o = wavelength in vacuum or air
ν_o = frequency of the wave, Hz
ω_o = angular frequency of the wave = $2\pi\nu_o$, s^{-1}
$\mathbf{k}$ = wave vector or propagation vector = $2\pi/\lambda$ [see text following Eq. (4.44)]

For plane waves, c is also the "phase velocity," which is the speed at which a point of given phase advances in the direction of propagation. Now, $\tilde{n}$ increases with ω_o, especially as one approaches the resonant frequency of the medium and the interaction becomes very strong. This accounts for the *dispersion* of white light into its constituent colors by a prism. Dispersion relationships can be derived from Maxwell's equations for any electromagnetic situation, and for a right-hand circularly polarized wave propagating parallel to **B** in a plasma, it is found [48] that

$$\tilde{n}^2 = 1 - \frac{\omega_p^2}{\omega_o^2 - \omega_o\omega_c} \approx \frac{\omega_p^2}{\omega_o\omega_c} \tag{9.49}$$

The last equality holds for the present case of interest, which is when $\omega_o \ll \omega_c \ll \omega_p$ (drive, cyclotron, and plasma frequencies, respectively). That is, our plasma is strongly magnetized for the drive frequency being applied, and it is dense enough that the plasma frequency is very high. Note that in the more general form of Eq. (9.49), when $\omega_o \to \omega_c$, $\tilde{n} \to \infty$, so the wave is stopped dead in its tracks. This is the *resonant* situation of the ECR plasma [Eq. (9.46)]. However, we return now to the situation at lower ω_o.

By inserting into the approximation at the end of Eq. (9.49) the expressions for ω_p [Eq. (9.15)] and ω_c [Eq. (9.47)], we obtain (in SI units)

$$\tilde{n}^2 = n_e q_e/\varepsilon_o \mathbf{B}\omega_o \tag{9.50}$$

Then, using Eq. (9.48) to eliminate $\tilde{n}$, we have for the wavelength of the helicon wave in the plasma,

$$\lambda = \sqrt{\frac{2\pi\varepsilon_o c_o^2}{q_e}}\sqrt{\frac{\mathbf{B}}{n_e\nu_o}} = 5.59\times10^{12}\sqrt{\frac{\mathbf{B}}{n_e\nu_o}} \tag{9.51}$$

Taking typical conditions of ν_o = 13.56 MHz, **B** = 0.01 T (100 Gauss), and $n_e = 10^{18}/m^3$ ($10^{12}/cm^3$), we find that $\tilde{n}$ = 147 and λ = 15 cm. The very high $\tilde{n}$ produces a very *slow wave* whose resulting short λ means that 13.56-MHz power can now be coupled conveniently into the plasma wave from an *antenna* rather than through the electrodes discussed in Sec. 9.4. This arrangement is shown in Fig. 9.28. The entire

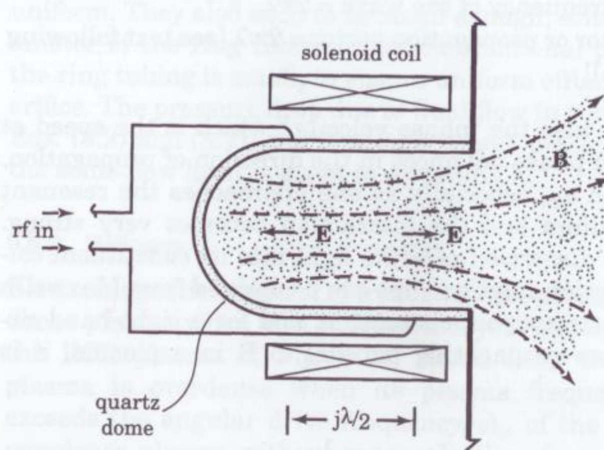

Figure 9.28 Helicon plasma source. The external antenna loop (not shown) is structured so as to drive the helicon wave to the right along **B**.

plasma container needs to be a dielectric here, not just the end window as in ECR, so a glass or quartz dome is usually used. The antenna loop (not shown) is wrapped around the dome and is driven through a matching network such as the one shown in Fig. 9.21. As in the case of ECR, the plasma electrons are accelerated out of the source by the magnetic nozzle effect of the diverging solenoid **B** field, and the ions follow by ambipolar diffusion. The magnetic confinement techniques of Fig. 9.26 can be used downstream. Since **B** is about 10 times smaller than in ECR, however, the solenoid requirements are much less severe.

Helicon behavior is strongly affected by the power level applied. At low power, the voltage on the antenna can be over 1 kV and can therefore act as an electrode to couple power capacitively through the quartz wall into the plasma sheath, as with the parallel-plate plasma of Sec. 9.4.2. As power is increased, there is a discontinuity [53] at which the helicon-wave coupling mode activates and becomes dominant, with an accompanying decrease in antenna voltage and a ×30 increase in plasma density, n_e. However, the antenna voltage may still be high enough to cause local capacitive coupling with accompanying high-energy ion bombardment and sputtering of the quartz dome. As power continues to increase in the helicon mode, there are further smaller discontinuities in n_e. These probably correspond to jumps in the number, j, of half wavelengths that best match the antenna length [53] [see Fig. 9.28 and Eq. (9.51)]. For stable process operation, one should adjust power or **B** to a point midway between these jumps.

The mechanism of plasma electron energy gain in the helicon is different from that in either the rf parallel-plate or the ECR plasma, and it is believed to be "Landau damping," which operates as follows. In the regions of time and space where the **E** field of the helicon wave points partly upstream (to the left in Fig. 9.28), plasma electrons are accelerated downstream. When an electron's velocity downstream is close to the wave's phase velocity, c [Eq. (9.46)], it can "surf" on the wave and receive considerable energy from it, damping (attenuating) the wave as it does so. In the example after Eq. (9.51) where $\tilde{n} = 147$, we have $c = 2{\times}10^6$ m/s. From Eq. (8.6), we find that this corresponds to 12 eV of electron energy, which is in the range of typical ionization potentials (Fig. 8.3) and thus provides efficient coupling from the wave to plasma ionization. This mechanism of electron energy gain does not require collisions with molecules to operate, in contrast to the sheath-edge mechanism of the high-frequency parallel-plate plasma (Fig. 9.18) and the phase-shift mechanism of the unmagnetized microwave plasma (Fig. 9.22). Collisionless electron energy gain also occurs in the ECR plasma of the last section. In addition, confinement of the electrons by **B** in both of these plasmas greatly increases their path length before they are lost to the walls. Collisionless coupling and magnetic confinement together allow these plasmas to be operated down to very low pressures of 10^{-2} Pa or so where the molecular mean free path exceeds the plasma diameter.

9.5.3 Inductive coils

The third and last method of electrodeless plasma excitation to be discussed is inductive coupling [54], which has the simplest concept and equipment. If a highly conductive helical coil of j turns is wrapped around a dielectric containment tube or dome as shown in Fig. 9.29 and operated in resonance with applied rf power, the very large rf current circulating in the coil, I_{rf}, generates an axial rf magnetic field, $\mathbf{B}_{rf}$, within the tube, which in turn induces a circulating rf electron current in the plasma, jI_{rf}, once the plasma is lit. This is basically a transformer, with the plasma itself acting as the single secondary winding. Since the electrons are confined to orbits by $\mathbf{B}_{rf}$, this plasma can operate down to 10^{-1} Pa or so, although some collisions are required for electron phase shifting between rf cycles, as in the microwave plasma of Fig. 9.22. Since high-voltage sheaths are not involved, power coupling to the electrons is efficient and power density can be high, so plasma densities of $\sim 10^{12}$ cm^{-3} are achievable. The inductive plasma can also operate at 1 atm as a "plasma torch," which has been explored for deposition of diamond films from methane but will not be discussed further here.

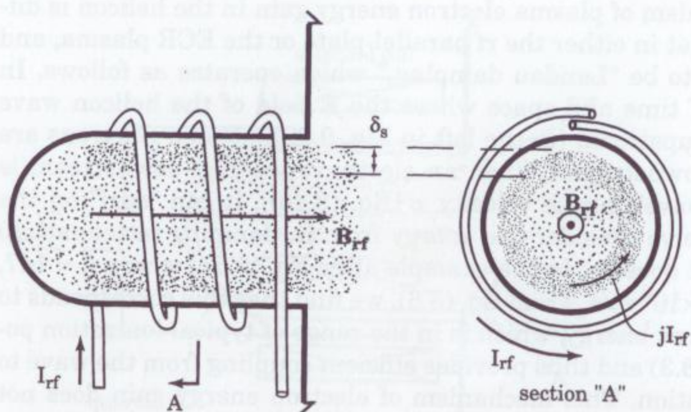

Figure 9.29 Inductive coupling to a plasma from a helical coil. [δ_s is the skin depth of Eq. (9.43).]

Coil resonance can be established using the coil's inductance in conjunction with a capacitor in an L-C circuit similar to that of the Fig. 9.21 matching network. However, the helical-resonator coil of Fig. 9.30 achieves a sharper and stronger resonance (referred to as a higher "Q") and therefore a higher current. This type of coil [55] is grounded on one end and floating on the other, and is (1/4)λ from end to end along the helix, so that it resonates like an antenna. The length required is found from Eq. (9.45) and is 5.5 m at 13.56 MHz. The grounded enclosure provides some parallel capacitance, and imped-

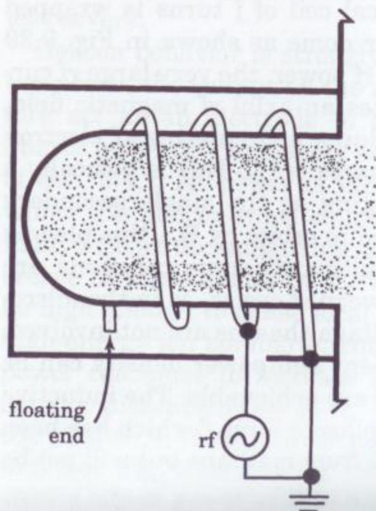

Figure 9.30 Geometry of a helical resonator.

ance matching to the power supply is accomplished with a supplemental parallel capacitor and by the position of the rf input on the coil. In either of the above resonators, the voltage from end to end of the coil is many kV, so *capacitive* coupling to the plasma through the dielectric wall is also possible, as with the helicon antenna. This is generally undesirable because of the accompanying high-voltage sheath and consequent sputtering and elevation of the plasma potential above ground. However, the capacitive mode can be blocked effectively by inserting a cylindrical metal electrostatic shield between the coil and the dielectric wall. The shield needs to have periodic slots oriented parallel to the cylinder axis to prevent circulating currents from developing and robbing power from the plasma. This shield cannot be used with the helicon, because its antenna couples through the *electric* field.

The plasma of Fig. 9.29 is most intense in the annular region where the current is circulating, since this is where the electrons are being accelerated to ionization potential. This region extends in from the wall by about the skin depth, δ_s, of Eq. (9.43). For a given applied frequency, ν_o, δ_s depends on the plasma conductivity, s. We can use Eq. (9.13) to find s so long as the pressure is high enough that the electron collision frequency, ν_e, is much larger than $2\pi\nu_o$ (= ω_o). Into Eq. (9.9) for ν_e, we insert the following:

- the speed of a 4.5 eV ($\tilde{T}_e$ = 3 eV) electron, 1.3×10^6 m/s from Eq. (8.7)
- a typical collision cross section of 10^{-19} m^2 (0.1 nm^2)
- the concentration of a room-T gas at 10 Pa

For this case, we find $\nu_e = 3\times10^8$ s^{-1}, which is sufficiently larger than the ω_o of 9×10^7 s^{-1} at 13.56 MHz. Under these conditions, and for a plasma density of 10^{18} m^{-3} (10^{12} cm^{-3}), we find δ_s = 1.4 cm. Note that δ_s decreases with increasing s and therefore with increasing power (or n_e) and decreasing pressure. For the most efficient and uniform power coupling into the plasma volume, one wants δ_s to be about the same as the radius of the containment cylinder. If δ_s is larger, the impedance of the "secondary winding" represented by the plasma becomes too high, and inductive coupling dies out. If δ_s is smaller, the intense region of the plasma becomes more concentrated toward the cylinder periphery. However, the center region still "fills in" with plasma to some extent by diffusion.

As in the cases of ECR and the helicon, the inductive plasma diffuses out the end of the source and can be used downstream in conjunction with a gas ring for film deposition, as shown in Fig. 9.24 for ECR. All three sources share the ability to achieve high plasma density of >10^{12} cm^{-3} at low pressures without developing high sheath voltages. This combination gives ionization fractions near unity and

high fluxes of low-energy, directed ions that are particularly well suited to reaction activation and structural modification at the surface of a depositing film. The main difference with inductive coupling is that there is no solenoid **B** field with its accompanying problems of ion steering and acceleration along the diverging field lines. Although inductive coupling is an old concept, large, high-intensity inductive sources have become commercially available only recently, so they have been explored very little for film deposition.

A few other inductive configurations deserve mention. One is the *immersed* coil of Fig. 9.14, which was used there to enhance the ionization of sputtered particles. Another is the spiral coil of Fig. 9.31, which has the potential advantages of generating a reasonably uniform plasma over a large diameter and of coupling it closely to the depositing film. An electrostatic shield with radial slots can be used here to block capacitive coupling as in the case of the helical coil. Finally, Fig. 9.32 shows a ferrite-core transformer driven at frequencies as low as 60 Hz, with a plasma loop acting as the secondary winding [54]. This is probably not scalable to large areas, but it could provide an efficient and inexpensive source of free radicals and ions for use in downstream reactions on small substrates, as did the microwave cavity of Fig. 9.22.

9.6 Plasma Chemistry

This chapter has thus far focused on the *physics* of the glow-discharge plasma; that is, the generation of charged particles and the electric fields and currents which these charges produce. The principal features observed are the presence of energetic electrons (T_e of several eV) throughout the bulk of the plasma, and the bombardment of all

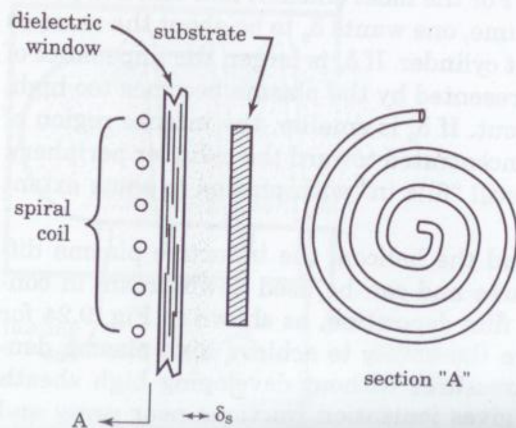

Figure 9.31 Inductive coupling from a spiral coil.

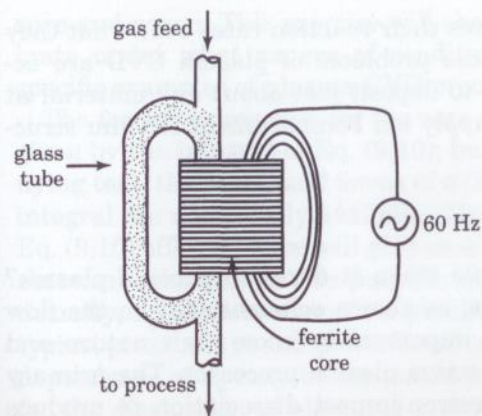

Figure 9.32 Transformer coupling to a plasma loop.

surrounding surfaces by energetic ions (10 to 1000 eV). Chapter 8 dealt with the physical effects of this ion bombardment on sputtering targets and depositing films. We now turn to the *chemistry* which is induced by interaction of charged particles with gaseous and adsorbed reactants.

Recall from Sec. 6.5.4 that most elements can be gasified by reacting them with terminating radicals: for example, Si becomes SiH_4 (silane) gas, and Al becomes $Al(CH_3)_3$ (trimethyl Al) vapor. This allows film-forming elements to be transported by fluid flow to the reaction zone on or above the substrate, where the terminating radicals are eliminated and the remaining elements combine with each other to deposit the film. In *thermal* CVD, the energy needed to surmount the reaction-activation-energy barrier (Fig. 7.16) comes from the elevated substrate T. In *plasma* CVD, it comes from the charged particles. We have established the concept of plasma activation of chemical reactions at low T in previous discussion at the beginning of this chapter and Chap. 8. Below, we will examine in more detail how this occurs and how it can be controlled.

As in the case of thermal CVD, the plasma-deposition process consists of a series of steps, any one of which may be the rate-controlling one, and there are likely to be parallel pathways as well. Usually, the chemical kinetics are not known well enough that we may be certain of the dominant reaction pathway through this web. The plasma case can be even more complex than the thermal one, because charged particles tend to be less selective than thermal energy in activating reactions. This makes reaction modeling a major challenge, and it also can increase film contamination. For example, unwanted decomposition of the methyl radical in $Al(CH_3)_3$ leads to several percent of C incorporation in Al film, although this can be controlled by using a minimum of plasma power [56]. Background gases such as CO and H_2O also be-

come activated, and this increases their reaction rates over what they would be in thermal CVD. These problems of plasma CVD are accepted in return for the ability to deposit just about any material at low T and to simultaneously supply ion bombardment for film structural improvement.

9.6.1 Kinetics

What happens to a gas molecule when it dares to enter a plasma? There are various possible fates, as shown schematically in the flow diagram of Fig. 9.33, and it is important to know their nature and rates to design and optimize reactive plasma processes. The primary chemical-activation event is electron-impact dissociation to produce free radicals, as shown at (*a*). Ionization also occurs, of course, but at a much lower rate because of the higher energy required, except in very intense low-pressure plasmas. The free radicals may diffuse directly to the substrate surface (*b*), or they may first react with other radicals or molecules (*c*) to produce gaseous precursor molecules which then diffuse to the surface (*d*). Some of the source gas reaches the surface without activation (*e*), and some is pumped away directly (*f*). The species arriving at the surface have a certain adsorption probability that depends on conditions there, and the adsorbate then reacts (*g*) to form the film and volatile by-products. The surface reactions may be activated by electron and ion bombardment and by the substrate T. Reactive plasma processes other than plasma CVD involve a solid source material as well as a gaseous one, those processes being reactive sputtering, activated reactive evaporation, laser ablation, and arc evaporation. In those cases, the vaporized solid will be adsorbing and reacting too. Here, however, we concentrate on plasma CVD, since it involves the richest gas-phase chemistry, so that the other processes are subsets of plasma CVD in that regard. We proceed below to make rough estimates of the rates of the various gas-phase steps shown in Fig. 9.33 and their dependence on the primary plasma parameters of pressure and power. This exercise will show which steps are going to dominate under what ranges of conditions. In Sec. 9.6.4, we will give specific examples of plasma-CVD processes.

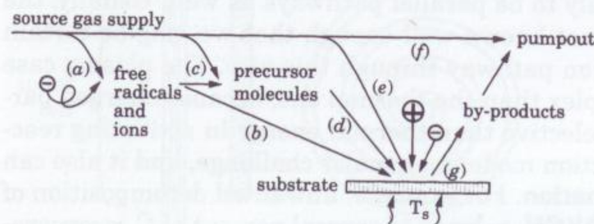

Figure 9.33 Plasma-CVD reaction steps as defined in the text.

The formal expression for the rate of an electron-impact reaction is given by the integral of Eq. (9.10); but as pointed out in the accompanying text, the functional forms of $\sigma(E_e)$ and $f(E_e)$ needed to solve this integral are not usually available. Nevertheless, the simplifications to Eq. (9.10) offered below will give us a good *qualitative* sense of plasma chemical behavior. In this pursuit, we first need to know the **plasma density,** n_e. Measurements on parallel-plate plasmas indicate that at typical pressure (p) and power density, $n_e \sim 10^{10}$ cm^{-3}. The p and power dependence of n_e may be estimated by writing the following equation for the dissipation of electrical input power, P (in W), in the plasma (Lieberman, 1993):

$$P = j_+ A\varepsilon_L = 0.6 n_{eo} q_e u_a A \varepsilon_L \approx n_e q_e u_a A \varepsilon_L \tag{9.52}$$

where A is the effective area of plasma contact with its container, and the second equality is given by Eq. (9.20) for the ion flux, j_+, injected into the sheath. In the last equality, we are neglecting gradients in n_e across the bulk of the plasma. The term ε_L (in eV, ≡ V) is the total energy dissipated in the plasma per ion injected into the sheath, and it consists of three terms:

$$\varepsilon_L = \varepsilon_c + 2\tilde{T}_e + \varepsilon_i \tag{9.53}$$

which are, respectively, the total electron energy lost in collisions in the plasma per ion-electron pair created by ionization, the mean energy of an electron escaping the sheath for a Maxwellian electron-energy distribution, and the ion energy gained in crossing the sheath. $\tilde{T}_e$ decreases slowly with increasing p, but it is largely "pinned" to a few eV by the thresholds for the inelastic collisions with gas molecules (dissociation and ionization), except at <1 Pa in ECR plasmas, where "thermal runaway" can occur due to insufficient collisions (Sec. 9.5.1). Meanwhile, ε_c increases slowly with increasing p, so ε_L is only a weak function of p. u_a also varies little with p, since it is determined by $\tilde{T}_e$ through Eq. (9.17). Finally, A decreases somewhat with increasing p due to electrons diffusing less far from their generation region. The net effect of these compensating behaviors of the Eq. (9.52) factors is that n_e is a weak (usually increasing) function of p, and we will therefore assume for present purposes that n_e is independent of p. We can also see from Eq. (9.52) that n_e will increase with power. By the way, Eqs. (9.52) and (9.53) also show why the electrodeless plasmas of Sec. 9.5 are more efficient at generating high n_e, because the absence

of a high-voltage sheath makes ε_i lower and thus n_e higher for a given power input.

Given n_e, we now estimate the **dissociation rate**: the generation rate of a typical free radical, B, from molecules of AB. To do this, we first replace the cross section function $\sigma(E_e)$ in Eq. (9.10) with an abrupt dissociation threshold of 9 eV. This threshold is just above the low-energy edge of the total-neutral-dissociation curve for SiH_4 in Fig. 9.2, where the dissociation-collision cross section is $2{\times}10^{-16}$ cm^2. We also need the speed of a 9-eV electron, which is $c_e = \sqrt{2E_e q_e/m_e} = 1.8{\times}10^8$ cm/s. For the electron-energy-distribution term, $f(E_e)$, we assume the Maxwellian form of Fig. 2.4, where we can see by eyeball integration that about 10% of the distribution lies above the c_e corresponding to

$$2\overline{c_e^2}$$

—that is, above twice the mean energy. Thus, for a typical plasma with a mean electron energy of 4.5 eV ($\tilde{T}_e$ = 3 eV), about 10 percent of n_e is energetic enough to dissociate SiH_4 or some other typical reactant molecule. Putting this all together in Eq. (9.10), we have for a dissociation rate of AB per unit volume,

$$R\ (\text{mc/cm}^3{\cdot}\text{s}) = n_e n_{AB} c_e \sigma \cdot 10\% = 3.6{\times}10^{-9}\ n_e n_{AB} \qquad (9.54)$$

for n_e and n_{AB} in cm^{-3}. From this, the *frequency* at which an individual molecule of AB becomes dissociated is

$$\nu_d = R/n_{AB} = 3.6{\times}10^{-9}\ n_e = 36\ \text{s}^{-1} \qquad (9.55)$$

where the last equality applies when $n_e = 10^{10}$ cm^{-3}. We are going to compare this frequency with the frequencies of the other events that can befall a molecule entering the plasma, and they are all plotted versus pressure in Fig. 9.34.

For the frequency of the second event—**reaction with a free radical**, we first need an estimate of radical concentration. Since dissociation energy thresholds are lower than ionization thresholds, dissociation rate is much higher than ionization rate. Also, radical diffusion to the wall is much slower than electron diffusion because of the much lower particle speed. Consequently, the steady-state dissociation fraction of molecular plasmas is much higher than the ionization fraction or plasma density, n_e. In the Sec. 9.1 example of N_2, whose triple bond makes it one of the most difficult molecules to dissociate, this fraction was found experimentally to be 0.025 at a moderate power level of 0.3 W per cm^2 of parallel-plate cross section. We

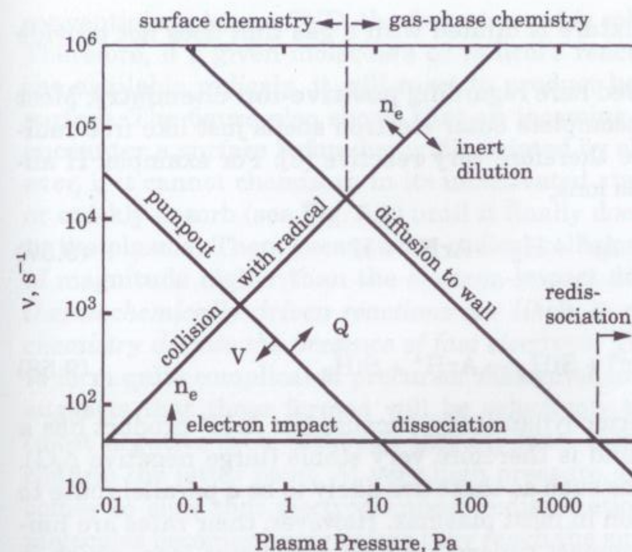

Figure 9.34 Approximate frequencies of various events that can befall a molecule in a glow-discharge plasma, for conditions and assumptions given in the text. (Source: Adapted from a figure in Ref. 72.)

will assume for present purposes a typical value of 0.1n for free-radical concentration, where n is the total gas (molecule) concentration. To the molecule-radical reaction, we can now apply the rate equation for a conventional (thermal) second-order reaction [Eq. (7.34)]. Indeed, free radicals are involved as intermediate species in many thermal chain reactions such as combustion and polymerization. As in the thermal case, the rate constant here is exponential in T per Eq. (7.35) unless the activation energy, E_a, is zero. E_a is in fact always zero in the case of *radical*-radical reactions, because then no bonds need to be broken to activate the reaction—but E_a may be nonzero when one reactant is a complete molecule. In the limit of $E_a = 0$, reaction proceeds at "collision rate" as expressed by Eq. (7.39), where the room-T rate constant is $k_c = 1.6{\times}10^{-10}$ cm^3/mc·s. Thus, for the collision *frequency* and upper-limit reaction frequency of an individual molecule, say CD, with B radicals, we have

$$\nu_r = R/n_{CD} = k_c n_B = 1.6{\times}10^{-10} \cdot 0.1n = 3.8{\times}10^3\ p \qquad (9.56)$$

where the last equality uses n given by the ideal-gas law, Eq. (2.10), with p in Pa. This frequency is also plotted in Fig. 9.34. It will increase with n_e because of increased dissociation fraction, and it will decrease

if the process-gas mixture is diluted with a gas that does not provide reactive radicals.

A comment is needed here regarding **positive-ion chemistry**. Most positive ions have incomplete outer electron shells just like free radicals do, and they are therefore very reactive [8]. For example, H abstraction by noble gas ions,

$$Ar^+ + H_2 \rightarrow ArH^+ + H \quad (9.57)$$

or

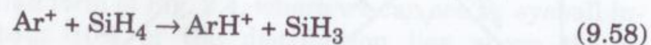

$$Ar^+ + SiH_4 \rightarrow ArH^+ + SiH_3 \quad (9.58)$$

is very favorable thermodynamically, because the ArH^+ product has a filled electron shell and is therefore very stable (large negative $\Delta_f G$). Ion-molecule reactions such as these are likely to be a parallel route to free-radical generation in most plasmas. However, their rates are limited by the electron-impact generation rate of reactive ions, which is much smaller than the electron-impact generation rate of radicals because of the higher electron-energy threshold. Ion-molecule reactions may be more important downstream of the plasma, where the electrons will have dissipated their kinetic energy (more in Sec. 9.6.3).

The remaining two events befalling a molecule entering the plasma are the physical processes of **diffusion to the wall and pumpout**. The frequency at which an individual molecule reaches the wall is the inverse of its characteristic diffusion time, which was estimated in Eq. (9.34) for a typical diffusion length of $\Lambda = 1$ cm. Thus,

$$\nu_D = 1/\tau_D = 4D/\Lambda^2 = 7.7\times10^4/p \quad (9.59)$$

Finally, the pumpout frequency is the inverse of the molecule's residence time in the plasma:

$$\nu_p = W/V = 1.7\times10^3\ Q/Vp \quad (9.60)$$

where W = total volume flow rate of gas, cm^3/s
V = plasma volume, cm^3
Q = mass flow rate, sccm
p = total pressure, Pa

For a typical flow rate of 100 sccm through a 500 cm^3 plasma, we have $\nu_p = 330/p$.

Comparison of these four order-of-magnitude frequency estimates in Fig. 9.34 gives a good qualitative idea of which events will dominate under various plasma operating conditions. In the ~100 Pa regime of conventional plasma CVD, the fastest event is collision with a radical. Therefore, if a given molecule's or radical's reaction rate is fast with the available radicals, it will react to product before diffusing to the surface. The figure also shows that an incoming molecule is likely to encounter a surface before being dissociated by electron impact. However, if it cannot chemisorb in its unactivated state, it will just reflect or quickly desorb (see Fig. 5.1) until it finally does become dissociated in the plasma. Then, because the radical collision frequency is orders of magnitude higher than the electron-impact dissociation frequency, *thermochemically driven reactions are likely to dominate the plasma chemistry despite the presence of fast electrons*. This makes it possible to form quite complicated precursor molecules in plasmas, and it also suggests that those formed will be selectively the most stable ones (most negative $\Delta_f G$), although there is little information available to confirm the latter point. At very high pressure, however, diffusion becomes so slow that electron-impact redissociation of these precursor molecules becomes likely before they reach the surface and deposit, especially at higher power (higher n_e). The high reactivity of the resulting precursor *radicals* may contribute to the gas-phase macroparticle formation (homogeneous nucleation) which is often encountered at high pressure or power in plasma CVD. Macroparticle formation will be discussed further in the next subsection.

Moving down in pressure to <4 Pa in Fig. 9.34, we reach a crossover beyond which a radical, once formed, will diffuse to the surface before colliding with another radical. In this regime, the film-forming reaction sequence involves less gas-phase precursor formation and is instead dominated by radical reactions on the surface. At about the same pressure, depending on n_e and mass flow rate, reactant molecules begin to be pumped away faster than they can become dissociated, so that reactant utilization fraction (η in Fig. 5.1) decreases. This is an example of a shift in the rate-limiting step in a series of steps: reactant dissociation has become limiting here rather than gas supply. However, η can be made high at low pressure by using one of the high-power plasma sources discussed in the previous section. These have an n_e about 100× higher than that assumed for Fig. 9.34, and this raises the dissociation frequency so that it intersects the pumpout frequency at 100× lower a pressure. Figure 9.34 and the procedures used to construct it are useful in determining which of the gas-phase processes is going to dominate a given plasma-CVD process.

We now turn to the **surface chemical processes** by which the film is formed from the adsorbed reactants and precursors (step *g* in Fig. 9.33). Little is known about the surface chemistry of plasma CVD, largely because of the difficulty of analyzing a surface that is im-

mersed in a plasma. Because of the transient nature of many important surface species, analysis really has to be carried out *during* deposition and not after the plasma has been extinguished. New techniques in infrared-absorption spectroscopy and infrared ellipsometry are promising in this pursuit (see Sec. 7.3.3 and Kroesen, 1993). In addressing the surface chemistry, we first note that the sequence of steps which was discussed extensively in the context of thermal CVD in Sec. 7.3.3 also applies to plasma CVD. That is, reactants adsorb, they react to form the film, and by-products desorb. The added factor in the present context is plasma activation of the surface chemistry, which appears both as predissociation of the reactants before they adsorb, and as electron and ion bombardment of the surface. The relative influence of free radicals versus charged particles on film deposition rate and quality can be distinguished by experimentally comparing direct plasma deposition with downstream deposition, since in the latter case the charged particles are selectively attenuated (more in Sec. 9.6.3). *Thermally* activated surface processes may also be occurring, and they can be identified by a change in film properties with increasing substrate T.

One can learn much about the surface processes of both thermal and plasma CVD by examining the profile of films deposited onto structured substrates. A particularly useful structure [57] is shown in Fig. 9.35. This can easily be fabricated by (1) depositing SiO_2 and polycrystalline Si layers onto a Si(100) wafer, (2) defining a trench etch mask by photolithography, (3) etching through the polycrystalline Si, and (4) undercut-etching the SiO_2 in HF solution (which etches Si much more slowly). The trenches should be oriented perpendicular to a (110)

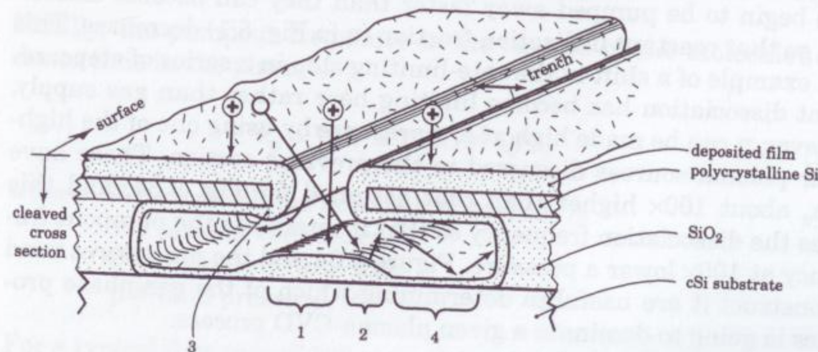

Figure 9.35 Hypothetical thickness profile of a film deposited into the test-structure cavity described in Ref. 57. Deposition in numbered regions is due mainly to (1) ion activation, (2) neutral species of high sticking coefficient, S_c, (3) surface diffusion, and (4) low-S_c species.

cleavage plane, so that after film deposition the substrate can be cleaved to expose the film-thickness profile within the etched cavity. The profile can be viewed and measured by scanning electron microscopy (SEM). Even the profile at incremental depths through the film, as drawn in Fig. 9.25, may be seen by interrupting or modifying the deposition briefly at intervals to produce SEM contrast. The hypothetical film profile shown in Fig. 9.35 illustrates four surface processes that can be distinguished by this technique. Deposition activated by or carried by ion bombardment appears only directly under the trench (region 1), because ions impinge perpendicularly from the plasma, provided that the trench width is much smaller than the plasma-sheath thickness. On the other hand, neutral depositing species impinge over a broad solid angle and therefore also deposit in region 2. Surface diffusion would produce a thickening in region 3 due to surface species diffusing around the trench lip from the top face. If the sticking coefficient, S_c, of a particular depositing species is very low, its deposition will be uniform out to the edge of the cavity in region 4. An intermediate S_c will result in a dropoff in thickness moving outward both on the bottom surface (region 2) and on the underside of the top surface (region 3). The latter effect may be distinguished from surface diffusion by increasing the height of the cavity, which will cause thinning and spreading of an intermediate-S_c profile but will not affect a surface-diffusion profile.

9.6.2 Macroparticles

Plasma-deposition processes are notorious generators of macroparticles, otherwise known as particulates, dust, or powder. For now, we will refer to these simply as particles, although in general, the term "macroparticle" is more precise, because atoms and molecules are particles, too. When plasma-deposition processes are used in dust-free clean rooms for integrated-circuit fabrication or other critical applications, great care must be taken to minimize particle generation and to keep particles from being transported to the substrate or out into the room. Particle transport is minimized by using the vacuum techniques of Sec. 3.4.3. Particle generation occurs in several ways. One involves the flaking off of deposits built up on surfaces surrounding the substrate. This buildup is controlled by periodic system cleaning using plasma etching, wet etching, or abrasion and washing. Particles can also be ejected from various process-material vapor sources such as electron-beam hearths, cathodic arcs, or sputtering targets, and their minimization was discussed in connection with those sources. Remaining generation is due to gas-phase (homogeneous) nucleation of film material, which was discussed as a thermal-CVD problem in

Sec. 7.3.2. There, the remedies were to minimize reactive-gas partial pressure and residence time within the reaction zone, and the same remedies apply to plasma CVD. In plasma CVD, however, homogeneous nucleation and particle growth are both greatly increased by the presence of the plasma, as explained below.

A particle immersed in a plasma behaves like any other electrically floating solid in a plasma in the sense that it develops a negative charge, q, determined by the floating potential, ΔV_f, given by Eq. (9.18). Upon doing so, the particle becomes surrounded by a sheath of positive space charge and thus behaves like a spherical capacitor [58], as shown in Fig. 9.36. The charge required to raise a spherical capacitor to a given potential is proportional to its radius [43], r, so q grows with the particle. Now, the peripheral sheath field surrounding the plasma, which retards electron escape, will far more efficiently retard the escape of these much more massive negative particles, because they have far less translational energy with which to surmount the field barrier. Consequently, massive particles become *trapped* in the plasma and can linger there for minutes or even hours! The longer they linger, the bigger they grow, because vapor atoms and free radicals are continually colliding with them and depositing just as they do on the film surface.

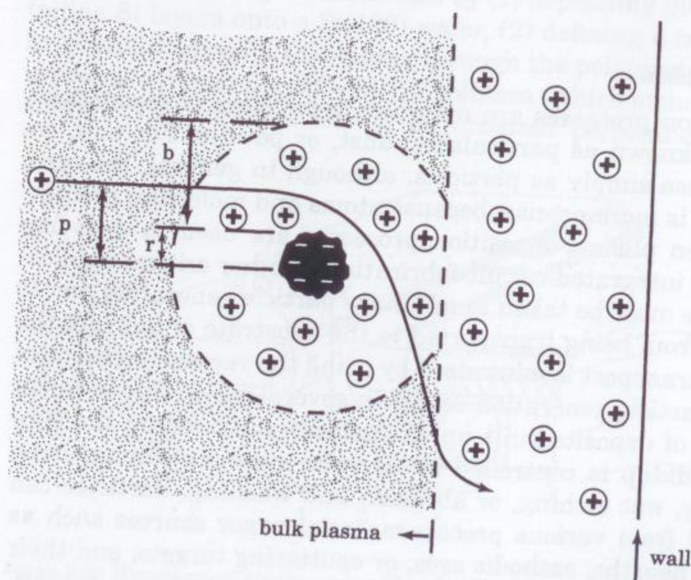

Figure 9.36 Coulombic collision of a plasma ion with a negatively charged macroparticle of radius r which is electrostatically trapped at the edge of the plasma sheath.

In the meantime, numerous other forces are acting on the suspended particles, including the gas flow, gravity, thermophoresis (Sec. 7.4.3), and the "ion wind." One or the other of these can eventually push the particles out of the plasma, sometimes onto the depositing film where they are most unwelcome. Ion wind refers to the flux of ions from the bulk plasma into the peripheral sheath as described by Eq. (9.20), and it interacts with the particles as follows. When one of these ions passes within a particle's sheath, it begins to feel the particle's negative charge, q, and is deflected as shown in Fig. 9.36, thereby transferring momentum to the particle. The smaller the impact parameter, p, the less that q is screened by the particle's sheath, and the larger is the deflection. This is a screened coulombic collision like the ones between ions and solid atoms which were described in Sec. 8.5.2.2, except that here the coulombic interaction is attractive rather than repulsive. The collision cross section may be expressed as $\sigma = \pi p_o^2$, where the characteristic interaction distance, p_o, is proportional to q and therefore to particle radius, r, by the spherical-capacitor relation discussed above. This cross section is much larger than the physical cross section of the particle, since r is much less than the particle's sheath width, b. The drag force produced on the particle by these collisions [59] increases with ion flux and therefore with plasma density, and it increases as r^2, since $\sigma \propto p_o^2 \propto q^2 \propto r^2$ in accordance with the above discussion. This drag force pushes the particle toward the containing wall or depositing-film surface against the electrostatic retarding force of the plasma's peripheral sheath.

The other forces acting on the suspended particles also increase rapidly with particle radius, r: gas-flow drag is proportional to surface area [Eq. (2.28)] and therefore to r^2, thermophoresis is proportional to cross section (r^2), and gravity is proportional to mass (r^3). On the other hand, the electrostatic trapping force is proportional only to the *first* power of r. Thus, the growing particle eventually reaches a critical size at which the trapping is overcome and the particle is pushed out of the plasma. *Which* force overcomes the trapping and whether the particle lands on the depositing film depends on conditions of ion flux [$\propto n_e$ by Eq. (9.20)], gas flow velocity, T gradients, and substrate orientation relative to gravity. In thermal CVD, the charge-related forces are absent, but homogeneously nucleated particles can still be suspended in a layer above a heated substrate by the thermophoretic force acting against gravity and gas flow (Sec. 7.4.3). In plasmas, the behavior of suspended particles and how it depends on process conditions is more complex and is just beginning to be understood.

Suspended particles can be observed easily by the scattering of a laser beam directed into the plasma [60]. They are often, though not always, observed to accumulate at the edge of the sheath as shown in

Fig. 9.36. Indeed, their boundary might be a good marker of the edge of the sheath, not an easy point to measure otherwise. The particles also segregate laterally when there are steps in the surface that are bigger than the sheath width or when a change in surface material changes plasma coupling, presumably because of the lateral field components induced thereby. The particles segregate toward cooler areas due to thermophoresis. They flow laterally along the direction of gas flow and can be swept downstream once they overcome the trapping sheath at the edge of the plasma.

Among the plasma-deposition processes, plasma CVD has the largest potential for particle generation, because of homogeneous nucleation. The nucleation rate is determined by the second-order gas-phase reaction between film precursors. When a third-body collision is required to remove reaction energy and thereby prevent redissociation of the reaction product, the pressure dependence of the reaction rate can even approach third-order [see discussion preceding Eq. (7.38)]. Particle growth therefore increases rapidly with process pressure and plasma density. Indeed, there appears to be a threshold in both of these parameters below which no particles are observed, and in one case it was determined by laser scattering at $\lambda = 532$ nm to be ~10 Pa in pressure for typical parallel-plate plasma densities [61]. Of course, threshold sensitivity depends on the probe, being proportional to laser intensity and to the $1/\lambda^4$ Rayleigh-scattering factor.

Even in a plasma full of particles, these particles will not become incorporated into the film if final film thickness is reached before they have time to grow to the critical size at which they can escape the sheath. When this condition cannot be achieved for a particular process, it is still possible to reduce film contamination by deliberately allowing the particles to escape periodically while they are still too small to degrade film homogeneity. Recall that when plasma power is turned off, electron T and the sheath field decay with a time constant given by Eq. (9.33) and amounting to about 6 μs at 100 Pa. Without the sheath field, the particles are free to escape, and a clean plasma can then be reignited. Thus, 100 percent modulation (on-off) of input power at a switching frequency of a few kHz is very effective in reducing the concentration of observable particles in the plasma [62]. This can be done easily using an in-line electronic rf switch triggered by a square-wave generator.

9.6.3 Downstream deposition

Films can also be deposited "downstream" in the gas flow stream emanating from a plasma, instead of at the very edge of the plasma. This can reduce undesired film deposition within the plasma source if one of

the reactants is injected through a downstream gas ring as shown in Figs. 9.24 and 9.37. Downstream deposition also reduces the variety of energetic species present at the deposition surface and may consequently improve film quality. The price paid for these potential advantages is in deposition rate, since the species that activate the deposition reaction become deactivated as they proceed downstream.

To determine the dominant deposition mechanism of a particular downstream thin-film process, one must first determine what active species are available there. That is, one must assess the degree to which the deposition region is *decoupled* from the plasma. Coupling occurs in both the forward and backward directions: energetic species are transported downstream, and reactants that are injected downstream can "backstream" up into the plasma source against the flow to become activated there. Forward coupling of UV light, which can cause activation of adsorbed species and radiation damage within dielectric films, is easily blocked by the optical baffle shown in Fig. 9.37. For the other active species, the degree of forward coupling depends on their lifetime relative to the time it takes them to be transported downstream.

The transport of ions and electrons is initially at the ambipolar diffusion velocity of Eq. (9.17): $u_a \approx 3\times10^5$ cm/s for $\tilde{T}_e = 3$ eV. But once the electrons are no longer receiving energy from the plasma power source, the drag of ions colliding with molecules thermalizes both species to the gas T. The mean free path for molecular collisions was estimated after Eq. (2.24) to be l (cm) $\approx$ 1/p for p in Pa, and since ion-molecule momentum transfer is efficient for similar masses [Eq. (8.20)], the thermalization time constant is

$$\tau_+ \approx l/u_a = 3\times10^{-6}/p \tag{9.61}$$

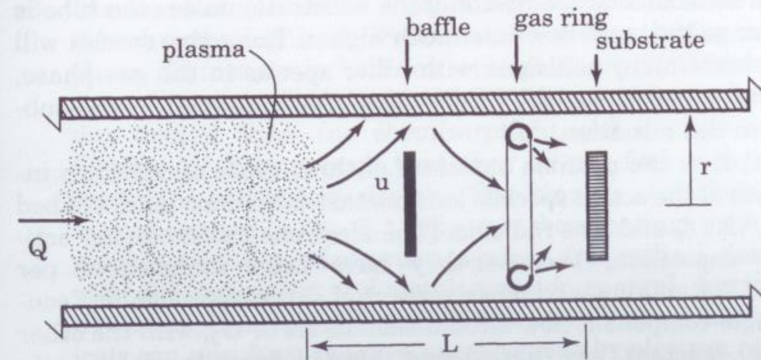

Figure 9.37 Geometry for downstream plasma CVD.

Note that this is 200× faster than the time constant for thermalization of electrons by direct momentum-transfer collisions within the bulk of the plasma when the power is shut off [Eq. (9.33)]. The travel distance during τ_+ is only $u_a\tau_+ = l$, so in downstream transport, the ions and electrons may be considered fully thermalized. Consequently, these species are carried along with the neutral active species at the mean velocity of the gas flow stream, $\bar{u}$ (cm/s). This velocity depends on mass flow rate, Q (sccs), and flow cross section, A (cm^2), in accordance with Eq. (3.14), so that the time for the stream to travel the distance L (cm) downstream from the plasma to the substrate in Fig. 9.37 is

$$t = L/\bar{u} = ALp/10^5 Q \tag{9.62}$$

[Note that the numerator represents just the quantity of gas within volume AL, so that t amounts to a residence time within a volume as in Eq. (7.41).] If we want to operate in the fluid-flow regime to minimize backstreaming, we need to have the Knudsen number, Kn, be ≤ 0.01, where $Kn = l/r \approx 1/pr$ [Eq. (2.25)] and r is the flow-tube radius. Taking r = 5 cm, we need p = 20 Pa (or more). For a typical Q of 100 sccm or 1.7 sccs and an L of 20 cm, we then find from Eq. (9.62) that t = 0.2 s. This time might be made ×100 or so faster by operating at very high Q or low p. Against this time, we must now compare the survival times of the various active species carried by the flow stream.

During transport, the active species are going to be diffusing to the wall with a time constant τ_D given by Eq. (9.59). Taking an average diffusion length $\Lambda = 2$ cm for our 5-cm-radius tube, we have $\tau_D = 5\times10^{-5}p$ or 10^{-3} s at 20 Pa, which is much faster than the transport time of 0.2 s. Raising p slows the diffusion but also slows the transport, so we conclude that all active species are going to experience many wall collisions before reaching the substrate, unless the tube is much wider or the mass flow rate much higher. The active species will also experience many collisions with other species in the gas phase, and we now must assess the likelihood of their survival at the substrate given this situation.

Table 9.1 lists the possible outcomes of three types of collisions involving each of the active species: ions, metastable atoms [as described before Eq. (9.1)], and free radicals. [The electrons can no longer activate film deposition, because they have been thermalized per Eq. (9.61).] For making a trial assessment of survival probability, consider a single-component flow stream such as He or O_2, with the other (depositing) reactant, say SiH_4, being injected downstream so as to minimize upstream reaction and deposition. We now examine the active species of Table 9.1 one by one.

TABLE 9.1 Fates of Active Plasma Species in Common Collisions

Collision with	Active species: B^+	B^*	B (radical)
Molecule	Deactivated by Eq. (9.58) if molecule contains H	Penning reactions [Eqs. (9.1) and (9.2)]	Can react or can recombine in third-body collision
Electron	Recombination needs third body [Eq. (7.38)]		Can become unreactive B^- by Eq. (9.38)
Wall	Neutralized if electron available	Energy lost to wall [7]	Reaction rate increases with adsorption time and wall reactivity (Sec. 5.1)

1. The B^+ ions can react into an inert ion by H abstraction [Eq. (9.58)] only to the extent that the downstream reactant is backstreaming or another H-bearing molecule is available. Recombination with an electron is unstable if pressure is low enough (such as 20 Pa) that third-body collisions are not available to carry away the energy of recombination [see discussion preceding Eq. (7.38)]. Ions are always neutralized at conducting walls, but they are neutralized at insulating walls only if electrons are supplied. Since there are always electrons in the flow stream, wall neutralization is likely.
2. The metastables, B^*, can transfer energy to other molecules by Penning reactions [Eqs. (9.1) and (9.2)]. Even if no such reactions are available, they will generally be deactivated in their first collision with the wall [7].
3. The free radicals can be kept from reacting with other molecules if backstreaming is avoided, and from recombining in the gas phase if pressure is held low enough to avoid third-body collisions. They can also survive wall collisions if the wall is unreactive toward them (no chemisorption) and if their adsorption lifetime is short enough that they do not find each other and recombine before they desorb. (The kinetics of surface reactions were discussed in Sec. 5.1.) Fluorocarbon coatings such as Teflon provide the best passivation against free-radical deactivation, with dielectrics next and metals worst in general, due to the relative adsorption energies and lifetimes on these surfaces. The radicals can also form inactive negative ions by electron attachment [Eq. (9.38)], but there are so many more radicals than electrons in the stream that depletion will be negligible.

In summary, metastables and ions are unlikely to survive unless wall collisions can be avoided, but free radicals can survive if care is taken. In cases where downstream deposition has been reported using a noble-gas plasma such as He along with downstream injection of a reactant such as SiH_4, it is therefore most likely that backstreaming and activation of the reactant is dominating the process.

In the molecular-flow regime of $Kn > 1$ ($p < 0.2$ Pa for $r = 5$ cm), backstreaming is very fast, because the counterflowing streams do not collide with each other. In the fluid-flow regime, the backstreaming problem was solved in connection with pump-oil backstreaming [Eq. (3.13)], where the concentration of the downstream species was found to decrease exponentially with distance upstream, with a 1/e attenuation distance of $L_o = D/\bar{u}$. We take the diffusivity, D, to be $1.9{\times}10^4/p$ cm^2/s for Ar-Ar (Table 2.1) and find the mean flow-stream velocity $\bar{u}$ from Eq. (3.14). At $Q = 100$ sccm and $p = 20$ Pa, this pressure being chosen at the bottom end of the fluid-flow regime for maximum $\bar{u}$, we find that $L_o = 9$ cm. A 99 percent attenuation would take $4.6L_o$ or 40 cm, so we conclude that the elimination of backstreaming reactant is going to require a very high mass flow rate or long transport distance. Reactant that does backstream can be dissociated by active species that are still surviving just downstream of the plasma, and those of the resulting free radicals that are nondepositing can then be swept back to the gas-ring region where they can dissociate depositing reactant. For SiH_4 backstreaming into a He plasma, for example, we expect Penning dissociation [Eq. (9.1)] into $SiH_3 + H$. Then, when the H is swept downstream, the following H-abstraction reaction occurs:

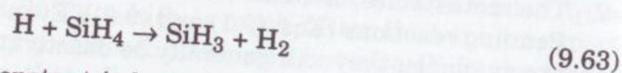

$$H + SiH_4 \rightarrow SiH_3 + H_2 \tag{9.63}$$

for which the rate constant is known [63, 64]: $k = 4{\times}10^{-13}$ $cm^3/mc \cdot s$. The SiH_3 deposits in both regions. This is the most likely mechanism for deposition downstream of noble-gas plasmas, but careful experimental analysis of each situation is needed.

When a high-intensity, low-pressure plasma source is used in the Fig. 9.24 configuration with the depositing reactant being injected from a downstream gas ring, one might expect activation by backstreaming to easily dominate the deposition, since Kn is high. However, a surface activation mechanism also becomes important, whereby the high flux of energetic ions and electrons impinging on the substrate can dissociate reactant which becomes adsorbed there following downstream injection, as discussed in Sec. 8.5.1.2. The dominance of this mechanism was indicated for Si deposition from an ECR H_2 plasma plus downstream SiH_4 when a deposition-thickness pattern was seen on the substrate which replicated that of a grid placed in the

flow stream [65]. Free radicals emanating from the plasma are not as collimated as are electrons and ions confined to magnetic field lines, so the pattern from radical deposition would have been much less distinct. The surface activation mechanism accounts for the directional deposition illustrated in Fig. 9.25*b* which can be obtained downstream of these plasmas. Backstreaming will still occur to the extent that reactant can reflect or desorb from downstream surfaces before reacting, but for ionization fraction approaching unity in a high-intensity, low-pressure source, much of this backstreaming reactant will become ionized and thrown back at the substrate rather than depositing upstream. This direct deposition by ions is also directional.

One might expect that a high enough ion flux emanating from a plasma would sweep backstreaming reactant downstream even for $Kn > 1$, but it may be argued as follows that the ion flux is not high enough to do so. Figure 2.6*b* showed an ion passing into the plane of the paper through an array of gas molecules, and the ion's mean free path was calculated as the distance the ion had to travel before the collision cross sections with the molecules it passed, σ_m, "filled" the total cross section. Using similar reasoning, we now consider the reverse case of a stream of ions passing *out* of the plane of the paper past a relatively stationary thermal molecule. The mean time that it takes for this stream to fill the cross section and thus collide with the molecule is

$$t = 1/J_+\sigma_m \tag{9.64}$$

where J_+ is the ion flux in $ions/cm^2{\cdot}s$ (versus j_+ for A/cm^2). Using Eq. (9.20) for the ion flux, we find that for $n_e = 10^{12}$ cm^{-3} and $\tilde{T}_e = 3$ eV, $t = 2{\times}10^{-3}$ s. During this time, a room-T molecule travels 80 cm, so backstreaming is not significantly impeded by the ion flux.

At higher pressures and flow rates where backstreaming can be avoided, and when the plasma generates chemically active free radicals such as O or N atoms, downstream deposition occurs by reaction of these radicals with a film-forming gas injected downstream, such as SiH_4 to form SiO_2 or SiN_xH_y films, respectively. At still higher pressures including atmospheric, O reacts with O_2 to form O_3 (ozone), which is also an active downstream oxidant. For example, its reaction with $Si(OCH_2CH_3)_4$ (tetra-ethoxysilane or TEOS) forms SiO_2 which is known for excellent deposition conformality over substrate topography.

9.6.4 Case studies

Only a few plasma-CVD chemical systems have been studied enough to describe their deposition mechanisms. Chemical-kinetics studies require elaborate apparatus and tedious measurement. For process

development, it is easier to just keep depositing films and looking at them until the desired results are achieved. Indeed, most (all?) technologically important plasma-CVD processes have been developed in this manner. However, a deeper understanding of the chemistry can explain various puzzling behaviors, point the way toward even better film properties, and help develop new processes. Hydrogenated amorphous Si (aSi:H or just aSi) and Si nitride (SiN_xH_y) have been studied the most, and their mechanisms will be discussed here as examples of the plasma principles presented above. In this discussion, keep in mind the sequence of steps shown in Fig. 9.33. When more than one of the sequences shown are operating in parallel, the fastest one dominates the process, and within that sequence, the slowest step controls the deposition rate.

9.6.4.1 Amorphous silicon. Plasma-CVD aSi is a semiconductor of surprisingly respectable electronic properties. It is widely used for solar cells and photosensors and for thin-film transistors in active-matrix, liquid-crystal, flat-panel displays (AMLCDs) for portable televisions and computers. It is impossible for the four bonds of each Si atom to fully coordinate with each other in an amorphous network. That is, the network is "overconstrained." The resulting dangling bonds would trap all charge carriers and render the material insulating were it not for the termination of these bonds by H amounting to about 10 at.% of the film composition. The keys to effective H incorporation are to (1) start with a H-saturated Si source such as silane gas (SiH_4), (2) use low plasma power to prevent excessive dissociation, and (3) use enough substrate T to develop the Si network without driving out too much H (about 280° C). Electronic-quality aSi cannot be deposited by thermal CVD, because too high a T is required to activate the deposition reaction. The mechanism by which SiH_4 transforms into aSi is quite complex and still somewhat controversial, involving parallel gas-phase reactions and many surface and subsurface processes. The following is a distillation of the current understanding.

The process begins with electron-impact dissociation of SiH_4 into various products. The most likely reactions are

$$SiH_4 \xrightarrow{e} SiH_4^* \rightarrow SiH_3 + H \qquad (\Delta_r H = +4.3\ \text{eV/mc}) \qquad (9.65)$$

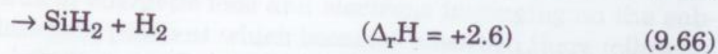

$$\rightarrow SiH_2 + H_2 \qquad (\Delta_r H = +2.6) \qquad (9.66)$$

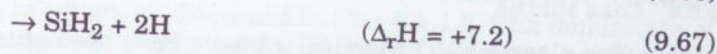

$$\rightarrow SiH_2 + 2H \qquad (\Delta_r H = +7.2) \qquad (9.67)$$

One might expect the reaction requiring the least energy input ($\Delta_r H$) to dominate, but actually there is more than enough energy for any of

these reactions available in the electronically excited species, SiH_4^*, whose internal-energy content is well above that of the products in accordance with the Franck-Condon principle illustrated in Fig. 9.1. Its energy content has to be ≥8 eV, in fact, because that is the observed electron-energy threshold for SiH_4 dissociation (Fig. 9.2). The portion of this energy not used in bond-breaking appears as either internal or translational energy of the products. It has been argued that Eq. (9.67) should dominate [66] because it has been determined to do so when SiH_4 excited by 8.5-eV photons dissociates, but it is likely that all three reactions occur to some extent. This is different from the thermal-CVD situation, where the vertical electronic excitation of Fig. 9.1 does not apply. Thermal excitation instead involves *vibrational* excitation through molecular collisions, as discussed in Sec. 7.3.2. Since the occupancy of vibrational energy levels is exponentially distributed in accordance with Boltzmann statistics as expressed in Eq. (5.13), the low-$\Delta_r H$ reaction of Eq. (9.66) is strongly favored in thermal CVD. This is a crucial difference between plasma chemistry and thermochemistry.

Thus, three principal radical species are produced in some proportion by the above reactions, and these "primary" radicals then proceed to react with neighboring species in ways which *are* governed by thermodynamic favorability. The insertion reactions

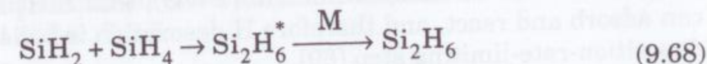

$$SiH_2 + SiH_4 \rightarrow Si_2H_6^* \xrightarrow{M} Si_2H_6 \qquad (9.68)$$

and

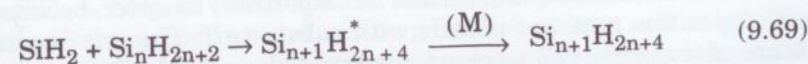

$$SiH_2 + Si_nH_{2n+2} \rightarrow Si_{n+1}H_{2n+4}^* \xrightarrow{(M)} Si_{n+1}H_{2n+4} \qquad (9.69)$$

are known by direct measurement [67] to proceed at collision rate; that is, with the fastest possible rate constant of $k \approx 2{\times}10^{-10}\ cm^3/mc{\cdot}s$ [see Eq. (7.39)]. De-activation of the $Si_2H_6^*$ requires a third-body (M) collision, without which it will just fall apart again. However, k reaches its high-pressure limit with only 130 Pa of He, and this would be lower for other gases. Polysilane species with n > 2 in Eq. (9.69) have enough vibrational degrees of freedom to absorb the reaction energy *without* the aid of a third body, so they are fast at arbitrarily low pressure. These latter reactions are responsible for gas-phase powder formation in both thermal and plasma CVD of Si when pressure is too high, as shown in Fig. 7.15. The other two primary radicals react less quickly. H produces additional SiH_3 by H abstraction [Eq. (9.63)] with $k = 4{\times}10^{-13}\ cm^3/mc{\cdot}s$ as measured by several

labs [63, 64]. SiH_3 has no thermodynamically favorable reactions with SiH_4, but at high enough concentration and pressure, it will recombine with itself to form Si_2H_6 at collision rate with the aid of a third body.

All of these gas-phase products impinge on the deposition surface along with the SiH_4, with their relative fluxes depending on how far from the surface the primary radicals were generated and how many reactive collisions they encountered before reaching the surface. That is, moving away from the generation zone one would expect to see mostly SiH_3 and Si_2H_6, and farther away mostly Si_2H_6. The aSi surface will be almost completely covered with chemisorbed H because of the continual arrival of H-laden precursors and because H is known to effectively passivate the surface of Si, as discussed in Sec. 7.3.3. Because of the passivation, the sticking coefficients, S_c, of SiH_3 and Si_nH_{2n+2} are low, and this accounts for the uniform conformality obtained for aSi deposited over surface topography at low power [68]. On the other hand, SiH_2 is expected to have a very high S_c because of its ability to insert into the Si-H bond as in Eq. (9.68). Fortunately, it never reaches the surface unless pressure is very low or the SiH_4 is highly diluted. The fractional surface coverage by H, Θ, may be roughly modeled by the Langmuir isotherm, Eq. (7.46), which shows that Θ will decrease as the H-desorption rate constant, k_d, increases. It is on the bare Si sites, of fraction $(1 - \Theta)$, that SiH_3 and Si_nH_{2n+2} can adsorb and react, and therefore H desorption is believed to be the deposition-rate-limiting step [69].

There are several possible H-desorption mechanisms, including thermal desorption, reaction with impinging H, and ion bombardment. Thermal desorption cannot be important, however, because the aSi deposition rate varies little with substrate T. The relative importance of the other two mechanisms is not clear. As the SiH_4 is diluted with any of the noble gases, film conformality into trenches degrades, and TEM images begin to show a microcolumnar structure [68] characteristic of "Zone 1" quenched growth (Sec. 5.4). Both of these trends suggest that S_c is becoming high. One would indeed expect a shift to a lower steady-state Θ upon increasing the ratio of nondepositing-ion flux to H-bearing precursor flux if ion-induced desorption were important. However, dilution also increases the probability of the high-S_c SiH_2 reaching the surface before reacting with SiH_4, as has been observed in mass spectrometry [68]. The message here is that it is difficult to do an unambiguous experiment when there are so many things going on, and this is one of the challenges of plasma-CVD analysis.

In addition to its possible role in desorbing the passivating H, impinging H is known to etch Si. Selective etching of strained Si-Si bonds by H can account for the transition of film structure from amor-

phous to "microcrystalline" that occurs with increasing H_2 dilution [68] of the SiH_4 or with increasing exposure of the film to H_2 plasma [70] between intervals of deposition in pure SiH_4. The stronger, unstrained bonds occur where a cluster of Si atoms happens to be approaching its crystalline arrangement, so these crystalline nuclei are selectively left unetched. Now, the microcrystalline Si has far fewer dangling bonds upon which to attach H than does aSi, since they reside only at the grain boundaries instead of throughout the solid. Thus, we are presented here with a curious situation in which a 10× or so dilution of the SiH_4 plasma in H_2 results in a 10× *decrease* in the H content of the deposited film! Similar etching selectivity is believed to be responsible for the ability to deposit diamond films from CH_4-H_2 plasma. Even though graphite is the thermodynamically more stable form of C (except at very high pressure), a higher etch rate for graphite would cause kinetics to win out over equilibrium considerations.

Selective etching can also be used to obtain substrate-selective deposition, because the bonding of depositing Si precursors is weaker to dissimilar substrates such as SiO_2 than it is to Si itself. Since F atoms etch Si, an SiH_4-SiF_4 mixture can be used to obtain substrate-selective deposition [71]. Within a certain window of SiH_4/SiF_4 ratio, deposition is obtained on Si but not on SiO_2, while outside of the window, deposition is obtained on both or neither of the two surfaces. Selective deposition was discussed more fully in the context of thermal CVD toward the end of Sec. 7.3.3.

9.6.4.2 Silicon nitride. Plasma-CVD silicon nitride, SiN_xH_y, deposited from $SiH_4 + NH_3$, is widely used in the microelectronics industry as a diffusion-barrier coating and as the gate dielectric in aSi field-effect transistors. Like aSi, an amorphous network of Si and N having insufficient H is overconstrained by the presence of four bonding electrons on Si and three on N. However, during SiN_xH_y plasma deposition, considerable H (~30 at.%) becomes incorporated and serves to reduce the overconstraint by terminating Si and N bonds. By contrast, SiO_2 is not overconstrained, because the O, with only two bonding electrons, can more easily adjust itself in the network to find Si neighbors. This is why bulk SiO_2 can form a glass (fused quartz) as well as a crystal and why plasma-CVD SiO_2 incorporates relatively little H (~2 at.%). The H in plasma SiO_2 appears as OH, which decreases with increasing substrate T as it combines and evaporates in the form of H_2O, leaving the remaining O bonded to Si. Bond termination in dielectric films is important for many electronics applications, because dangling bonds can trap injected charge and thereby produce internal electric fields which alter device properties.

SiN_xH_y is a material of widely variable composition, unlike crystalline Si_3N_4, and this adds a new complication to deposition-process control. If a plasma-deposited (amorphous) SiN_xH_y film *happened* to have the 4/3 "stoichiometric" N/Si ratio corresponding to crystalline silicon nitride, then the ~30 at.% H would be equally distributed on Si and N atoms, because each broken bond of the overconstrained Si_3N_4 would produce one Si and one N dangling bond. However, the N/Si ratio can in practice vary continuously from zero (aSi:H) to almost two [$Si(NH)_2$, silicon di-imide], depending on deposition conditions, and the H shifts from the Si to the N with increasing N/Si, as seen by infrared absorption of the H bonds [6]. It turns out [72] that the trapping rate of injected electrons drops by ~10^3 as composition shifts from N/Si ≈ 4/3 to the N-saturated limit where all of the H is bonded to N, so the traps apparently are Si dangling bonds or Si-H bonds broken upon encountering an energetic electron. In the N-saturated limit, most of the H appears as NH groups and some as NH_2 groups. NH has two bonding electrons, like O, so it may be thought of as acting like O does in SiO_2 to tie together the Si atoms into a glassy network. By a similar analogy, NH_2 makes only one bond and is therefore equivalent to OH. With increasing substrate T, NH_2 and NH progressively combine and evaporate [6] as NH_3. The electron trapping rate of N-saturated SiN_xH_y is about the same as that of plasma-CVD SiO_2, which further supports the analogy between the two amorphous networks [72].

SiN_xH_y composition depends both on the NH_3/SiH_4 reactant ratio and on plasma power density. Even with a large NH_3/SiH_4 ratio of ~10, Si-rich nitride is obtained if power is too low [6], which indicates that NH_3 requires more electron energy to dissociate than does SiH_4. Note that this result does not *necessarily* follow from the fact that the N-H bond is stronger than the Si-H bond, because of the electronic-excitation factor illustrated in Fig. 9.1. The Si-rich deposit in excess NH_3 also indicates that SiH_n radicals do not readily react with NH_3 gas. To obtain N-saturated deposition, power must be sufficient to *dissociate* enough NH_3 to completely react with all of the SiH_n so as to saturate the depositing Si with bonds to N. Under conventional parallel-plate conditions of 10–100 Pa where gas-phase chemistry is important (see Fig. 9.34), this process has been found to involve the formation of the precursor molecule tetra-aminosilane [6], $Si(NH_2)_4$. This is an unstable molecule that cannot be detected downstream and mostly loses the first amino (NH_2) group in the plasma to form $Si(NH_2)_3$. This radical adsorbs on the surface and then undergoes a "condensation" reaction involving NH_3 gas evolution to form the SiN_xH_y network, as shown in Fig. 9.38. The continuation of this condensation beneath the surface where the network is becoming more rigid would result in stretched Si-N bonds and can thus account for the high tensile stress which is

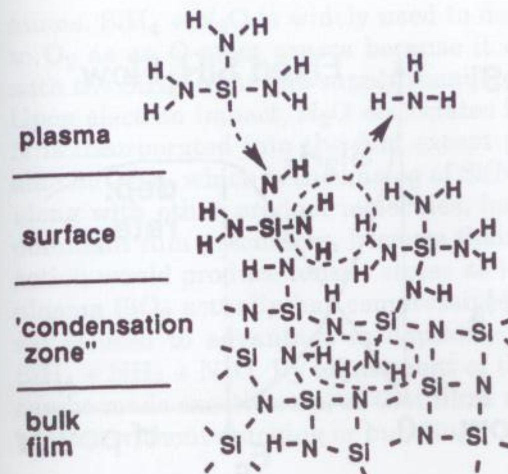

Figure 9.38 Surface and subsurface reactions in the deposition of SiN_xH_y from SiH_4 + NH_3. (Source: Reprinted from Ref. 6 by permission.)

characteristic of this material unless deposited at low frequency (see Fig. 9.17). SiN_xH_y deposited this way also exhibits good film conformality over topography, indicating that $Si(NH_2)_3$ has a low sticking coefficient, S_c. The condensation reaction is thermally activated, because with increasing substrate T, stress increases, and N and H content decrease. The endpoint of this reaction would be the formation of Si_3N_4, but at 530° C the film still contains 20 at.% H. For precursor decomposition, we can write the following overall balanced reaction:

$$3Si(NH_2)_4 \rightarrow Si_3N_4 + 8NH_3 \quad (9.70)$$

The reaction of SiH_n with NH_m represents a chemical "oxidation" of the Si. The plasma generates the NH_m oxidant from NH_3 in proportion to the power applied, and this oxidant is then consumed in reacting with the SiH_n. The same behavior has been observed [72] in the reaction of SiH_4 with N generated from N_2 to form SiN_xH_y and with O from N_2O to form SiO_2. In all cases, complete oxidation of the Si requires the presence of excess oxidant. As SiH_4 mass flow rate is increased, the oxidant becomes depleted as shown in Fig. 9.39*a* until an endpoint (F_c) is reached where the oxidant is completely consumed. At higher flow rates, the excess SiH_n begins to react with *itself* to form Si_2H_6 gas, which can be detected by mass spectrometry downstream, and a smaller amount of the SiH_n deposits as aSi which becomes an undesired part of the nitride or oxide film.

The Fig. 9.39*a* experiment is essentially a "titration" of the oxidant using SiH_4, with the appearance of Si_2H_6 being the endpoint signal. SiH_4 plasma-oxidation processes may be "tuned" in this way to control

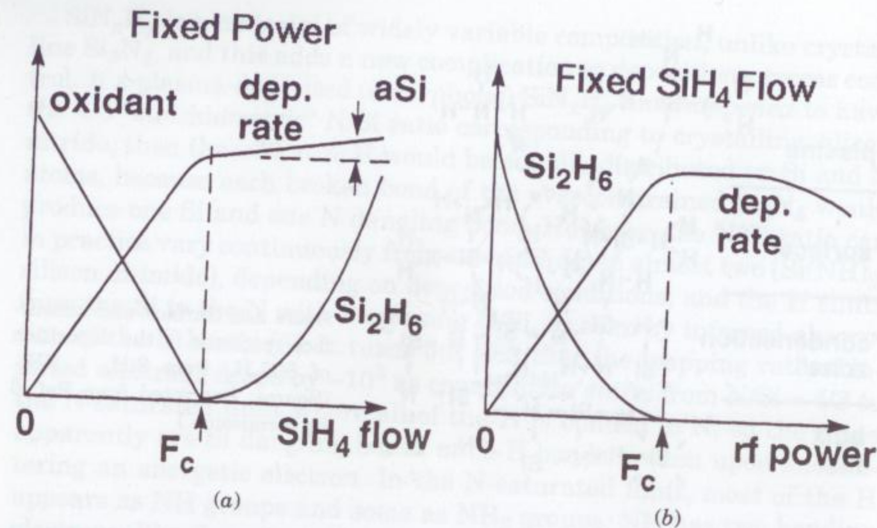

Figure 9.39 Characteristic process behavior of SiN_xH_y and SiO_2 plasma CVD. (Source: Reprinted from Ref. 72 by permission.)

composition and produce good electronic material. The amount of available oxidant increases with power, and the amount needed increases with SiH_4 flow, so the end-point condition is represented by a critical ratio,

$$F_c = (\text{plasma power})/(SiH_4 \text{ mass flow rate}) \tag{9.71}$$

which will be a characteristic of a given reactor and may vary somewhat with reactor geometry and plasma frequency. F_c also varies with the ease of oxidant dissociation, being largest for N_2, smallest for N_2O, and intermediate for NH_3. The F_c point may instead be approached by varying power at a given SiH_4 flow as shown in Fig. 9.39*b*. Downstream Si_2H_6 disappears, and deposition rate levels out, when there is enough power to oxidize all of the SiH_4. In this level region, most of the SiH_4 is incorporated into the depositing film, so the approximate deposition rate expected may be found from the SiH_4 flow rate and is controlled by that rate. In making this calculation, remember that the film deposits on all accessible surfaces, not just on the substrate.

Although the behavior of these three SiH_4-oxidation processes is similar in the aspects discussed above, it is different in other ways. $SiH_4 + N_2$ does not form a gas-phase precursor molecule, deposits poorly over topography, and produces the undesirable microcolumnar "Zone 1" structure [9, 72] (Sec. 5.4). These characteristics indicate that the deposition precursors are high-S_c SiH_n ($n \leq 2$) radicals and N

atoms. $SiH_4 + N_2O$ is widely used to deposit SiO_2. N_2O is preferable to O_2 as an O-atom source because it does not spontaneously react with the SiH_4 in the gas-supply manifold to form powder like O_2 does. Upon electron impact, N_2O dissociates into O and N_2, and negligible N is incorporated into the film except at excessive power. Considerable $Si(OH)_4$, which is the analog of $Si(NH_2)_4$, is seen in the gas phase along with other product molecules, but they are unlikely to be the dominant film precursors, because their subsurface condensation reaction would produce tensile stress as in the case of nitride, whereas plasma SiO_2 actually has compressive stress [72]. This stress reversal is used to advantage in depositing oxynitride, $SiO_xN_yH_z$, from $SiH_4 + NH_3 + N_2O$. By adjustment of the NH_3/N_2O ratio, film stress can be made exactly zero, so that films many microns thick can be deposited without cracking or buckling.

9.7 Conclusion

The glow-discharge plasma is a convenient and versatile source of energetic particles for activating film-deposition processes. It is characterized by a low gas T and by a much higher electron T which is driven by electrical power input. Free radicals generated by electron impact can activate CVD reactions at much lower T than is required for thermal CVD, thus allowing processing of T-sensitive materials. The positive-space-charge sheath surrounding the plasma accelerates positive ions into surrounding surfaces at kinetic energies of 10 to 1000 eV. These ions are useful for source-material sputtering and for film structural modification during deposition. Indeed, the sputter-magnetron is the most widely used technique for volatilizing solid material in thin-film deposition.

Free-radical chemistry and ion energy vary considerably with substrate location and with plasma conditions, especially gas pressure, electrical frequency, and power level. Therefore, the choices of reactor geometry and plasma operating conditions are critical to achievement of the desired film properties. Higher pressure allows more gas-phase chemistry to take place and often produces macroparticle contamination if it is too high. It also scatters ions and sputtered particles and thus reduces their kinetic energy at the surface. Electrical frequency at or above the standard 13.56 MHz is preferred for coupling power through dielectric materials. Increasing frequency reduces ion energy, through a transition in sheath behavior at about 1 MHz and through a steady decrease in sheath voltage at higher frequencies.

One may identify two main categories of plasma-CVD reactors: the conventional parallel-plate discharge, and electrodeless discharges. Electrodeless discharges can be operated at much higher power den-

sity without causing arc breakdown. When the electrons are magnetically confined, electrodeless discharges can also be operated at much lower pressure without causing extinction. This shift in power and pressure causes a change in plasma chemistry from control by free radicals to control by the ion stream. The potential advantages of this new chemistry for film deposition are presently being explored.

9.8 Exercises

9.1 What are the ways in which free electrons can be lost from a plasma?

9.2 (a) Estimate the conductivity, s (S/cm or 1/Ω·cm), of a 10-Pa SiH_4 plasma of density 1×10^{10} e/cm^3 and $\tilde{T}_e$ = 3 eV. How does this compare with the conductivity of (b) Al metal? and (c) the sheath, of width b, at an electrically floating substrate, taking $s = j_+/E \approx j_+/(\Delta V_f/b)$ per Eq. (6.2)?

9.3 Show that the three expressions for the plasma frequency in Eq. (9.15) are equivalent.

9.4 In the low-pressure limit, (a) what is the maximum ion-bombardment flux at the electrodes of a dc Ar plasma operating at 1200 V and 100 W between parallel electrodes 15 cm in diameter and 3 cm apart? (b) What is the plasma density, assuming $\tilde{T}_e$ = 3 eV?

9.5 Name four reasons for preferring an electrodeless discharge in PECVD.

9.6 Activated reactive evaporation of ZnO is being carried out from Zn and O_2 in the geometry of Fig. 9.7. The O_2 pressure is low enough that Zn-vapor scattering during transport can be neglected. The electron current across the evaporant stream is 1 A and is distributed over an area of 10 × 10 cm. Estimate the probability of Zn ionization.

9.7 Using the mean free path calculated following Eq. (2.24) and using Fig. 9.8, estimate the fraction of sputtered Pt that reaches the substrate in a planar-diode plasma having an 8-cm gap and operating at the minimum pressure given by Eq. (9.24).

9.8 Silicon nitride (ε = 6.5) is being deposited by PECVD in a symmetrical, parallel-plate discharge. Assuming square-wave drive voltage for simplicity, at peak voltage V_o = 800 V and 1 mA/cm^2 of ion flux across the sheaths, what is the minimum drive frequency that will keep the film from charging up to beyond half of its breakdown strength of 6 MV/cm?

9.9 (a) Derive Eq. (9.36). (b) What is the transit time of H^+ across a 1000-V, 1-cm collisionless sheath? (c) What is the functional dependence of τ_+ on V_b?

9.10 Consider a plasma sheath to be oscillating sinusoidally with a peak-to-peak amplitude equal to the sheath thickness of Eq. (9.23). For 13.56 MHz drive power at a peak voltage of 300 V and for $n_e = 10^{10}$ cm^{-3} and $\tilde{T}_e$ = 3 eV in the plasma, what is the maximum energy gain in eV of an electron reflected off the oscillating sheath? (Hint: use a moving coordinate system.)

9.11 Estimate the pressure for most efficient power coupling in a 2.45 GHz plasma having $\tilde{T}_e$ = 3 eV. (Sec. 9.5.1)

9.12 Assuming a typical electron-molecule collision cross section for momentum transfer, calculate the pressure at which a 10-eV electron in a 2.45-GHz ECR plasma encounters one collision per orbit.

9.13 An rf-bias power of 400 W is needed to achieve a dc bias of −300 V on a 150-cm^2 substrate platform downstream of an ECR source. (a) What is the ion flux to the substrate, and (b) what is the plasma density over the substrate?

9.14 Derive Eq. (9.51) from Eq. (9.49).

9.15 (a) What two operating conditions in high-power, electrodeless glow discharges result in ionization fractions near unity? (b) What allows each of these operating conditions to be achieved?

9.16 Show that a molecule can indeed travel about 80 cm upstream against the plasma-source ion flux in the example following Eq. (9.64).

9.17 Describe at least three deposition mechanisms operable in the apparatus of Fig. 9.24.

9.18 Describe three ways to reduce macroparticles in plasma CVD and how they work.

9.19 (a) How many sccm of SiH_4 are required to deposit $SiN_{1.7}H_{1.1}$ of density 2.3 g/cm^3 at 500 nm/m in a 30-cm-diameter parallel-plate reactor, assuming 60 percent SiH_4 utilization? (b) What is the minimum mass flow rate of NH_3 needed to achieve N saturation of the SiH_4, assuming 20 percent NH_3 dissociation?

9.9 References

1. Collart, E.J.H., J.A.G. Baggerman, and R.J. Visser. 1991. "Excitation Mechanisms of Oxygen Atoms in a Low Pressure O_2 Radio-Frequency Plasma." *J. Appl. Phys.* 70:5278.
2. Aydil, E.S., and D.J. Economou. 1992. "Theoretical and Experimental Investigations of Chlorine RF Glow Discharges." *J. Electrochem. Soc.* 139:1406.
3. Krogh, O., T. Wicker, and B. Chapman. 1986. "The Role of Gas Phase Reactions, Electron Impact, and Collisional Energy Transfer Processes Relevant to Plasma Etching of Polysilicon with H_2 and Cl_2." *J. Vac. Sci. Technol.* B4:1292.
4. Coburn, J.W., and M. Chen. 1980. "Optical Emission Spectroscopy of Reactive Plasmas: A Method for Correlating Emission Intensities to Reactive Particle Density." *J. Appl. Phys.* 51:3134.

5. Donnelly, V.M. 1989. "Optical Diagnostic Techniques for Low Pressure Plasmas and Plasma Processing." Chap. 1 in *Plasma Diagnostics*, vol. 1, ed. O. Auciello and D.L. Flamm. Orlando, Fla.: Academic Press.
6. Smith, D.L., A.S. Alimonda, C.-C. Chen, S.E. Ready, and B. Wacker. 1990. "Mechanism of SiN_xH_y Deposition from NH_3-SiH_4 Plasma." *J. Electrochem. Soc.* 137:614.
7. Kolts, J.H., and D.W. Setser. 1979. "Electronically Excited Long-Lived States of Atoms and Diatomic Molecules in Flow Systems." Chap. 3 in *Reactive Intermediates in the Gas Phase*, ed. D.W. Setser. Orlando, Fla.: Academic Press.
8. Libby, W.F. 1979. "Plasma Chemistry." *J. Vac. Sci. Technol.* 16:414.
9. Smith, D.L., A.S. Alimonda, and F.J. von Preissig. 1990. "Mechanism of SiN_xH_y Deposition from N_2-SiH_4 Plasma." *J. Vac. Sci. Technol.* B8:551.
10. Hershkowitz, N. 1989. "How Langmuir Probes Work." Chap. 3 in *Plasma Diagnostics*, vol. 1, ed. O. Auciello and D.L. Flamm. Orlando, Fla.: Academic Press.
11. Meuth, H., and E. Sevillano. 1989. "Microwave Diagnostics." Chap. 5 in *Plasma Diagnostics*, vol. 1, ed. O. Auciello and D.L. Flamm. Orlando, Fla.: Academic Press.
12. Kushner, M.J. 1988. "A Model for the Discharge Kinetics and Plasma Chemistry during Plasma Enhanced Chemical Vapor Deposition of Amorphous Silicon." *J. Appl. Phys.* 63:2532.
13. Gottscho, R.A. 1986. "Negative Ion Kinetics in RF Glow Discharges." *IEEE Trans. on Plasma Science* 14:92.
14. Godyak, V.A., and N. Sternberg. 1990. "Dynamic Model of the Electrode Sheaths in Symmetrically Driven RF Discharges." *Phys. Rev. A* 42:2299.
15. Godyak, V.A., and N. Sternberg. 1990. "Smooth Plasma-Sheath Transition in a Hydrodynamic Model." *IEEE Trans. on Plasma Science* 18:159.
16. Pennebaker, W.B. 1979. "Influence of Scattering and Ionization on RF Impedance in Glow Discharge Sheaths." *IBM J. Res. Develop.* 23:16.
17. Bunshah, R.F. 1983. "Processes of the Activated Reactive Evaporation Type and Their Tribological Applications." *Thin Solid Films* 107:21.
18. Westwood, W.D. 1978. "Calculation of Deposition Rates in Diode Sputtering Systems." *J. Vac. Sci. Technol.* 15:1.
19. Rossnagel, S.M. 1988. "Deposition and Redeposition in Magnetrons." *J. Vac. Sci. Technol.* A6:3049.
20. Stutzin, G.C., K. Rózsa, and A. Gallagher. 1993. "Deposition Rates in Direct Current Diode Sputtering." *J. Vac. Sci. Technol.* A11:647.
21. Cuomo, J.J., R.J. Gambino, J.M.E. Harper, and J.D. Kuptsis. 1978. "Significance of Negative Ion Formation in Sputtering and SIMS Analysis." *J. Vac. Sci. Technol.* 15:281.
22. Tominaga, K., S. Iwamura, Y. Shintani, and O. Tada. 1982. "Energy Analysis of High-Energy Neutral Atoms in the Sputtering of ZnO and $BaTiO_3$." *Jap. J. Appl. Phys.* 21:688.
23. Venkatesan, T., X.X. Xi, Q. Li, X.D. Wu, R. Muenchausen, A. Pique, R. Edwards, and S. Mathews. 1993. "Pulsed Laser and Cylindrical Magnetron Sputter Deposition of Epitaxial Metal Oxide Thin Films." In *Selected Topics in Superconductivity*, ed. L.C. Gupta and M.S. Multani. Singapore: World Scientific, 625.
24. Berg, S., M. Moradi, C. Nender, and H.-O. Blom. 1989. "The Use of Process Modelling for Optimum Design of Reactive Sputtering Processes." *Surface and Coatings Technol.* 39/40:465.
25. Carlsson, P., C. Nender, H. Barankova, and S. Berg. 1993. "Reactive Sputtering using Two Reactive Gases: Experiments and Computer Modelling." *J. Vac. Sci. Technol.* A11:1534.
26. Thornton, J.A. 1982. "Coating Deposition by Sputtering." Chap. 5 in *Deposition Technologies for Films and Coatings*, ed. R.F. Bunshah. Park Ridge, N.J.: Noyes Publications.

27. Rossnagel, S.M. 1991. "Glow Discharge Plasmas and Sources for Etching and Deposition." Chap. II-1 in *Thin Film Processes II*, ed. J.L. Vossen and W. Kern. Orlando, Fla.: Academic Press.
28. Window, B., and G.L. Harding. 1990. "Ion-assisting Magnetron Sources: Principles and Uses." *J. Vac. Sci. Technol.* A8:1277.
29. Window, B., and G.L. Harding. 1992. "Characterization of Radio Frequency Unbalanced Magnetrons." *J. Vac. Sci. Technol.* A10:3300.
30. Rossnagel, S.M., and J. Hopwood. 1994. "Metal Ion Deposition from Ionized Magnetron Sputtering Discharges." *J. Vac. Sci. Technol.* B12:449.
31. Köhler, K., D.E. Horne, and J.W. Coburn. 1985. "Frequency Dependence of Ion Bombardment of Grounded Surfaces in RF Argon Glow Discharges in a Planar System." *J. Appl. Phys.* 58:3350.
32. Gottscho, R.A. 1987. "Glow-Discharge Sheath Electric Fields: Negative-Ion, Power, and Frequency Effects." *Phys. Rev. A* 36:2233.
33. Claassen, W.A.P., W.G.J.N. Valkenburg, M.F.C. Willemsen, and W.M.v.d. Wijgert. 1985. "Influence of Deposition Temperature, Gas Pressure, Gas Phase Composition, and RF Frequency on Composition and Mechanical Stress of Plasma Silicon Nitride Layers." *J. Electrochem. Soc.* 132:893.
34. Godyak, V.A., R.B. Piejak, and B.M. Alexandrovich. 1991. "Ion Flux and Ion Power Losses at the Electrode Sheaths in a Symmetrical RF Discharge." *J. Appl. Phys.* 69:3455.
35. Howling, A.A., J.-L. Dorier, and Ch. Hollenstein. 1992. "Frequency Effects in Silane Plasmas for Plasma Enhanced Chemical Vapor Deposition." *J. Vac. Sci. Technol.* A10:1080.
36. Godyak, V.A., and A.S. Khanneh. 1986. "Ion Bombardment Secondary Electron Maintenance of Steady RF Discharge." *IEEE Trans. on Plasma Science* PS-14:112.
37. Köhler, K., J.W. Coburn, D.E. Horne, and E. Kay. 1985. "Plasma Potentials of 13.56 MHz RF Argon Glow Discharges in a Planar System." *J. Appl. Phys.* 57:59.
38. Smith, D.L., and A.S. Alimonda. 1994. "Coupling of Radio-Frequency Bias Power to Substrates without Direct Contact, for Application to Film Deposition with Substrate Transport." *J. Vac. Sci. Technol.* A12:3239.
39. Gottscho, R.A., G.R. Scheller, D. Stoneback, and T. Intrator. 1989. "The Effect of Electrode Area Ratio on Low-Frequency Glow Discharges." *J. Appl. Phys.* 66:492.
40. Godyak, V.A., R.B. Piejak, and B.M. Alexandrovich. 1991. "Ion Flux and Ion Power Losses at the Electrode Sheaths in a Symmetrical RF Discharge." *J. Appl. Phys.* 69:3455.
41. Hall, G.L. et al. (eds.). 1984. *The Radio Amateur's Handbook*, Chaps. 2 and 19. Newington, Conn.: American Radio Relay League.
42. Alcaide, H.D. 1982. "RFI Prevention in RF Plasma Systems." *Solid State Technol.* (April).
43. Feynman, R.P., R.B. Leighton, and M. Sands. 1964. *The Feynman Lectures on Physics*, vol. 2. Reading, Mass.: Addison-Wesley.
44. Suggestion by R.B. Piejak, May, 1991.
45. Hey, H.P.W., B.G. Sluijk, and D.G. Hemmes. 1990. "Ion Bombardment: a Determining Factor in Plasma CVD." *Solid State Technol.* (April):139.
46. Fehsenfeld, F.C., K.M. Evenson, and H.P. Broida. 1965. "Microwave Discharge Cavities Operating at 2450 MHz." *Rev. Sci. Instr.* 36:294.
47. Moisan, M., J. Hubert, J. Margot, G. Sauvé, and Z. Zakrzewski. 1993. "The Contribution of Surface-Wave Sustained Plasmas to HF Plasma Generation, Modeling and Applications: Status and Perspectives." In *Microwave Discharges: Fundamentals and Applications*, ed. C.M. Ferreira and M. Moisan. New York: Plenum.
48. Chen, F.F. 1974. *Introduction to Plasma Physics*, Chap. 4. New York: Plenum.

49. Asmussen, J. 1989. "Electron Cyclotron Resonance Microwave Discharges for Etching and Thin Film Deposition." *J. Vac. Sci. Technol.* A7:883.
50. Gorbatkin, S.M., L.A. Berry, and J.B. Roberto. 1990. "Behavior of Ar Plasmas Formed in a Mirror Field Electron Cyclotron Resonance Microwave Ion Source." *J. Vac. Sci. Technol.* A8:2893.
51. Matsuoka, M., and K. Ono. 1988. "Magnetic Field Gradient Effects on Ion Energy for Electron Cyclotron Resonance Microwave Plasma Stream." *J. Vac. Sci. Technol.* A6:25.
52. Berry, L.A., and S.M. Gorbatkin. 1995. "Permanent Magnet Electron Cyclotron Resonance Plasma Source with Remote Window." *J. Vac. Sci. Technol.* A13(2).
53. Perry, A.J., D. Vender, and R.W. Boswell. 1991. "The Application of the Helicon Source to Plasma Processing." *J. Vac. Sci. Technol.* B9:310.
54. Hopwood, J. 1992. "Review of Inductively Coupled Plasmas for Plasma Processing." *Plasma Sources Sci. and Technol.* 1:109.
55. Cook, J.M., D.E. Ibbotson, P.D. Foo, and D.L. Flamm. 1990. "Etching Results and Comparison of Low Pressure Electron Cyclotron Resonance and Radio Frequency Discharge Sources." *J. Vac. Sci. Technol.* A8:1820.
56. Masu, K., K. Tsubouchi, N. Shigeeda, T. Matano, and N. Mikoshiba. 1990. "Selective Deposition of Aluminum from Selectively Excited Metalorganic Source by the RF Plasma." *Appl. Phys. Lett.* 56:1543.
57. Cheng, L.-Y., J.P. McVittie, and K.C. Saraswat. 1991. "New Test Structure to Identify Step Coverage Mechanisms in Chemical Vapor Deposition of Silicon Dioxide." *Appl. Phys. Lett.* 58:2147.
58. Kilgore, M.D., J.E. Daugherty, R.K. Porteous, and D.B. Graves. 1994. "Transport and Heating of Small Particles in High Density Plasma Sources." *J. Vac. Sci. Technol.* B12:486.
59. Kilgore, M.D., J.E. Daugherty, R.K. Porteous, and D.B. Graves. 1993. "Ion Drag on an Isolated Particulate in a Low-Pressure Discharge." *J. Appl. Phys.* 73:195.
60. Selwyn, G.S., J.H. Heidenreich, and K.L. Haller. 1991. "Rastered Laser Light Scattering Studies during Plasma Processing: Particle Contamination Trapping Phenomena." *J. Vac. Sci. Technol.* A9:2817.
61. Yoo, W.J., and Ch. Steinbrüchel. 1992. "Kinetics of Particle Formation in the Sputtering and Reactive Ion Etching of Silicon." *J. Vac. Sci. Technol.* A10:1041.
62. Verdeyen, J.T., J. Beberman, and L. Overzet. 1990. "Modulated Discharges: Effect on Plasma Parameters and Deposition." *J. Vac. Sci. Technol.* A8:1851.
63. Becerra, R., and R. Walsh. 1987. "Mechanism of Formation of Tri- and Tetrasilane in the Reaction of Atomic Hydrogen with Monosilane and the Thermochemistry of the Si_2H_4 Isomers." *J. Phys. Chem.* 91:5765.
64. Johnson, N.M., J. Walker, and K.S. Stevens. 1991. "Characterization of a Remote Hydrogen Plasma Reactor with Electron Spin Resonance." *J. Appl. Phys.* 69:2631.
65. Nakayama, Y., M. Kondoh, K. Hitsuishi, M. Zhang, and T. Kawamura. 1990. "Behavior of Charged Particles in an Electron Cyclotron Resonance Plasma Chemical Vapor Deposition Reactor." *Appl. Phys. Lett.* 57:2297.
66. Gallagher, A. 1988. "Neutral Radical Deposition from Silane Discharges." *J. Appl. Phys.* 63:2406.
67. Jasinski, J.M. 1994. "Gas Phase and Gas Surface Kinetics of Transient Silicon Hydride Species." In *Gas-Phase and Surface Chemistry in Electronic Materials Processing*, Proceedings vol. 334. Pittsburgh, Pa.: Materials Research Society.
68. Street, R.A. 1991. *Hydrogenated Amorphous Silicon*, Chap. 2. Cambridge, U.K.: Cambridge U. Press.
69. Veprek, S., and M. Heintze. 1990. "The Mechanism of Plasma-Induced Deposition of Amorphous Silicon from Silane." *Plasma Chem. and Plasma Processing* 10:3.

70. Boland, J.J., and G.N. Parsons. 1992. "Bond Selectivity in Silicon Film Growth." *Science* 256:1304.
71. Baert, K., P. Deschepper, J. Poortmans, J. Nijs, and R. Mertens. 1992. "Selective Si Epitaxial Growth by Plasma-Enhanced Chemical Vapor Deposition at Very Low Temperature." *Appl. Phys. Lett.* 60:442.
72. Smith, D.L. 1993. "Controlling the Plasma Chemistry of Silicon Nitride and Oxide Deposition from Silane." *J. Vac. Sci. Technol.* A11:1843.

9.10 Suggested Readings

Cecchi, J.L. 1990. "Introduction to Plasma Concepts and Discharge Configurations." Chap. 2 in *Handbook of Plasma Processing Technology*, ed. S.M. Rossnagel, J.J. Cuomo, and W.D. Westwood, eds. Park Ridge, N.J.: Noyes Publications.

Chapman, B. 1980. *Glow Discharge Processes: Sputtering and Plasma Etching.* New York: John Wiley & Sons.

Kroesen, G.M.W., and F.J. de Hoog. 1993. "In-Situ Diagnostics for Plasma Surface Processing." *Appl. Phys.* A 56:479.

Lieberman, M.A., and R.A. Gottscho. 1993. "Design of High Density Plasma Sources for Materials Processing." In *Physics of Thin Films: Advances in Research and Development*, vol. 3, ed. J. Vossen. Orlando, Florida: Academic Press.

Thornton, J.A. 1982. "Plasmas in Deposition Processes." Chap. 2 in *Deposition Technologies for Films and Coatings*," ed. R.F. Bunshah. Park Ridge, N.J.: Noyes Publications.